



Universidade do Minho
Escola de Engenharia

Miguel Ângelo Silva Sanches

Integration of tactile sensing and feedback control of an under-actuated gripper with adjustable modes of operation

Dissertação de Mestrado

Mestrado Integrado em Engenharia Física

Ramo de Dispositivos, Microssistemas e Nanotecnologias

Trabalho efetuado sob a orientação da

Professora Doutora Cristina Peixoto Santos

Professora Doutora Jamie Paik

Dezembro de 2018

DECLARAÇÃO

Nome: Miguel Ângelo Silva Sanches

Endereço eletrónico: miguelsanches.sjm@gmail.com

Telefone: 914019050

Bilhete de Identidade/Cartão do Cidadão: 14517814

Título da dissertação: Integration of tactile sensing and feedback control of an under-actuated gripper with adjustable modes of operation

Orientador/a/es:

Professora Doutora Cristina Peixoto Santos

Professora Doutora Jamie Paik

Ano de conclusão: 2018

Mestrado Integrado em Engenharia Física

É AUTORIZADA A REPRODUÇÃO INTEGRAL DESTA DISSERTAÇÃO APENAS PARA EFEITOS DE INVESTIGAÇÃO, MEDIANTE DECLARAÇÃO ESCRITA DO INTERESSADO, QUE A TAL SE COMPROMETE.

Universidade do Minho, 12 / 12 / 2018

Assinatura: *Miguel Sanches*

ACKNOWLEDGMENTS

All the work carried during the past year would not be possible without the help, understanding and support from many people.

First and foremost, I would like to express my gratitude to my adviser Prof. Cristina Santos, who allowed me the possibility of being integrated in the BiRD Lab (Bio-inspired/Biomedical Robotic Devices) here at University of Minho. I am extremely grateful for her dedication, support and time spent since the beginning, always being available to help and providing insightful discussions, constructive criticisms and advices that helped me develop this accomplishment and contributed to the final quality of this thesis.

I would like to also express my deepest gratitude to Prof. Jamie Paik for hosting and integrating me in the RRL (Reconfigurable Robotics Lab) at EPFL, Switzerland. I am grateful for this opportunity and for her transmitted passion, creating an excellent atmosphere of mutual aid between all of those who research at RRL. A special thank to Dr. Amir Firouzeh for the all his patience, transmitted knowledge during the past year, which largely contributed to develop this work, and for encouraging me to develop my critical spirit and take a different perspective when solving problems.

I am especially thankful to my parents, José e Graça, and my sister, Rita, for their constant support, love and encouragement, not only during this past year but since the very beginning of this long journey, without them this work would not be possible.

I would also like to express my warm thank you to my girlfriend Cristiana, for supporting me when I needed the most, for all the hours giving me the strength to finish this journey and encouraging me to not give up even when I am tired.

Finally, I would like to thank to all my friends and everybody in the lab, either at University of Minho or at EPFL, for the companionship and support that provided me with an excellent daily environment between hard work and laughs.

RESUMO

Garras robóticas sub-atuadas apresentam um *design* compacto e estratégias simples de controlo e atuação, mas com o custo de configurações estáveis, quando comparados com sistemas totalmente atuados. Assim, torna-se importante o estudo e compreensão das forças de interação entre as garras e os objetos que são por elas agarrados. Tendo estas considerações como base, esta tese aborda o desenvolvimento de uma garra sub-atuada inspirada em origamis e que possui juntas de rigidez ajustáveis e sensores táteis, sendo estes utilizados com o objetivo de iniciar o estudo de configurações efetivas para agarrar objetos.

No trabalho aqui apresentado, uma garra sub-atuada é composta por dois dedos robóticos, sendo estes fabricados usando métodos precisos e uma técnica de fabricação de camada-a-camada que permite a integração de múltiplas camadas funcionais, tornando, por isso, o processo escalável e personalizável ao meio envolvente onde a garra será inserida. Uma camada de rigidez ajustável, composta por um *heater* elástico embebido num polímero com memória, permite adotar diferentes configurações e ajustar a *compliance* dos dedos do manipulador. O *heater* é responsável por ativar termicamente o polímero, modulando a sua rigidez e, por conseguinte, ativando as juntas desejadas. Assim, múltiplas configurações para os dedos da garra podem ser definidas para agarrar diferentes objetos, dependendo do seu tamanho, forma, peso e tarefa a ser executada. Para além disso, um sistema de sensores táteis é integrado nos seus dedos com o objetivo de fornecer a informação acerca da interação entre a garra e o objeto.

Finalmente, o estudo de configurações efetivas para agarrar objetos é realizado simulando inicialmente o movimento livre da garra sub-atuada, i.e., quando não existe um objeto a ser segurado. Os resultados são comparados com a configuração esperada quando o limite das juntas é atingido. Seguidamente, dois modos de operação são testados usando a garra fabricada: uma pega de força e uma pega de precisão. A fase de pega de um objeto é inicialmente estudada usando uma configuração de pega de força para que se compreenda como o envolvimento de um objeto permite atingir uma pega estável. Posteriormente, é realizado o estudo da pega de objetos de diferentes tamanhos, utilizando pegas de precisão, com o objetivo de analisar o *feedback* das forças de contato proporcionado pelos sensores táteis.

Os resultados mostram a importância do uso de sensores táteis para compreender e agarrar objetos do quotidiano, uma vez que tais sistemas permitem controlar e ajustar as forças de

contato para melhorar as pegadas e garantir interações mais seguras entre a garra e o meio que o envolve.

Palavras-chave: Juntas de rigidez ajustáveis, forças de contacto, configurações de pega, origami robótico, sensores táteis, manipulador sub-atuado.

ABSTRACT

Under-actuated robotic grippers offer compact design and simple actuation and control strategies, but at the cost of limited stable configurations when compared with fully actuated systems. Thus, it is important to understand and study the interaction forces between the objects being grasped by the gripper. Taken this matter into consideration, this thesis addresses the development of an origami based under-actuated gripper with adjustable stiffness joints and tactile sensors with the goal of initiating the study of effective grasp configurations.

In this work, a tendon-driven robogami under-actuated gripper is composed by two robotic fingers which are manufactured using precise fabrication methods and a unique layer-by-layer manufacturing technique that allows integrating multiple functional layers, making such process scalable and customizable to the environment where the gripper will be inserted. An adjustable stiffness layer (ASL) composed by a stretchable heater embedded inside a shape memory polymer (SMP) allows achieving different configurations for the fingers and adjust the compliance of the gripper. The stretchable heater is responsible for thermally activating the SMP modulating its stiffness and hence activating the desired joints. Thus, multiple configurations for the fingers of the gripper can be defined to grasp different objects depending on their size, shape, weight and task to be performed. Also, a tactile sensing system is integrated on the fingers to provide the interaction information between the gripper and the object.

Finally, the study of effective grasps configuration is performed by initially simulating the free motion of the tendon-driven robogami under-actuated gripper, i.e. when there is not an object being grasped. The results are compared to the expected configuration when joint limit is reached. Then, two modes of operation are tested using the manufactured gripper, a power grasp and a precision grasp. The grasping phase of an object is initially studied for the power grasp to understand how enveloping an object allows achieving stable grasps. Afterwards, the grasping study of different sized objects using precision grasps is performed, with the goal to analyze the contact forces feedback provided by the tactile sensors.

The results show the importance of using tactile sensors to perceive and grasp daily objects, since such systems allows controlling and adjust the contact forces to improve grasps and ensure safer interactions between the gripper and the surrounding environment.

Keywords: Adjustable stiffness joints, contact forces, grasping configurations, robotic origami, tactile sensing, under-actuated gripper.

TABLE OF CONTENTS

Acknowledgments	iii
Resumo	v
Abstract	vii
Table of contents	ix
List of figures	xi
List of tables	xix
List of abbreviations and acronyms	xxi
CHAPTER 1 Introduction	1
1.1 Motivation, goals and problem statement.....	1
1.2 Overview of the research.....	2
1.2.1 Goals and research questions	3
1.3 Contributions to knowledge.....	4
1.4 Thesis outline and structure.....	5
CHAPTER 2 Literature review.....	7
2.1 Fully vs under-actuated grippers	7
2.1.1 Fully-actuated robotic hands	7
2.1.2 Under-actuated robotic hands.....	9
2.2 Under-actuation as a solution to grasping	11
2.3 Compliant under-actuated grippers	13
2.4 Under-actuated grippers with tactile sensing.....	18
2.5 Stretchable heaters/sensors	21
2.6 Summary of the presented studies	24
CHAPTER 3 Under-actuated gripper with adjustable stiffness joints	27
3.1 Manufacturing process	27
3.1.1 Robogami finger manufacturing process	28
3.1.2 Robogami finger structure.....	30
3.1.3 Adjustable stiffness layer (ASL) manufacturing process.....	31
3.2 Mathematical model	34
CHAPTER 4 Stretchable heater	39
4.1 Stretchable heater design	39
4.2 Stretchable heater manufacturing process	42

4.2.1	Layers deposition	42
4.2.2	Serpentine path patterning.....	44
4.2.3	Mesh pattern structure	48
4.2.4	Device release	53
4.3	Stretchable heater characterization	55
4.3.1	Resistance measurement and acquisition	56
4.3.2	Temperature effect contribution.....	60
4.3.3	Mechanical deformation effect contribution	61
CHAPTER 5 Tactile sensing integration.....		63
5.1	Tactile sensors performance comparison	63
5.1.1	Voltage to temperature conversion	66
5.1.2	Test comparison	68
5.2	Tactile sensor characterization	70
5.3	Tactile sensors integration	73
5.4	Thermistors integration.....	75
5.5	Study of effective grasps configurations	76
5.5.1	Adjustable grasp modes of operation	77
5.5.2	Effective grasp configurations results	78
CHAPTER 6 Conclusion and future work		85
6.1	Conclusion	85
6.2	Future work.....	88
6.2.1	Adjustable stiffness layer improvement	88
6.2.2	Stretchable heaters improvements.....	89
6.2.3	Effective grasps configurations	89
References		93
Appendix I – Rate of tendon displacement		103
Appendix II – ASL elongation		105
Appendix III – Equilibrium state		107
Appendix IV – Stretchable heaters manufacturing process outline		109
Appendix V – Sallen-Key 2 nd order filter		117

LIST OF FIGURES

Figure 1 – Fully-actuated robotic hands: (a) – Okada Hand [27]; (b) – Salisbury’s Hand [28]; (c) – Utah/MIT Hand [29]; (d) – DLR1 Hand [30]; (e) – DLR2 Hand [31].	8
Figure 2 – Evolution from the RTR Hand: (a) – RTR1 Hand [37] was a fully-actuated robotic hand, while the RTR2 Hand [38] , (b), and the SPRING Hand [39], (c), were under-actuated. The difference between the two latter versions was the transmission mechanism used to drive the fingers.	10
Figure 3 – First version of an under-actuated gripper, presented by Hirose, S. and Umetani, Y. [7]. The soft gripper conforms to an object thanks to the redundant number of DoFs – (a). The mechanism presented consisted of several phalanges with a cable and pulley driven mechanism – (b).	12
Figure 4 – Grasping phase of the soft gripper presented by Hirose, S. and Umetani, Y. [7]. The finger is initially at a resting position thanks to a releasing wire. Once the input torque is applied, the fingers envelop the object distributing the contact forces around the object.	12
Figure 5 – Under-actuated finger composed by Teflon material [13]. The rigid joint coupling achieved by the one-piece structure allows reducing the cost of the manufacturing process – (a). The finger design determines the limit configuration angle for the bending motion of the three hinges – (b).	14
Figure 6 – Adjustable under-actuated finger [45]. The thermoplastic stiffness varies according to the temperature when a signal is passed through Nichrome wires embed inside the PCL layer, while thermistors are used as sensing elements to estimate the temperature of the active PCL layer – (a). As a result, the configuration of the finger can be adjusted – (b).	14
Figure 7 – Shape memory alloy-based soft gripper[14].By selectively activating the stiffness of the desired hinges (red hinges) and actuating the relevant SMA wire (red) the joint to be bent and their bending direction can be chosen.	15
Figure 8 – Pneumatic under-actuated gripper with adjustable stiffness joints[47].The finger structure is composed by an acrylonitrile butadiene styrene (ABS) structure acting as bone. Each bone part is linked to a SMP structure that acts as a joint – (a). A pneumatic soft actuator passes through the structure bending the activated joints, whose temperature is higher than the glass transition temperature of the SMP – (b).	17

Figure 9 – Adjustable Stiffness Layer manufacturing process[4]. A stretchable heater, (a), is embedded inside two SMP sheets, (b), and two glass fibers frames, (c). Finally, the structure is encapsulated using silicone rubber, (d).	18
Figure 10 – Under-actuated robotic hand with integrated tactile sensors [21]. A cable driven mechanism and torsion springs are used to actuate the joints – (a), while three pneumatic sensors placed on the tip of the fingers to provide feedback to obtain rough information on the object shape – (b).	19
Figure 11 – Compliant under-actuated gripper with locking mechanism and tactile sensors, (a). Eletrolaminate breaks allow configuring the actuated joints using a tendon-driven mechanism. The layers that compose the capacitive sensors are illustrated in (b). A silicone elastomer acts as dielectric layer between a conductive fabric layer and a sensing plate connected to an active shield preventing capacitive coupled currents to interfere on the signal being measured [22].....	20
Figure 12 –Stretchable patterns: (a) – Meander patterns on stretchable device [66], [73]; (b) – Out-of-plane deformation due to a pre-strain in elastic membrane causing a wavy surface deformation [74]; (c) – Mesh pattern composed by several micro beams that twist buckle out-of-plane when deformed [67].	22
Figure 13 – Stretched kirigami sensor [67]. As the sensor is stretched the micro-beams twist and bend out of plane leading to positive and negative strains in different sections of the metal layer. The tension is represented by the plus signal, while the compression is represented by the minus signal.	22
Figure 14 – Manufacturing process of a kirigami-patterned stretchable device composed by CNTs embed inside a PDMS layer [71].....	23
Figure 15 – Manufacturing process of a kirigami-patterned stretchable device, (a), using clean room techniques, (b) [71].	24
Figure 16 – Materials (a) and Laser micromachine (b) used in the manufacturing process of the robogami finger structure. In (b), (a) represents the laser head, (b) the scanner, (c) the camera and (d) the moving stage.....	28
Figure 17 – Initially the layers are aligned, stacked on a jig and then heat pressed (a) resulting on the finger structure presented in (b). Then the outer frame used to align the layers is cut using a UV Laser. As a result, the joints are released.	29
Figure 18 – Manufacturing process of the tendon-driven robogami under-actuated gripper with adjustable stiffness joints.	30

Figure 19 – Final structure of the finger. Zoomed in the right side of the figure is the castellated pattern indicating the gap and the height of the teeth that allows adjusting the range motion of the joints.....	30
Figure 20 – The modulus of elasticity of the SMP changes orders of magnitude over the glass transition temperature ($T_g=55^\circ\text{C}$)[78].....	32
Figure 21 – Embedding process of the stretchable heater inside the SMP Layer: (a) SMP pellets are transformed into SMP sheets, (b). The stretchable heaters is then embedded in between the two SMP sheets using spacers, (c), resulting in the final structure, (d).	32
Figure 22 – ASL manufacturing process: A stretchable hater is embedded between two SMP sheets (a). A glass fiber frame is bonded to the SMP layer and the heater (b). The silicone rubber is poured into the structure filling the empty spaces (c). Finally, the aligning outer frame is cut, releasing the heater, (d) and making the device stretchable (e).	33
Figure 23 –Schematic of the finger designed and the actuation of the second joint from a cross section side of view. The schematic of the finger with its second joint at an angle θ_2 is presented to illustrate the displacement of the tendon. The point of interaction between the tendon and the glass fiber layer is magnified to show the tendon displacement and the path used to calculate (7) and (8).	35
Figure 24 – Conceptual under-actuated finger.....	37
Figure 25 – Layout of the proposed design for the device, (a). The structure is composed by 5 serpentine paths and 4 contact pads. Besides these features, it is possible to observe two T-shapes in upper and lower middle of the design. Their function is to ensure the electrical insulation between the two pairs of contact pads, so that the resistance can be measured using those contact pads (upper pair and lower pair). (b) Equivalent circuit for the 5 serpentine paths.	40
Figure 26 – Each serpentine path is composed by 23 micro beams with the dimensions shown in Table V.....	41
Figure 27 – Illustration of the cross section of the layers on top of the wafer. The process starts with a 10cm diameter wafer (a). Then, a WTi and Al layer are sputtered (b). Next, a polyimide coating is performed (c). Finally, the metallic layers that compose the serpentine metallic path are sputtered (d). The heights of the layers are not at scale.	43
Figure 28 – Layout transferred during the DWL patterning. This mask will be transferred using a laser and will pattern the photoresist that allows defining the metallic layers that will compose the structure of the device.....	44

Figure 29 – Illustration of the photoresist reflow process. If the reflow is not performed, then, during the metal etching process of the underneath metallic layers fences can occur due to accumulation of particles on the corners of the interface between the two layers (a). If the reflow is performed the curvature of the top surface of the photoresist will prevent particle’s accumulation in the interface between the two layers (b). 45

Figure 30 – Illustration of the cross section of the layers to define the serpentine path. A photoresist coating is initially performed (a). Then, the photoresist is patterned using a DWL technique exposing the metallic layers underneath (b). An ion beam etching patterns the metallic layers exposed (c). Finally the photoresist used as sacrificial layer is stripped (d). 46

Figure 31 – Comparison between the dimensions of the design on the CAD (upper images) and the dimensions of the structure observed under the microscope (lower images). 47

Figure 32 – Profilometer measurement in order to determine the step height of the metallic layers. 47

Figure 33 – Illustration of the layers cross section prior to the photolithography step. A polyimide layer is initially coated (a) and a silicon layer is sputtered to act as a hard mask (b). 48

Figure 34 – Layout for the second photolithography step. This mask will be transferred using a laser that will pattern the photoresist defining the structure of all the polyimide layers previously coated. In order to align this design with what has already been manufactured, alignment crosses are used. 49

Figure 35 – Illustration of the cross section of the layers after the second photolithography step. The heights of the layers are not at scale (a). Microscopic observation of the photoresist patterned after the second photolithography step. As can be seen in the zoomed image the vertical lines in between different serpentine paths correspond to the location where the polyimide will be etched to define the mesh pattern for the stretchable structure. 49

Figure 36 – Illustration of the cross section of the layers after the mesh pattern is defined. The SiO₂ is etched to provide access to the polyimide layer (a). The polyimide layer is then etched, defining the mesh pattern and providing access to the contact pads (b). Finally, the sacrificial layers are etch (c) and stripped (d). The heights of the layers are not at scale. 50

Figure 37 – Illustration of the cross section of the layers after the remaining SiO₂ is etched (a). As can be seen the metallic layers that compose the contact pads were also etched,

which was not expected. The heights of the layers are not at scale. Microscopic observation of the contact pads after the SiO₂ and polyimide etching process (b). As can be seen in the figure above, the contact pad (at the left upper corner) does not possess any metal left. 51

Figure 38 – Layout for the third photolithography step. The mask will be transferred using a laser and will pattern the photoresist that will define the structure of the new contact pads (shown in red). 51

Figure 39 – Illustration of the cross section of the layers after the new photolithography step. Initially, the photoresist is coated (a) and then exposed and developed (b). The polyimide layer is etched where the photoresist was removed (c). Finally, the remaining photoresist is removed (d). The heights of the layers are not at scale. 52

Figure 40 – Microscopic observation of the new L-shaped contact pads. The metallic layer is shinier indicating the presence of metal. 53

Figure 41 –Illustration of the anodic dissolution setup and its working principle. 54

Figure 42 – Final stretchable heater. Microscopic observation of the stretchable device. In the right side of (a) one of the five serpentine paths is zoomed in. In (b) is illustrated the cross section view of the layers that compose the final device. 55

Figure 43 –Stretchable mesh. The mechanical deformation causes the micro beams to twist out-of-plane and bend about their axis of lowest moment of inertia, which requires less energy leading to positive and negative strain in different sections of the metallic layer. Since the metallic layer is uniform and the micro beams present always the same dimensions the different sections of the metal layer in tension and compression cancel each other out, making the device rather insensitive to strain. 56

Figure 44 –Equivalent circuit for measuring the resistance of the device when long wires are connected to it [91]. 57

Figure 45 –Equivalent circuit for measuring the resistance of the device using Kelvin’s method [91]. 57

Figure 46 –Equivalent circuit for measuring the resistance of the device using Kelvin’s method and having into account the effect of the wires resistance for the voltmeter connection. Although the long wires introduce a new resistance, the current that flows through these wires is almost zero and so its effect can be neglected [91]. 57

Figure 47 –Assigning different duty cycles for the input PWM signal allows achieving different steady temperatures. 59

Figure 48 – **Repeatability** and **variability** test the stretchable heaters. The **resistance increases linearly** with temperature according to the equations shown on top of the chart. Each point represents 3 tests for a given temperature achieved by a duty cycle assigned value. The error bars represent the standard deviation per set of 3 tests. The blue dashed line represents the repeatability results while the red line represents the variability results. 61

Figure 49 –The temperature and mechanical deformation effects on the resistance of the heaters were studied by initially activating the heater during 120s, after which a bending motion was applied three times, as zoomed in the left figure. 62

Figure 50 – Stiffness of the ASL as a function of its temperature. The shaded area shows the standard deviation of the data points [4]. 62

Figure 51 – Tactile sensors considered to be integrated on the tendon-driven robogami under-actuated gripper: (a) – TakkStrip; (b) – SingleTact; (c) – FSR400 Short. 63

Figure 52 – When the heaters thermally activate the ASL layers the finger structure is heated as well due to the thermal conductivity of the glass fiber layers. 64

Figure 53 – Flowchart of the protocol defined for the tactile sensors comparison. 66

Figure 54 – Electronic circuit used to acquire the voltage across the thermistor. 67

Figure 55 – Setup to test the temperature and loading effects on the capacitive sensors. The sensor is placed on top of a tile structure with the same glass fiber structure as the fingers and a thermistor is placed near the sensor to acquire the temperature (a). A 3D printed cup ensures that the weight positioning is kept constant during all tests (b). 68

Figure 56 – Test results comparing FSR400 (a) and SingleTact capacitive sensors (b) under different loading and temperature conditions. Each test was performed three times. The red dashed curve represents the data acquired at $T=25^{\circ}\text{C}$ while the blue lined curve represents $T=60^{\circ}\text{C}$ 69

Figure 57 – Flowchart of the protocol defined for the tactile sensors characterization. For each weight and temperature, five trials were performed. During those five trials the sensor output during the heating and cooling process was acquired. 70

Figure 58 – Test results for the SingleTact capacitive sensors under different loading and temperature conditions. Each set consisted of five trials in which the heating and cooling processes were recorded. 71

Figure 59 – Since in good approximation the sensor output is a linear function of the loaded weight, the relation between the weight and sensor output can be found for each temperature. 71

Figure 60 – Minimum radius detected by the contact sensors. The left figure, (a), represents the schematic with the dimensions for the test performed in the right figure, (b).	73
Figure 61 – Final structure of the tendon-driven robogami under-actuated finger. Four tactile sensors and thermistors were placed at the tiles of each finger.	74
Figure 62 – Data Frame of an I ² C communication [112]......	74
Figure 63 – Multiplexer circuit with voltage follower to measure the voltage drop across each thermistor.	76
Figure 64 – Tendon-driven robogami under-actuated gripper with adjustable stiffness joints and tactile sensing.	76
Figure 65 – Adjustable modes of operation are accomplished by adjusting the ASLs stiffness. A power grasp mode is achieved by activating joints 2-5 (a), while a precision grasp mode is achieved by activating only joints 2 and 3 (b).	77
Figure 66 – Grasp of foam with different stiffness settings. If the base compliance is stiff, (a), the gripper applies a large force, deforming the foam. However, if the compliance at the base is soft, the contact force is limited and when the object is contacted, the base joint adjusts itself, (b) [2].	78
Figure 67 – Model simulations results for power , (b), and precision grasps , (d). The results are compared to the expected configuration (a) and (c).	81
Figure 68 – Flowchart for studying the contact forces with different grasp configurations....	82
Figure 69 – Power grasp allows lifting heavier and larger objects by enveloping them between the robotic fingers (a). As a result, contact forces increase from the base to the tip of the finger. The continuously increasing tendon displacement increases the contact forces but at the cost of losing two contact points (b).	83
Figure 70 – Precision grasp modes allows handling smaller and delicate objects by grasping them between the distal phalanxes (a). Objects with 50mm (black curve), 60mm (red dashed curve) and 70mm diameter (blue curve) were grasped and their contact forces acquired (b).	83
Figure 71 –Precision grasp of 50mm cylinder. Initially the gripper was able to handle the weight attached to the object (1). A 32gm weight was added in (point 2) and the gripper kept the object in position. At point 3 a new 32gm weight was added. From that point the gripper was not able to secure the object, causing it to fall.	84
Figure 72 –Proposed design for future ASLs. The puzzle outer frame structure allows to easily replace the ASL if damaged.....	88
Figure 73 –Schematic showing how contact forces can be calculated on future simulations.	91

Figure 74 – Schematic of the ASL elongation with the dimensions necessary to calculate the elongation.....	105
Figure 75 – Methods to improve the adhesion to the previous layers fabricated. In this case, since the new coating will be performed on top of aluminium, the best option is to perform a thermal dehydration on the wafer’s surface.	112
Figure 76 – Methods presented to improve the adhesion to the previous layers fabricated. In this case, since the new coating will be performed on top of metallic layer, the best option is to perform a thermal dehydration on the wafer’s surface.	113
Figure 77 – Process to choose the appropriate recipe for coating the photoresist. The coating option allows to thermally dehydrate the wafer’s surface to improve the adhesion. The recipe is also chosen having into account the desired photoresist thickness.	113
Figure 78 – For the laser machine, the dose used by the laser to correctly transfer the pattern has to be set according to the photoresist thickness.	113
Figure 79 – The recipe for developing the exposure photoresist is set according to the photoresist thickness. As can be seen, for 2µm of photoresist, the total contact time of the photoresist in the wafer with the developer solution is 81s.	114
Figure 80 – Recipe’s available for the physical resist strip. In this case, to ensure that the crust of the photoresist is properly etched 1min exposure to the oxygen plasma is performed.	114
Figure 81 – Schematic description of the process performed to chemically strip the remaining photoresist.	114
Figure 82 – 2 nd Order Butterworth active filter with Sallen-Key topology.	117
Figure 83 – Gain and frequency response of Butterworth, Chebyshev and Elliptic filters....	118
Figure 84 – Second order low pass-filter amplitude response.	118
Figure 85 – Schematic of the electronic circuit that activates and measure the resistance of the heater.	119

LIST OF TABLES

TABLE I – Fully-actuated robotic hands comparison.	7
TABLE II – Under-actuated robotic hands comparison.....	10
TABLE III – Shape Memory Polymer stimulation methods.....	16
TABLE IV – Challenges and approaches to solve them according to literature review and what is still to be done.....	25
TABLE V – Micro beams dimensions for each of the serpentine paths. The resistance of each serpentine path is given by equation (21).....	41
TABLE VI – Resistance values for each of the serpentine paths that compose the structure of the devices.	41
TABLE VII – Tactile sensors characteristics for comparison.....	65
TABLE VIII – Validation results from the model prediction.	72
TABLE IX – 74HC4051 Logic Table.	75
TABLE X – Pseudo-code for simulating the free motion of the tendon-driven robogami under-actuated gripper	78
TABLE XI – Pseudo-code for simulating the free motion of the tendon-driven robogami under-actuated gripper	89

LIST OF ABBREVIATIONS AND ACRONYMS

ACK	Acknowledge
ASL	Adjustable Stiffness Layer
CNT	Carbon Nanotubes
DRIE	Deep Reactive Ion Etching
DIP	Distal Interphalangeal
DoF	Degree of Freedom
DWL	Direct Writing Laser
HF	High Frequency
I²C	Inter-Integrated Circuit
ICP	Inductive Coupled Plasma
IP	Interphalangeal
LED	Light Emitting Diode
MP	Metacarpo-phalangeal
NTC	Negative Temperature Coefficient
Op Amp	Operational Amplifier
PCL	Polycarpolactone
PDMS	Polydimethylsiloxane
PTFE	Polytetrafluoroethylene
PTC	Positive Temperature Coefficient
PIP	Proximal Interphalangeal
RTD	Resistance Temperature Detector
SCL	Serial Clock Line
SDA	Serial Data Line
SMA	Shape Memory Alloy
SMP	Shape Memory Polymer
RTC	Rigidity Tunable Composites

CHAPTER 1

INTRODUCTION

This thesis presents the work developed during the past year in the Bio-inspired Robotic Devices Lab (BiRD Lab) at University of Minho in collaboration with the Reconfigurable Robotics Lab (RRL) at École Polytechnique Fédérale de Lausanne, in Switzerland.

This work addresses to the field of the under-actuated grippers, through the implementation of under-actuation concepts. The **ultimate goal** of this research is to **initiate the study of effective grasp configurations**, where **different stiffness's are achieved through temperature modulation** of an adjustable stiffness layer that composes the manufactured tendon-driven robogami under-actuated gripper. In this context, **contact sensors are integrated to provide feedback and information about the contact forces** while grasping different sized objects.

Ultimately, a **control strategy based on the feedback provided by the contact sensors** can be used to **adjust the stiffness of the joints** and the **tension of the actuation source** that drives the gripper to **improve and ensure safer grasps and interaction between the gripper and the surrounding environment**.

1.1 Motivation, goals and problem statement

Compared to directly driven fully-actuated systems, under-actuated systems offer several advantages, such as simple and compact design, simple actuation and control and inherent softness. However, the simplicity of these systems comes with the cost of limited stable configurations and reduced dexterity [1]. Thus, the **goal** of this project consists on **designing and manufacturing a tendon-driven robogami under-actuated gripper with tactile sensing and adjustable stiffness joints to study effective grasps configurations** achieved by adjusting the joints stiffness of the gripper, thus ensuring a safe interaction with the surrounding environment.

One of the challenges of under-actuated grippers is their **fabrication using fast and low-cost manufacturing processes** that allow reducing the overall cost production of them [2]–[4]. In addition, the design of a simple actuation source is also desirable since it can reduce the computation time to actuate the joints and the weight of gripper. Another challenge faced on under-actuated grippers, consists on **ensuring a safe interaction between the gripper**

and its surrounding environment. The fingers shape conformity to an object is especially advantageous and easily achieved through the redundant number of degrees of freedom that characterize under-actuated grippers. Thus, the input actuation torque is distributed between the multiple joints that compose the gripper, leading to a contact force distribution applied in proper points and directions. However, a compromise between the compliance and the force output must be achieved in order to properly secure an object with a stable grasp. Finally, as already supra mentioned, **under-actuated grippers present limited configurations.** Thus, **acquiring and analyzing information** not only **about loaded area and contact force**, but also about slip perception between the robotic gripper and the object being manipulated **is needed as a safety complement.** Such system should also be compatible with robogami layer-by-layer manufacturing process.

The manufacturing **cost and time consuming** challenge is easily solved using **robogami platforms.** Robotic origamis, robogamis, are planar and foldable robotic platforms that use fast and precise fabrication methods using a UV laser to micro machine quasi 2-D layers. Such fast and low-cost manufacturing process allows reducing the overall cost production of the gripper and integrate multiple functional layers that can be scaled and customized, as first presented by Firouzeh, A. [2, 4]. To **control the compliance and power distribution between the joints, an adjustable stiffness layer is manufactured.** The adjustable stiffness layer is composed by a stretchable heater that thermally activates a shape memory polymer, adjusting its stiffness and hence the compliance of the gripper by deforming a compliant part of the finger structure that connects two rigid segments [3, 4]. In addition, the adjustable stiffness layer allows setting different grasp configurations to the gripper by activating only the desired joints. Lastly, **to study effective grasp configurations** capable of **solving the problem of limited stable configurations** achieved by under-actuated grippers, a **tactile sensing system** compatible with the layer-by-layer manufacturing process is integrated to **provide the necessary feedback to study grasping different sized objects using different configurations.**

1.2 Overview of the research

Under-actuated robotic grippers were introduced in the robotic field as a grasping solution, contrarily to the robotic hands which were normally proposed to manipulate, in an attempt to emulate the human hand. Due to their simplicity considering architecture and control, under-actuated grippers were seen as a different approach, as referred by Birglen, L. [5] and Bicchi,

A. [6]. The first under-actuated grippers were simple structures consisting of several links, pulleys and cables transmission mechanisms to employ rigid joint coupling and actuate all segments [7, 8]. Later on, mechanisms to adjust the compliance of the under-actuated grippers aiming to increase their safety and simplify their actuation topologies were introduced. Initially, several authors proposed the use of springs to achieve the desired compliance, since these structures are inherently soft, allowing the self-adaptability of the fingers to the objects being grasped [9]–[12]. However, other authors proposed introducing structural compliance inside continuous structures, which led to diverging designs with attractive features. In some proposed solutions the finger was composed by a single structure [13], while in others the exploitation of materials properties to manufacture adjustable stiffness structures would allow further simplification of the actuation systems employed [14]–[18]. At this point, smart materials, like shape memory polymers gained the scientific community attention due to their considerable change in their modulus of elasticity around the glass transition temperature, high shape-recovery and ease of processing. Several methods to stimulate these polymers started being exploited and even integrated in under-actuated grippers [4, 15, 19, 20]. For research purposes of this dissertation, the use of stretchable heaters or embedded electrical heating wires were the most captivating due to their high response and ease of integration inside SMP structures, which is desirable in the under-actuated gripper being develop on this thesis. More recently, tactile sensors started being integrated in under-actuated grippers, demonstrating their importance to perceive the interactions between the gripper and the surrounding environment, either to evaluate pressure distribution [18], obtain rough information about the object shape [21] or to evaluate the role of external forces [22]. More importantly, in [23, 24], tactile sensors are used to study contact forces addressed to the implementation of control strategies.

1.2.1 Goals and research questions

The **ultimate goal** of this research is to **initiate the study of effective grasp configurations** using a **tendon-driven robogami under-actuated gripper**, with adjustable **stiffness joints** and **tactile sensing**. Thereby, it is necessary to achieve the following goals:

Goal 1: The first step is to conduct an extensive survey on the state of art related to under-actuated grippers. This goal will provide the necessary information concerning problems, main challenges and solutions developed so far in this field.

Goal 2: The second step is to **manufacture a robust tendon-driven robogami under-actuated gripper** using the robogami platform to integrate multiple functional layers and reduce the overall cost of production of the grippers.

Goal 3: Then, the design and **manufacturing** process of **stretchable heaters** to modulate the stiffness of a shape memory polymer is performed. Since the stiffness of shape memory polymers is directly related to their temperature, the possibility of using the heaters themselves as temperature sensors is exploited. This goal, also allows **manufacturing** an **adjustable stiffness layer** to adjust compliance and achieve different grasping configurations.

Goal 4: The fourth step is to **integrate a tactile sensing system to study effective grasp configurations** using the feedback provided by them. The tactile sensors should be compatible with the manufacturing process of the fingers and present a good response and behaviour under the operating conditions of the gripper.

Finally, during this dissertation, the following research questions (RQ) are expected to be answered:

RQ1: Is it possible to produce an under-actuated gripper with adjustable modes of operation and integrated tactile sensing using fast and low-costs manufacturing processes?

RQ2: Is the clean room manufacturing process of stretchable heaters advantageous?

RQ3: Can stretchable heaters be used as temperature sensors as well?

RQ4: Can tactile sensors be used to improve grasping quality and ensure safer interactions between grippers and the surrounding environment?

1.3 Contributions to knowledge

During the course of this dissertation, the following contributions were made:

- 1) A tendon-driven robogami under-actuated gripper with adjustable stiffness joints and integrated tactile sensors was manufactured using fast and low-cost manufacturing processes.
- 2) A clean room manufacturing process for stretchable heaters was developed. Such heaters were then characterized and their repeatability behavior and variability between

different heaters of the same batch were studied. Also, the possibility of using stretchable heaters as temperature sensors is introduced during this dissertation.

- 3) Initiate the study of effective grasp configurations of a tendon-driven robogami under-actuated gripper in different sized objects. The multiple configurations are achieved by modulating the stiffness of the joints while tactile sensors provide the contact force data relative to the grasp being performed.

Based on this dissertation the following publication has been submitted:

- 1) – M. Sanches, A. Firouzeh, C. P. Santos, J. Paik, “Under-actuated gripper with Adjustable Stiffness Joints and Tactile Sensing”, in International Conference on Robotics and Automation (ICRA2019), 2019.

1.4 Thesis outline and structure

This dissertation is composed by 6 chapters, each one revolving around a section of the developed work and organized as follows.

Chapter 2 has a state of the art of under-actuated grippers. Initially, the advantages of under-actuated systems relative to fully-actuated systems are presented. Then, the evolution from initial under-actuated grippers to more complex architectures integrating sensorial systems and compliance mechanisms are reviewed in order to identify and understand the problems and solutions developed so far.

Chapter 3 presents the manufacturing process of a tendon-driven robogami under-actuated gripper with adjustable stiffness joints and the mathematical model of such gripper.

Chapter 4 focuses on the manufacturing process and characterization of the stretchable heaters.

Chapter 5 contains the comparison of tactile sensors, the choice of the most adequate one to the addressed problem and its integration onto the developed under-actuated gripper. Also, based on the operating conditions of the gripper the tactile sensors characterization is performed and a model capable of calculating the contact forces is developed and validated. Then, the free motion of the under-actuated gripper is simulated while the integrated sensors are used the study of effective grasp configurations. Finally, the results are presented.

Chapter 6 contains the conclusion of this dissertation and future work.

In the appendixes I to III mathematical models deductions are explained with further detail. Additionally, appendix IV presents the detailed outlined process for stretchable heaters, while appendix V provides insight on the electronic circuits to measure their resistance.

CHAPTER 2

LITERATURE REVIEW

Nowadays, robots have undergone a long way, but they have still only accomplished a fraction of the tasks and performance that they are mechanically capable of. Research has provided advanced control technologies and several sensing systems capable of achieving higher perception to detect/localize objects and understand the surrounding environment. However, robotic grippers are still a long way from performing basic object manipulation tasks with the dexterity and versatility of human hands [25].

2.1 Fully vs under-actuated grippers

Matching the performance of human hands is a formidable challenge and the design of robotics hands for dexterous grasping and manipulation has historically been important, either to match the human hand in terms of dexterity and adaptability or to equip dexterous manipulators [26]. Nevertheless, the dexterity (i.e. the ability to perform highly precise operations with visual/perceptual/tactile feedback) of robotic hands has always been more limited than a human hand [5], which is capable of performing complex grasping and manipulation tasks on a wide variety of objects in unstructured environments [1].

2.1.1 Fully-actuated robotic hands

Several authors proposed pioneer designs of robotic hands, such as the Okada Hand [27], the Stanford/JPL (Salisbury's) hand [28], the Utah/MIT Hand [29] and the DLR Hand [30], [31]. All these anthropomorphic inspired robotic hands work based on fully-actuated systems where the number of degrees of freedom is equal to number of actuators used to achieve the dexterity of human hands. A small comparison between them can be found in Table I.

TABLE I – Fully-actuated robotic hands comparison.

Name	Fingers	DoF	Drive	Figure
Okada Hand [27]	3	11	tendons	1 – (a)
Salisbury's Hand [28]	3	9	tendons	1 – (b)
Utah/MIT Hand [29]	4	16	tendons	1 – (c)
DLR Hand 1 [30]	4	12	mechanical	1 – (d)
DLR Hand 2 [31]	4	13	mechanical	1 – (e)

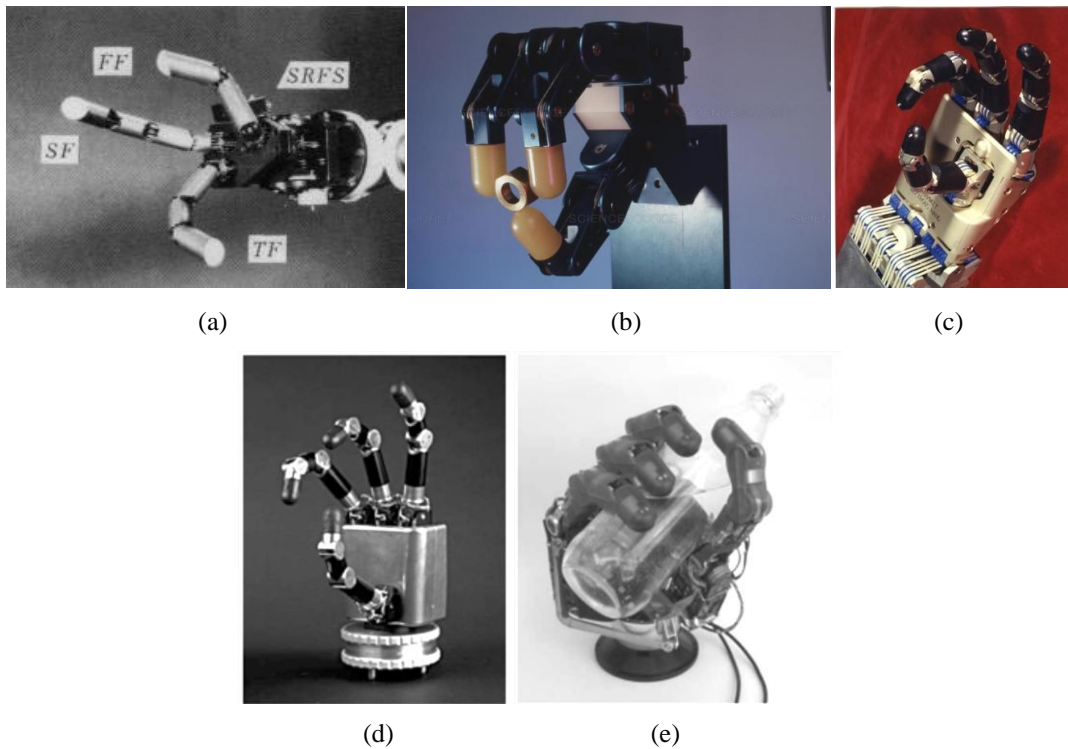


Figure 1 – Fully-actuated robotic hands: (a) – Okada Hand [27]; (b) – Salisbury's Hand [28]; (c) – Utah/MIT Hand [29]; (d) – DLR1 Hand [30]; (e) – DLR2 Hand [31].

One of the major problems with fully-actuated systems is the number of actuators needed. In the Utah/MIT Hand a tendon system is used to individually control each joint. However, since a tendon can only pull and not push, the actuation is uni-directional, meaning that $2n$ actuators are required to control n DoFs [5]. For the Salisbury's Hand the use of passive elements alongside with a tendon system allowed reducing the number of actuators to $n+1$ to control n DoFs [32]. Despite the number of actuators was reduced there was still problems regarding the actuation method, namely the fact of the tendon transmissions being limited to small force and exhibit large internal friction [5]. Thus, different mechanisms were also exploited, like linkage and gear transmissions, such the ones used in the DLR Hands. In such cases, the importance of miniaturization of electric motors and sensory systems allows saving space, which would not be a problem if a tendon-driven mechanism was used. Another problem of fully-actuated systems is the amount of sensors needed in order to properly grasp an object. Since each joint needs to be individually actuated position sensors, joint angle sensors, torque sensors or contact sensors needed to be integrated [30, 33]. As a result, the weight of the finger structure increases along with the computational power needed to acquire all the signals and adjust the fingers position [1, 33]. The mentioned problems explain the lack of success of fully actuated system.

In summary, the difficulties/disadvantages faced to implement such systems are [1]:

- The requisites needed on the mechanical sophistication topologies, i.e., kinematic arrangements and mechanical actuation systems;
- The need for high-fidelity sensing, causing complex architectures to be implemented;
- Demand for advanced and complex control schemes to individually control each degree of freedom.

2.1.2 Under-actuated robotic hands

More recently, a new concept of mechanical design has started to be explored: **under-actuation**. The under-actuation principle consists in using fewer actuators than the number of DoFs in the system. The employing rigid joint coupling using gear transmissions, cables or hinge layers that connect all joints allows reducing the actuator requirements, decreases the production costs and avail more tractable sensing and control schemes, saving weight and computing power [34]. Moreover, the redundant number of DoFs and the use of passive elements, like springs or smart materials to adjust the stiffness of the joints allows the mechanical adaption of the finger to the shape of the object being grasped providing inherent softness and consequently increasing safety interaction between the under-actuated robot and the surrounding environment [5, 26]. The shape conformity of the fingers can be used to distribute the actuation torque to a larger contact surface allowing the combination of secure grasps with delicate handling. Such property is especially important for food processing [35] or medical robots [36].

The advantages presented by the under-actuated mechanical design led several robotic hands to be upgraded from fully-actuated systems to under-actuated systems, like the RTR Hand. In its first version, presented by Carrozza *et al.* in 2002 [37], Figure 2 – (a), the RTR1 Hand consisted in three fully-actuated fingers to provide a tripod grasp: two identical fingers (index and middle fingers) and a thumb. The actuation system for the two identical fingers was based on two microactuators integrated in the hand structure to drive the metacarpophalangeal (MP) and the proximal interphalangeal (PIP) joints, respectively. The distal interphalangeal (DIP) joint was passively driven by four-bars link connected to the PIP joint. Concerning the third finger, the actuation system was based on microactuators to actuate two DoFs at the MP and interphalangeal (IP) joint. In the presented version, the grasping tasks comprised two phases: a shape-adapting initial phase, where the finger actuator system allowed the finger to morphologically adapt to the characteristics of the grasped object, and a

second grasping phase, where the second actuator system provided thumb opposition for grasping.

The next generation prototypes, RTR2 Hand, Figure 2 – (b), and SPRING Hand, Figure 2 – (c), presented by Zecca *et al.* in 2003 [38] and Carrozza *et al.* in 2004 [39], respectively, used an under-actuation approach. The RTR2 Hand presented an under-actuation design between fingers by using a movable pulley technique consisting of two DC actuators to move the hand: one for the thumb and one for the other two three-phalanx fingers [38]. The latter version used a slider as the fundamental element of the transmission mechanism providing flexion and extension of the fingers due to its two-way linear motion. Furthermore, a differential mechanism based on compression springs allowed controlling the movement of the multiple DoFs using only a single actuator [39]. The springs allowed modulating the stiffness of the finger and return it to a pre set position. Table II presents other examples of under-actuated robotic hands that can be found in the literature.

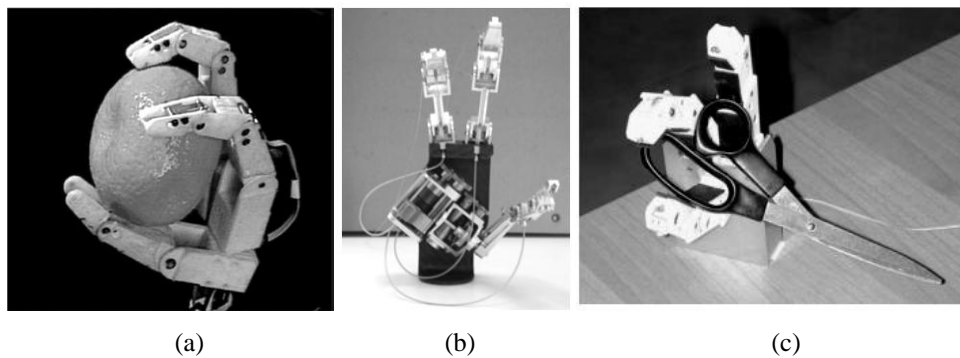


Figure 2 – Evolution from the RTR Hand: (a) – RTR1 Hand [37] was a fully-actuated robotic hand, while the RTR2 Hand [38] , (b), and the SPRING Hand [39], (c), were under-actuated. The difference between the two latter versions was the transmission mechanism used to drive the fingers.

TABLE II – Under-actuated robotic hands comparison.

Name	Fingers	DoF	Drive	Figure
RTR Hand 2 [38]	3	9	tendons	2 – (b)
SPRING Hand [39]	3	9	tendons	2 – (c)
AMADEUS hand [40]	3	n.a.	hydraulic	-----
BarettHand BH8 [41]	3	7	mechanical	-----
SARAH Hand [42]	3	10	mechanical	-----

n.a. – not available

2.2 Under-actuation as a solution to grasping

Despite the simplicity of robotic hands systems increased with the introduction of under-actuated robotic hands, mimeting the human hand still leads to complex systems. As pointed out by Birglen *et al.* [5] and Bicchi, A. [6] emulating the human hand is a possible solution towards manipulating objects, but not the best solution, since physiologically is very difficult to develop a control scheme capable of controlling every joint to achieve the desired dexterity. Furthermore, it is important to refer that such complex architecture, as presented in most robotic hands, along with demanding control schemes may lead to poor grasping performances [1]. Consequently the problem of manipulating an object started to be approached differently as a grasping problem. This way, the object would be grasped and subsequently prevented from moving. Thereupon, an articulated system like a robotic arm, where the gripper would be mounted, would be responsible for performing the required manipulation task. This is known by grasping vs. manipulating dilemma: a device intended for grasping is generally unable to manipulate and vice-versa. To obtain both functions is almost exclusive to the human hand and in some cases the robotic devices can outperform the human hand in dedicated applications where no constraints regarding emulating a human hand are necessary. Consequently and alongside with the high costs and computational power requirements of robotic hands, under-actuated grippers became a source of investigation and interest.

Under-actuated robotic grippers offer compact design and simpler actuation and control strategies when compared to robotic hands, but at the cost of limited configurations [6]. The concept of under-actuated fingers is different from the general concept of under-actuation in robotics. Generally, an under-actuated robot is defined as a manipulator with one or more unactuated joints, while under-actuated fingers “use elastic elements in the design of their “unactuated” joints, combined with a transmission system to distribute the actuation torque to the latter joints” [5]. Thus, passive elements such as springs are used to kinematically constrain the finger while the input actuation torque is transmitted to the phalanges through a transmission mechanism system, such as linkages, pulleys and tendons.

The first explicit description of under-actuation applied to robotic fingers was presented by Hirose, S. and Umetani, Y. in 1978 [7], Figure 3 – (a).

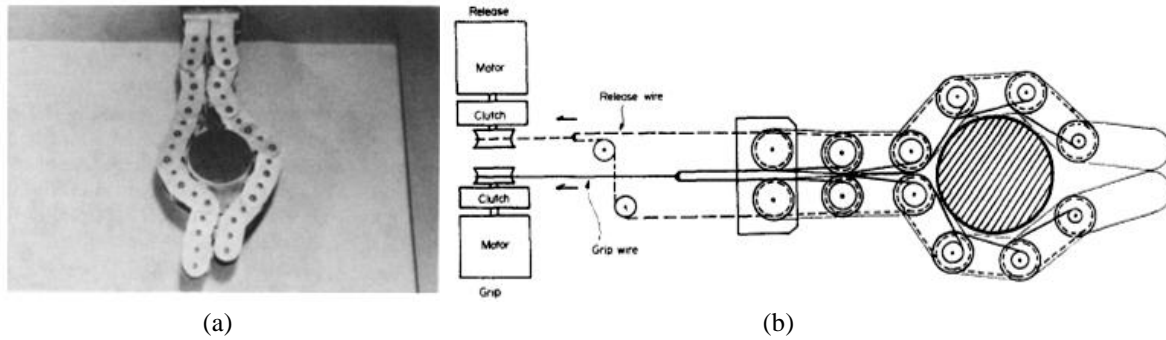


Figure 3 – First version of an under-actuated gripper, presented by Hirose, S. and Umetani, Y. [7]. The soft gripper conforms to an object thanks to the redundant number of DoFs – (a). The mechanism presented consisted of several phalanges with a cable and pulley driven mechanism – (b).

The prototype, composed by two fingers with ten-phalanx each, used pulleys as a transmission mechanism along with two cables. The employed rigid coupling mechanism actuates all the segments using a traction pair of wires: one for closing and another with constant tension for pulling back the finger, as depicted in Figure 3 – (b). As Hirose, S. and Umetani Y. [7] explained the movement and adaption of the gripper's fingers to an object depends on the size (diameter) of the pulleys and the object, following a series of grasping phases that result in the envelopment of the peripheral shape of the object. Initially, the release wire is pulled with a constant tension and the grip wire is completely loosened. As the grip wire starts to be pulled, the input torque on the fingers start to increase and eventually exceeds the torque on the release wire being applied on the base. Consequently, the finger starts to bend from the base segment of the gripper towards the tip segment. During this process, the links that compose the gripper become in contact with the object. The disposition of each gripper's links is determined by the mechanical contact. Finally, all the links are in contact with the object following its shape, as shown in Figure 4.



Figure 4 – Grasping phase of the soft gripper presented by Hirose, S. and Umetani, Y. [7]. The finger is initially at a resting position thanks to a releasing wire. Once the input torque is applied, the fingers envelop the object distributing the contact forces around the object.

Other examples of under-actuated grippers with simple design can be found in literature, like the one presented by Rovetta *et al.* in 1982 [8], Bin Gao *et al.* in 2016 [43] or Hong, D *et al.*, more recently, in 2017 [44].

2.3 Compliant under-actuated grippers

More recently, merging under-actuated grippers with compliant mechanisms allowed further simplification of the actuation topologies of robotic grippers, decreasing costs production. A desirable and attractive feature of the compliant action of joints resides in the inherent softness being provided to the gripper, which combined to shape adaptation and tolerance to impact of under-actuated robotic grippers, allows distributing the input actuation torque to proper points and directions, ensuring secure grasps alongside with delicate handling [5, 4]. The compliance of robotic fingers can be achieved by substituting the classical revolute joints with different materials, whose stiffness can be adjusted, leading to the deformation of a compliant part of the structure that permanently connects two rigid links.

A simple example was illustrated by Yang *et al.* in 2004 [9] using springs to compose the fingers that were actuated with a tendon-driven mechanism. The tension force applied by the tendon deforms the springs resulting in the desired movement of the fingers. As a result of the inherent softness and compliance, the springs would adapt to the object allowing grasping it. Despite several authors proposed using springs to achieve the desired compliance [10]–[12] another option found in literature is to introduce structural compliance inside a continuous structure. The attractive features of such design are the following ones [4, 6, 13]:

- The finger structure can be seen as one-piece structure, since the phalanges are directly connected by the hinge layer, and so, the manufacturing process cost can be reduced;
- The stiffness of the hinges can be exploited in order to simplify the actuation system. In this case, a single actuation source (e.g. a tendon) can be used to bend a joint pulling in opposition to the hinge stiffness. In this cases, the materials properties allows changing the stiffness of the joints, which compared to designs based on motors and mechanism, results in a more compact and scalable design.

The first attractive feature mentioned above was presented by Lotti, F and Vassura, G. in 2002 [13] where it was developed a manufacturing process of an under-actuated robotic finger using a PTFE (Teflon) material, as depicted in Figure 5. The mechanical properties presented by the material, such as manufacturability, low friction and wear resistance were the reason to chose it. The design of the finger allows setting the limit configuration angle for the bending motion of three elastic hinges (two active and one passive flexure), whose motion was generated by means of double-acting actuators.



Figure 5 – Under-actuated finger composed by Teflon material [13]. The rigid joint coupling achieved by the one-piece structure allows reducing the cost of the manufacturing process – (a). The finger design determines the limit configuration angle for the bending motion of the three hinges – (b).

For the adjustable stiffness joints, multiple solutions have been proposed in literature, taking advantage on the material properties like jamming, phase change in wax or elastic modulus variability in polymers [4].

In 2013, Shan, W *et al.* [16] introduces a rigid tunable composite (RTC) that combines a thermally responsive layer (VHB acrylic elastomer tape) with an elastically soft Joule heating element (liquid-phase Galinstan). When an input signal is applied using a pair of copper shims, the temperature of the thermally responsive layer increases, tuning the rigidity of the layer.

In 2015, McEvoy, M. A and Correll, N. [45] used a thermoplastic, polycaprolactone (PCL), to create structures with a wide range of stiffness. The manufacturing process uses a laser-cut technique and embeds thermistors for sensing and Nichrome wires acting as heating elements, as shown in Figure 6 – (a). Thus, when heated above its glass transition, the polymer elasticity modulus changes orders of magnitude, allowing modulating the stiffness of the structure and hence its configuration, as represented in Figure 6 – (b).

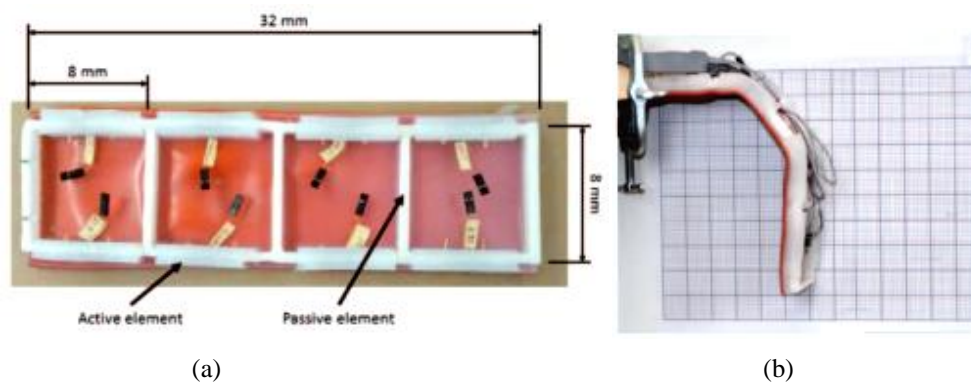


Figure 6 – Adjustable under-actuated finger [45]. The thermoplastic stiffness varies according to the temperature when a signal is passed through Nichrome wires embed inside the PCL layer, while thermistors are used as sensing elements to estimate the temperature of the active PCL layer – (a). As a result, the configuration of the finger can be adjusted – (b).

More recently, the use of variable stiffness structures started to be integrated in the robotics finger structure to increase their compliance and achieve different joints configurations by adjusting the stiffness of the embedded polymers. In particular, shape memory polymers (SMPs) gained interest on the scientific community due to their considerable change in the modulus of elasticity around the glass transition temperature and their high-shape recovery, a desirable feature where a pre set position needs to be reached [4, 14, 46]. Also, the high elastic deformation (capable of standing strains up to 200% times more than most of polymers), low cost, density and temperature range of operation made SMP even more attractive.

Several methods have been proposed to thermally stimulate SMP and adjust its stiffness. Table III summarizes those methods presenting their advantages and disadvantages.

In 2017, Wang. W. and Ahn. S. [14] presented a shape memory alloy-based soft gripper that integrates variable stiffness structure for compliant grasping. The gripper is composed by three identical fingers consisting of two hinges per finger. Each hinge is fabricated integrating a soft composite shape memory alloy (SMA) with stiffness change material (SMP) to achieve multiple configurations. The combination of two SMA wire-actuators and the SMP stiffness layer solves the small actuation force limitations presented by other transmission mechanisms, such as cable and motor-based mechanisms, while maintaining the inherent softness of the gripper. By selectively changing the stiffness of the hinges, achieved by inputting a current through a Nichrome wire embedded in the SMP layer, and actuating the relevant SMA wire a bending moment is created, resulting in the bending deformation to the eccentric side on the low-stiffness hinge segment, Figure 7. As a result the gripper can perform more several shaped grasps with a larger range of weighted objects.

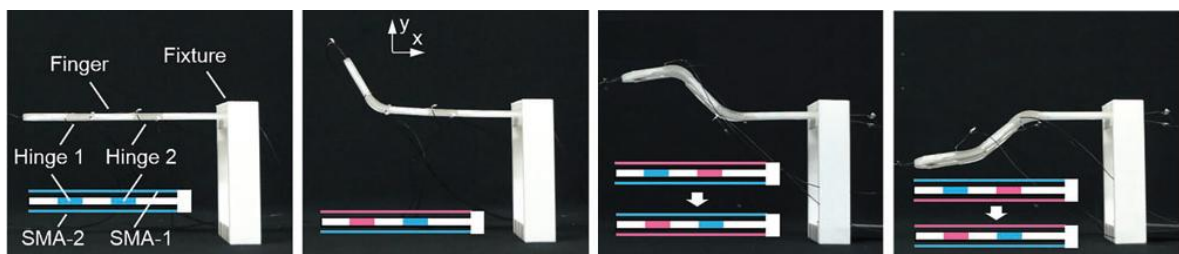


Figure 7 – Shape memory alloy-based soft gripper[14].By selectively activating the stiffness of the desired hinges (red hinges) and actuating the relevant SMA wire (red) the joint to be bent and their bending direction can be chosen.

TABLE III – Shape Memory Polymer stimulation methods.

Stimulus method	Schematic Diagram	Advantages	Evaluation
			Disadvantages
Joule heating by hot gas/water (direct) [46, 47]		<ul style="list-style-type: none"> • Easy fabrication process of SMP 	<ul style="list-style-type: none"> • Low response speed • Necessary equipment to supply hot air/water
Joule heating by embedded electrical heating wire (direct) [15, 16, 19]		<ul style="list-style-type: none"> • High response speed • Easy power supply 	<ul style="list-style-type: none"> • Modified fabrication of SMP structure to embed heating wires or elements
Infrared radiation (indirect)[48, 49]		<ul style="list-style-type: none"> • Remote heating 	<ul style="list-style-type: none"> • Low response speed • Additive fillers may increase SMP's stiffness at soft state
Electric activation (direct) [50]		<ul style="list-style-type: none"> • High response speed • Easy power supply 	<ul style="list-style-type: none"> • Additive fillers may increase SMP's stiffness at soft state • Chemical treatment of the filler is essential
Magnetic activation (indirect) [51]		<ul style="list-style-type: none"> • High response speed • Remote heating 	<ul style="list-style-type: none"> • Equipment to generate HF electromagnetic field, which depending on the robotic application might not be suitable • Additive fillers may increase SMP's stiffness at soft state • Chemical treatment of the filler is essential

More recently, in 2016, Yang, Y. *et al.* [47] presented a pneumatic under-actuated gripper with adjustable stiffness joints using SMP to activate the desired joints, Figure 8. Initially, the SMP is in its glass state ($T < T_g$) with the soft actuator turned off and so, the finger is fully stretched. Using an oven to heat the air surrounding the SMP above its glass transition temperature, T_g , allows a rubber state ($T > T_g$) to be reached, resulting in the bending motion of the SMP structure when compressed air is introduced inside the soft actuator chambers, as illustrated in Figure 8 – (b). Once the desired position has been reached, the SMP can be cooled down until its glass state allowing the fingers to hold and lift objects with large weight.

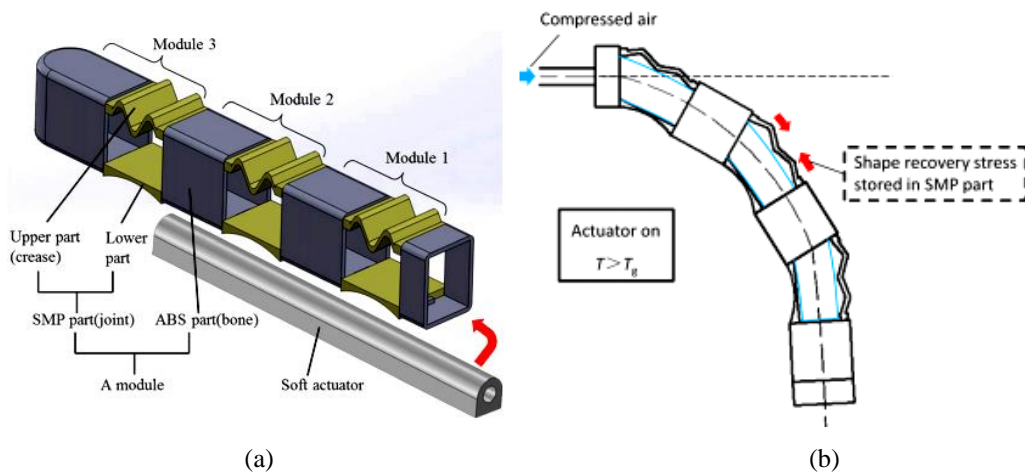


Figure 8 – Pneumatic under-actuated gripper with adjustable stiffness joints[47].The finger structure is composed by an acrylonitrile butadiene styrene (ABS) structure acting as bone. Each bone part is linked to a SMP structure that acts as a joint – (a). A pneumatic soft actuator passes through the structure bending the activated joints, whose temperature is higher than the glass transition temperature of the SMP – (b).

A more efficient approach to heat the SMP layers was presented by Firouzeh, A. *et al.* in 2016 [6], by manufacturing an adjustable stiffness layer. The adjustable stiffness layer consists of a stretchable heater, Figure 9 – (a), embedded between two sheets of SMP, Figure 9 – (b), allowing adjusting the stiffness of the joints and hence achieving different configurations for the fingers to grasp different objects. Furthermore, a glass fiber frame, Figure 9 – (c) acts as a mold for the silicone rubber encapsulation, Figure 9 – (d), that increases the shape recovery of the SMP layer. The manufacturing process of the fingers is an example of how rigid joint coupling is implemented on under-actuated fingers. The folding pattern of a hinge layer composed by a polyimide sheet determines the arrangement of DoFs, which are actuated with a single actuation source consisting of a tendon-driven mechanism. The redundant DoFs provide self-adaptability and inherent softness to the gripper while the adjustable stiffness layer increases safety interaction by adjusting the compliance and the configuration of the fingers to grasp an object [3], [4].

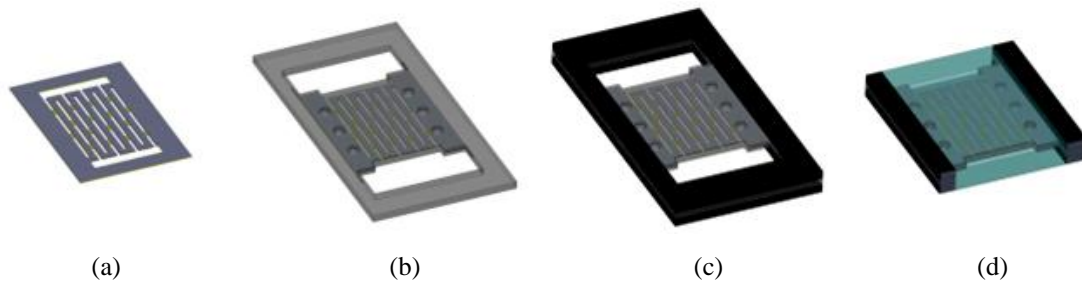


Figure 9 – Adjustable Stiffness Layer manufacturing process[4]. A stretchable heater, (a), is embedded inside two SMP sheets, (b), and two glass fibers frames, (c). Finally, the structure is encapsulated using silicone rubber, (d).

2.4 Under-actuated grippers with tactile sensing

Despite the efforts and proposed solutions to find a compromise between the grasp force distribution and the capability of the fingers to exert the appropriate amount of force on a grasped object, unstable grasps were still occurring. As a consequence, the object would eject or slip from the gripper [44, 52]. Thus, it is important to study effective grasp configurations that ensure that the object is properly secured. So, the integration of tactile sensing systems allows studying the interaction between the objects and the fingers that compose the gripper, improving the safety between the gripper and its surrounding environment.

Several examples of tactile sensors integrated in robotic hands and grippers can be found in the literature, which can have a resistive [53], capacitive [54], piezoelectric or barometer working principle [55]. In 2006, Aaron M. Dollar and Robert, D. Howe [17] presented an under-actuated gripper with joint compliance and several sensing systems, which included contact force sensing. A shape deposition manufacturing process allows integrating miniaturized sensors on the structure of the fingers, resulting in their encapsulation and therefore reducing the likelihood of damage. Such feature is particularly advantageous when fragile components like sensors need to be embedded. Furthermore, as presented by the authors, the layer deposition permits dissimilar materials to be used, resulting in the variation of mechanical parts within the same structure. An example of this advantageous feature in the presented manufacturing process is the use of elastomer flexures to form the joints of the fingers and the reflective layer embed in the soft pads of the fingers. The elastomer flexure of the joints allows the fingers compliance to be adjusted to conform to a wide range of object while minimizing contact forces, while the reflective layer acts as an auxiliary to the tactile sensing system. The tactile sensor is an optical sensor composed by a LED and a photodetector. As the finger applies force to an object, the pad deforms inwards bringing the

reflective inner surface of the finger pad closer to the embedded sensor, causing a change in the detector current.

In 2011, Nagase, J. *et al.* [18] proposed designing a variable stiffness robotic hand using pneumatic soft actuators and integrating tactile sensors to evaluate the pressure distribution. A tendon driven mechanism actuates the joints when the finger is expanded by the compressed air being introduced inside the balloon finger structure. As a consequence a tensile force is created for the tendon to drive. To study the grasping pressure distribution a tactile sensor (I-SCAN; Nitta Corp.) was integrated on the surface of the finger structure. The integrated force resistive sensors consisted on a sensor sheet with special ink resistive electrodes in the desired directions. Thus, the ink resistance changes depending on the amount of pressure being applied on top of the sensor's surface.

In 2013, Tsutsui, H. *et al.* [21] presented an under-actuated robotic hand with integrated tactile sensing with the goal to analyze the data provided by the tactile sensors and obtain rough information about the shape of the object. The robot hand possesses three fingers, each with three joints and a servo motor, which is responsible for the bending motion of the finger, while three torsion springs are responsible for the extending motion of it, as illustrated in Figure 10 – (a). The tactile sensor consists of three pneumatic sensors mounted in front of each robot finger, as shown in Figure 10 – (b). A grasping control is also presented by the authors to ensure a secure grip. The control scheme works based on comparison between the force being measured (F_1) and a threshold for the contact force (F). If $F < F_1$, the servo motor pulls the tendon to increase the contact force while if $F > F_1$ the motor releases the tendon one step decreasing the contact force. The above cycle is performed until $F = F_1$, meaning that a proper grip has been established.

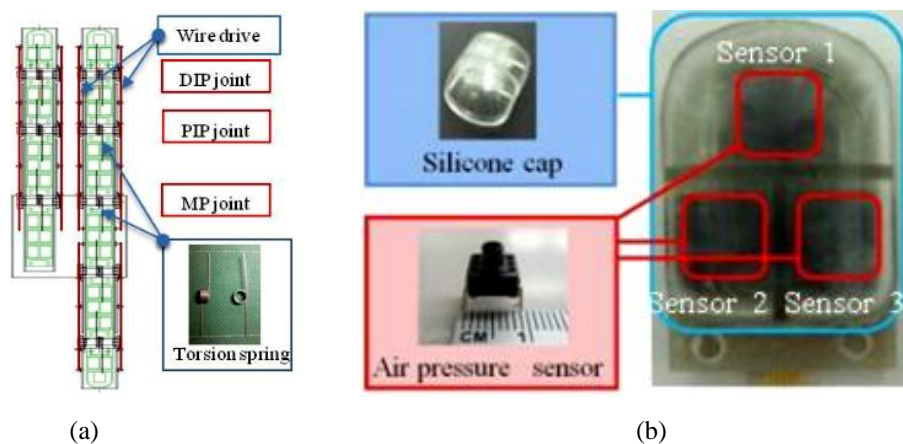


Figure 10 – Under-actuated robotic hand with integrated tactile sensors [21]. A cable driven mechanism and torsion springs are used to actuate the joints – (a), while three pneumatic sensors placed on the tip of the fingers to provide feedback to obtain rough information on the object shape – (b).

More recently, in 2014, Daniel M. Aukes *et al.* [22] presented a compliant under-actuated gripper that integrates tactile sensors, Figure 11, with the objective to acquire data in a wide range of object sizes and heavy weight. Moreover, it was also studied the ability of the gripper to resist high pullout forces for a given input torque and constant tendon tension. Thus, the integrated tactile sensors provided the necessary feedback to understand the resultant forces being applied to objects. The design proposed by the author is composed by four identical robust fingers. The robustness of the fingers is achieved due to an Aluminium structure that supports the moving parts of the finger. A locking mechanism for individual joints, accomplished using electrolaminate brakes, allows different configurations to be performed: spherical, interlaced and pinch configuration. The locking mechanism is composed by a thin dielectric film, which possesses clamping properties, on top of a patterned electrode so that when high voltages are applied, the material thickness changes determining the breaking torque. Such system is advantageous due to its high response to achieve different configurations.

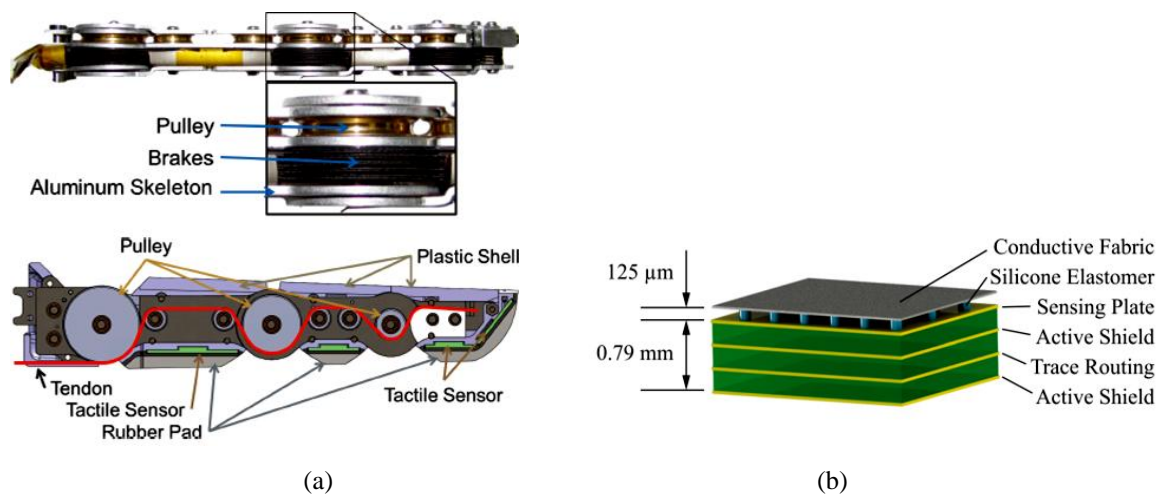


Figure 11 – Compliant under-actuated gripper with locking mechanism and tactile sensors, (a). Eletrolaminate breaks allow configuring the actuated joints using a tendon-driven mechanism. The layers that compose the capacitive sensors are illustrated in (b). A silicone elastomer acts as dielectric layer between a conductive fabric layer and a sensing plate connected to an active shield preventing capacitive coupled currents to interfere on the signal being measured [22].

Concerning the tactile sensory system, capacitive arrays were manufactured. Each sensor is composed by a grounded layer with a silicone rubber sheet and a conductive fabric, as shown in Figure 11 – (b). The dielectric layer is composed by several columns of silicone rubber with 200 μ m diameter, approximately. As a result, when a force is applied at the sensor, its deformation causes a change in the capacitive value being read.

2.5 Stretchable heaters/sensors

As it was previously mentioned, one of the possible methods to stimulate SMP is through Joule heating by embedding electrical wires or metallic layers inside SMP structures. Different conductive materials have been explored for flexible heaters, such as metallic nanowires [20, 56, 57], hybrid nanowires [58, 59], carbon nanotubes [60, 61] and graphene films [62]–[64].

Until now, stretchable devices have been produced using two different strategies. The first one consists of functional conductive material networks, like metallic nanowires [20, 56, 57] or metallic glasses alloys [65], that are attached to stretchable elastomeric substrates, like PDMS or other polymeric substrates, resulting in simple manufacturing processes. Despite demonstrating a wide range of operating temperatures (more than 150°C) [56, 59], chemical stability and mechanical robustness (in some cases capable of standing more than 1000 bending cycles [56, 59]), these heaters can only support low strain percentages [56, 57, 64] until becoming thermally or electrically unstable. Thus, the resulting devices have been shown to be generally limited to tens of percent strains, since for larger strains there is a severe loss of electrical conductivity and stability. Therefore, the **challenge is to minimize the local stress induced by the mechanical deformations**.

The second strategy takes upon a different approach consisting on designing stretchable architectures like fractal-inspired stretchable heaters [66] or mesh patterned heaters [67], **solving the problem of minimizing the induced stress**. Such designs are inspired in the Japanese art of cutting paper, Kirigami, which has been recently used to pattern thin films with arrays of cuts [67]–[72]. In fact, given the limited elastic strain in metals, a pattern that transforms a small strain in the metallic layer into a large displacement is desirable. This patterning of strain-relief motifs allow minimizing the local stresses induced by the mechanical deformation while retaining the electrical properties by changing their structures under deformation.

Several methods have been suggested to transform the bending motion in the metal film into stretch in the sensing elemental. Meander patterns, Figure 12 – (a) achieve this transformation in-plane due to the bending motion of the metal tracks [66, 73]. Another approach consists in out-of-plane deformation due to a pre-strain in an elastic membrane to create of a wavy surface, Figure 12 – (b) [74]. The third method uses a mesh pattern consisting of micro beams which twist buckle out-of-plane under strain and bend about their

lowest moment of inertia axis, Figure 12 – (c) [67]. In the latest, the use of offset rows of slits, enable stretching a material beyond what its normal tensile properties would allow.

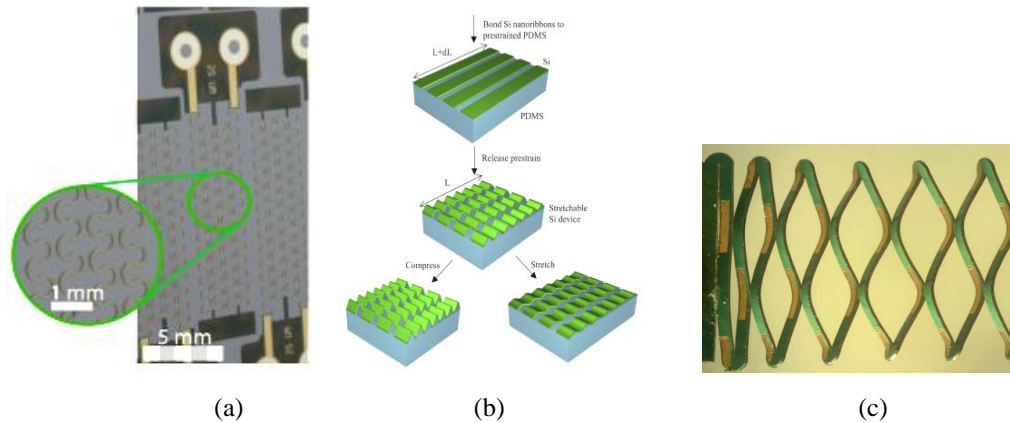


Figure 12 –Stretchable patterns: (a) – Meander patterns on stretchable device [66, 73]; (b) – Out-of-plane deformation due to a pre-strain in elastic membrane causing a wavy surface deformation [74]; (c) – Mesh pattern composed by several micro beams that twist buckle out-of-plane when deformed [67].

A manufacturing process inspired in Kirigami patterns was presented in 2015 by Firouzeh, A. and Paik, J. [67]. The authors propose a stretching sensing method based on the resistance change of a metal film under strain, a similar concept as the working principle of a strain-gauge. The device consists of a thin Constantan film laminated on a polyimide sheet composed by two patterns: a mesh pattern consisting of a linear array of slits, to make the device stretchable, and a metal serpentine path pattern layer acting as a resistance that changes when deformed like a strain-gauge. The most important advantage presented by the authors is the possibility of using the presented Kirigami approach to produce devices that act as a sensing element capable of measuring displacement as it occurs. The modified metal tracks profile leads the metal layer to be partly in tension and partly in compression in different sections of the device when stretched, as shown in Figure 13, resulting in a sensitive to strain device (since the effect of the parts in tension and compression does not cancel each other out).

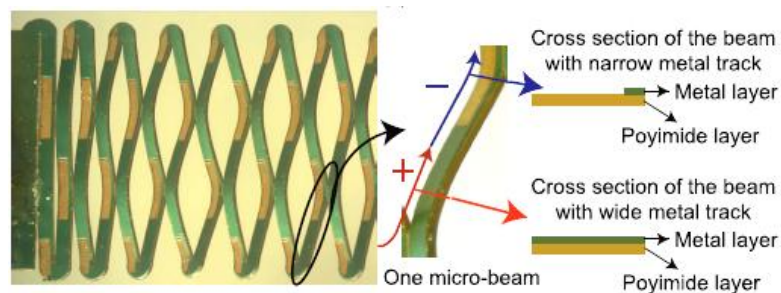


Figure 13 – Stretched kirigami sensor [67]. As the sensor is stretched the micro-beams twist and bend out of plane leading to positive and negative strains in different sections of the metal layer. The tension is represented by the plus sign, while the compression is represented by the minus sign.

More recently, in 2017, Wang, Z. *et al.*[71] presented a kirigami-patterned stretchable device composed by carbon nanotubes conductive networks embed on a PDMS substrate. The manufacturing process consists of three main steps, as depicted in Figure 14: Manufacturing of uniform CNT (carbon nanotubes) films by dispersing aqueous CNT in hydrophilic glass substrate, resulting in the formation of a thin CNT film after drying. Subsequently, the CNTs are integrated with PDMS by spin coating a mixture of PDMS with a curing agent. Once cured, the sample can be peeled from the glass substrate and hence a thin CNT/PDMS composite film is obtained. Finally, laser ablation is used to cut the thin film, resulting in a Kirigami pattern composed by linear cuts.

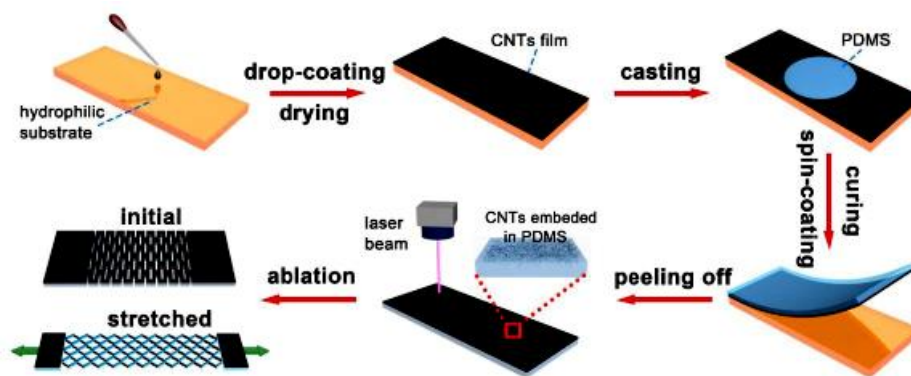


Figure 14 – Manufacturing process of a kirigami-patterned stretchable device composed by CNTs embed inside a PDMS layer [71].

Such devices have proven to be highly stretchable with an elongation as high as 430% and stable conductivity under strain levels up to 380%. The stretchable devices also possess excellent reversibility holding 500 repeated cycles with strains ranging from 0 to 400% with neglectful hysteresis and unchanged conductivity.

In the same year, 2017, Baldwin, A and Meng, E. [69] presented a Kirigami device manufactured using clean room techniques that allow achieving higher control on the designed features, Figure 15. The manufacturing process consists on initially coating a Parylene C layer and deposit a thin gold film, which is subsequently patterned using lift-off and Deep Reactive Ion Etching (DRIE) to etch slits in a free-standing Parylene substrate. The Parylene C layer acts both as support and insulation layer and presents a capability of standing 200% elongation before breaking.

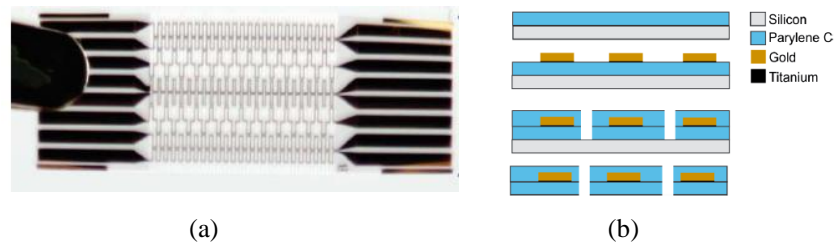


Figure 15 – Manufacturing process of a kirigami-patterned stretchable device, (a), using clean room techniques, (b) [71].

However, as it was previously seen, achieving a higher performance using Kirigami patterns comes with a cost: the manufacturing process is more complex and time-consuming, which is one of the biggest challenges for practical use.

2.6 Summary of the presented studies

The presented studies provided insight on under-actuated systems applied to robotic hands and grippers, demonstrating their advantages compared to fully-actuated systems. The interest on grippers as a grasping solution instead of robotic hands to emulate the dexterity of human hands has grown over the last years since the complexity on the manufacturing process and the computational time and power to operate grippers are lower.

The evolution of grippers has begun as simple grippers with simple actuation mechanism where self-adaptability was the primordial aspect and main advantage of such devices. Their redundant number of DoFs provided inherent softness to grasp an object by enveloping it in between the robotic fingers. However, the simpler design came with the cost of limited configurations and unstable grasps for certain lighter and delicate objects where a pinch grasp was more suitable. As a solution to that problem, compliance mechanisms to adjust the stiffness of the joints that compose the fingers structure were proposed. Modulating the stiffness of the joints allowed increasing the compliance of the finger and achieve different grasp configurations. As a result, the input actuation torque was distributed to proper joints and directions leading to an increased safety interaction between the gripper and the surrounding environment. More recently, tactile sensing systems started to be integrated on the fingers structure to provide feedback to identify the object's shape, understand the force interaction between the fingers and the objects and even detected slip events to automatically adjust the grasp configuration and applied torque [52, 54]. Table IV presents a summary of the studies providing insight on the challenges of under-actuated robotic grippers, the literature approach to solve those challenges, and the approaches being implemented on this thesis to solve the problems according to what was still missing on the presented literature.

TABLE IV – Challenges and approaches to solve them according to literature review and what is still to be done.

Challenges	Literature approach	What still misses	My approach
Design of simple architectures with simple actuation mechanisms to grasp objects.	Simple under-actuated grippers with self-conformity to objects [7, 8, 43, 44].	Fast and low cost manufacturing process.	Robogami platform using unique layer-by-layer manufacturing process and precise fabrication methods using UV laser
Find a compromise between input actuation torque and output force.	Adjust the compliance by substituting classical revolute joints with adjustable stiffness materials, like springs [9]–[12], elastic materials like PTFE [13] or thermally responsive layers, [6, 14, 16, 45, 46, 47].	A easily replaceable and scalable robust stiffness layer that allows achieving different grasp configurations.	Manufacturing process of individual adjustable stiffness layers (ASLs) using the robogami platform to improve robustness. These ASLs act as a locking joint mechanism allowing different configurations being performed
Understand the interaction forces between objects and grippers.	Integration of tactile sensing systems to either obtain information about the shape of the object [21] or force distribution [18, 22].	Studying how to improve grasping quality by adjust the configuration of the gripper.	Integrate tactile sensors to study effective grasp configurations to ultimately define a control strategy capable of adjusting the grasp configuration of the gripper and obtain securer grasps.

CHAPTER 3

UNDER-ACTUATED GRIPPER WITH ADJUSTABLE STIFFNESS

JOINTS

As robots move from confined workspaces to unstructured environments, they should be able to adapt to those environments. In particular, for robotic hands and manipulators, robots need to be able to manipulate objects with different shapes and sizes, with precision movements and grasping security, which require highly dexterous robots with multiple degrees of freedom and different assigned configurations. However, high dexterous robotic grippers with independent actuation of each joint result in complex actuating systems, which increase the overall weight of the gripper and require more computational load and so computational time [1, 4]. Thus, the need for simpler and lighter robotic systems led to an alternate approach consisting of under-actuated mechanisms to actuate many DoFs with a single actuation source, while an adjustable stiffness layer allows distributing the input actuation force to properly apply to objects being grasped.

This chapter aims to present the manufacturing process of a tendon-driven robogami under-actuated gripper with adjustable stiffness joints that uses a fast and low-cost manufacturing process to reduce the overall cost production.

3.1 Manufacturing process

Robotic origamis, robogamis, are planar and foldable robotic platforms that use fast and precise fabrication methods using a UV laser to micro machine quasi 2-D layers [4]. The unique layer-by-layer manufacturing process, which consists of several alternating cutting and heat pressing steps, allows integrating multiple functional layers. As a result, the fingers can be easily customized and scaled to fit into confined spaces or to perform heavier tasks where robustness is desirable. Moreover, the fast and low-cost manufacturing process allows reducing the overall cost production of the gripper, as desired.

The initial conditions for the manufactured finger are as follows:

- 1) Two fingers must be produced to compose the gripper, each composed by five joints.

In each finger the base joint must move in the opposite direction of the remaining ones due to compliance and grasping features that will be explained further on section 5.5.1.

- 2) The angle of the joints must have an upper limit of approximately 45° on the moving direction and a lower limit of 1° on the opposite direction.
- 3) An actuation mechanism must be integrated in order to actuate all joints. The actuation source must be simple and compatible with the robogami manufacturing process.
- 4) A sensing support must be developed to integrate tactile sensors.
- 5) An adjustable stiffness layer must be manufactured to adjust the stiffness of the joints and thus enable different configurations to be performed.

3.1.1 Robogami finger manufacturing process

In order to fabricate the finger structure, the following materials, represented in Figure 16 – (a), were used:

- 1) Cured glass fiber (CFK-Prepreg-Platte 200 x 200 x 0.6mm), as a structural material for the fingers making them more robust.
- 2) DuPont™ Pyralux adhesive LF0111 2mil thick, represented by the yellow polyimide sheet. The LF0111 layers are thermoset adhesive layers used to bond different glass fiber layers. Thus, between each glass fiber layer there will be an adhesive layer to bond them together.
- 3) DuPont™ Polyimide Kapton 5 mil thick. This material will define the hinge layer of the robogami finger.

The layer-by-layer manufacturing process consists of initially micromachining the different designed layers using a UV Laser.

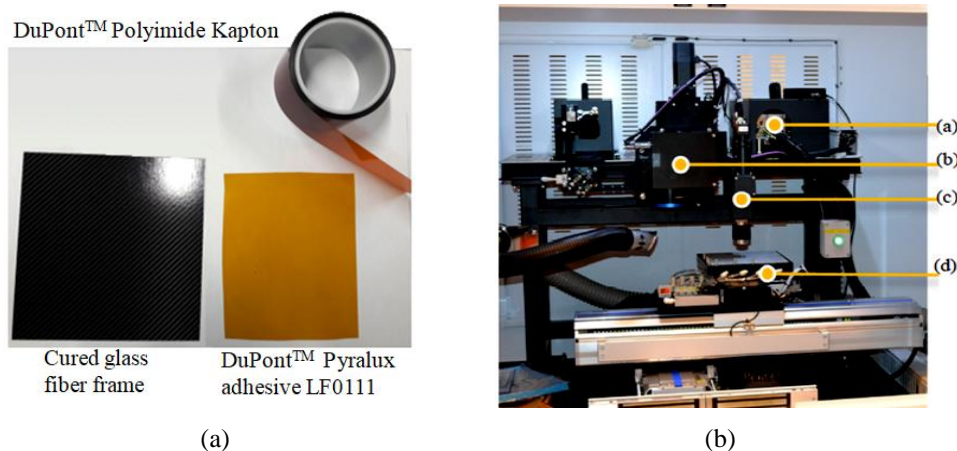


Figure 16 – Materials (a) and Laser micromachine (b) used in the manufacturing process of the robogami finger structure. In (b), (a) represents the laser head, (b) the scanner, (c) the camera and (d) the moving stage.

The micromachining device (LAB 3350 developed in collaboration with Inno6 Inc.), depicted in Figure 16 – (b), enables cutting different patterns on different materials. A DCH-335-4 laser head (Photonics Industris Inc.) is responsible for cutting the layers by adjusting its power range from 0 to 4.7W. A scanner (HurryScanIII10 from ScanLab) is used to make the cuts with a top speed of 2.5 m/s within a 50 x 50 mm field with 5 μ m accuracy. On the other hand, a linear stage (LP 200-St-200L from LPK) with the same accuracy as the scanner is used for cutting larger patterns (up to 200 x 200 mm). Thus, combining both machining systems allows transferring the designed pattern to the different materials that will compose the finger with high accuracy and speed. Finally, two different cameras with magnification of 3.2 and 10 are used to align parts where multiple steps are required [75].

Once all the individual glass fiber and polyimide layers are cut, the finger can be assembled by heat pressing (Carver, Inc. Bench Top Heat Press) the different layers. The layer-by-layer manufacturing process consists now in alternating glass fiber and polyimide layers, which are aligned and assembled on top of a jig, Figure 17 – (a). A special Teflon Film sheet is used to cover the bottom and top layers to ensure that bonded layers do not melt on the jig surface.

The heat pressing process must have into account the adhesive properties of the polyimide sheet to ensure a strong bonding between different layers. According to the datasheet of the materials and their properties [76, 77] the heating temperature, pressure and time that ensures a high quality bonding must be 182-199 $^{\circ}$ C, 200-400 psi, 1-2h at temperature, respectively. So, the layers are heated at a 200 $^{\circ}$ C temperature with 150 psi pressure during 1h. After all the layers are bonded and the structure has cooled down at room temperature (about 25 $^{\circ}$ C), the outer structure used for aligning the layers during the bonding process is cut to release the joints that allow the finger motion, as shown in Figure 17 – (b).

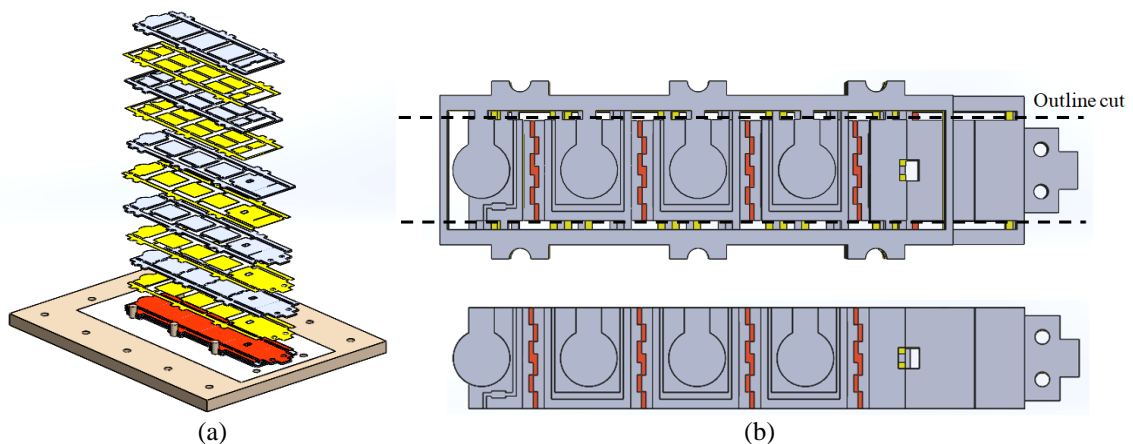


Figure 17 – Initially the layers are aligned, stacked on a jig and then heat pressed (a) resulting on the finger structure presented in (b). Then the outer frame used to align the layers is cut using a UV Laser. As a result, the joints are released.

3.1.2 Robogami finger structure

At this point, **requirements 1 to 4 have been achieved**, integrating multiple layers to finalize the finger structure. Thus, each finger is composed by the following layers, as illustrated in Figure 18.

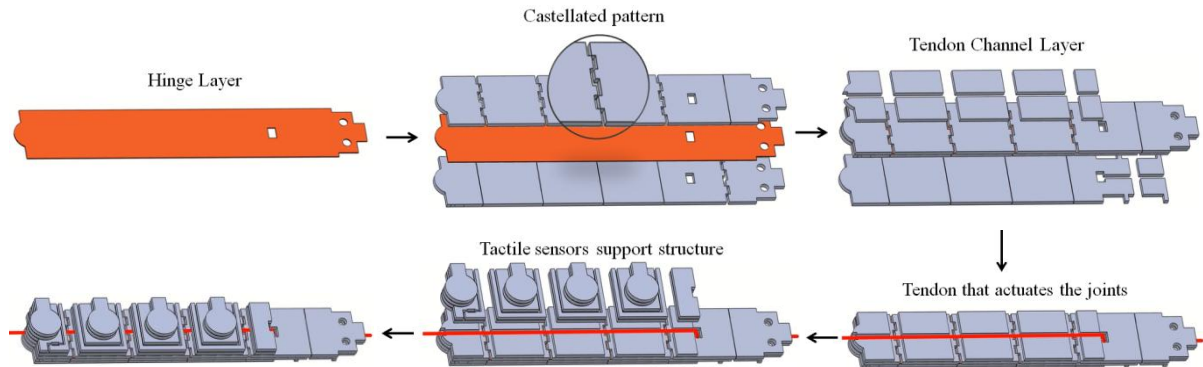


Figure 18 – Manufacturing process of the tendon-driven robogami under-actuated gripper with adjustable stiffness joints.

The **hinge area layer** is composed by a single polyimide layer that defines the DoFs of the finger and is responsible for the joint coupling that connects all joints. A rigid layer of glass fiber with a **castellated pattern** fixes the axis of rotation and increases lateral stability of each joint. This structure allows defining the range of motion of the joints without the need of adding mechanical parts, such as gears, allowing minimizing the space and overall weight of the finger. The number of joints is defined by the number of castellated patterns on the glass fiber layers, meaning that five of the mentioned structures must be designed in order to achieve the five joints initially required. The range of motion of the joints is limited by the gap between the castellated pattern of two consecutive tiles and the height of the teeth to the polyimide hinge layer that acts as the neutral plane for the bending motion, as shown in Figure 19.

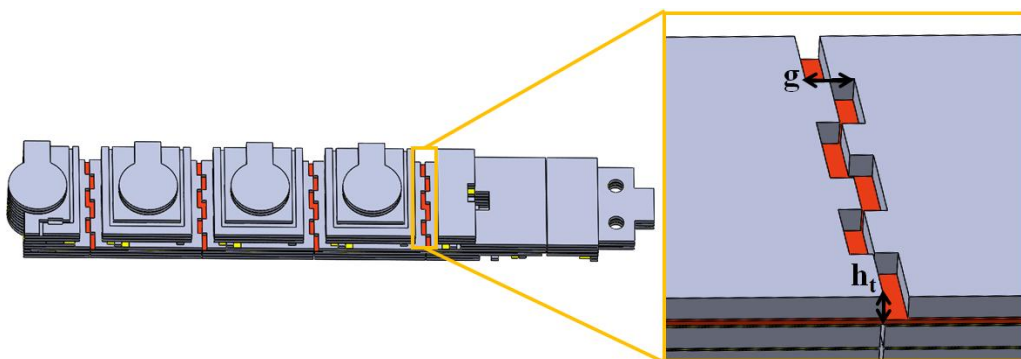


Figure 19 – Final structure of the finger. Zoomed in the right side of the figure is the castellated pattern indicating the gap and the height of the teeth that allows adjusting the range motion of the joints.

Thus, the gap should not only be small enough to keep the rotational axis fixed and on the hinge layer, but also large enough to ensure the mechanical endurance of the polyimide layer over repeated cycles. More importantly, by modulating the length of the gap, g , and the height of the teeth, h_t , one can set a joint limit, θ_{limit} , according to equation (1).

$$\theta_{limit} = \sin^{-1}\left(\frac{g}{2h_t}\right) = \sin^{-1}\left(\frac{1.24\text{mm}}{2 \times (0.6\text{mm} + 0.0508\text{mm})}\right) = 46.69^\circ \quad (1)$$

, which is approximately the required value initially imposed.

The **tendon channel layer** is designed to direct the tendon from one side of the finger to the other and should pass through all joints, as depicted in Figure 18. Also, depending on the location of the tendon channel (above or below the neutral plane) the finger folds in a certain direction. Thus, if one joint needs to move in the opposite direction of the remaining ones, its tendon channel and castellated pattern needs to be in the opposite side of the hinge layer as the others. For this reason, **the tendon switches side between the first and second joint and consequently the first joint of finger is actuated in opposite direction**. Finally a column-shaped structure is integrated on the tiles of the finger acting as a support for the tactile sensors that will be integrated.

At this point, the under-actuated tendon-driven robogami gripper has all joints being actuated when the tendon is pulled. As a result, the input actuation torque is distributed to all the joints. However, a compromise between the torque input and the output force applied to the objects must be found since heavier objects require higher contact forces while smaller and fragile objects require more delicate handling. For such reason an **adjustable stiffness layer (ASL)** needs to be manufactured and integrated in the above finger structure, **meeting the 5th requirement**. The ASL is responsible for adjusting the compliance of the fingers and allows achieving different configurations to grasp different objects.

3.1.3 Adjustable stiffness layer (ASL) manufacturing process

As mentioned in the previous section, the locking mechanism and compliance of the joints can be achieved by adjusting their stiffness. Among the examples presented in the literature, only the ones using thermoplastic polymers are compatible with the unique layer-by-layer manufacturing process that is used to manufacture the tendon-driven robogami finger. Thus, the use of thermoplastic polymers is an optimal choice given the significant change in their modulus of elasticity, low price and ease of processing.

In particular, Shape Memory Polymers (SMPs) offer the advantage of possessing a high shape recovery rate and stiffness modulation, which makes them desirable among other thermoplastic options. The stiffness control is achieved by varying their elasticity modulus (SMP MM5520 from SMP Technologies)[78], which varies within a range from 2.1 GPa at room temperature to 2.1 MPa at temperatures higher than its glass transition temperature (55 °C) [3], as can be seen in Figure 20.

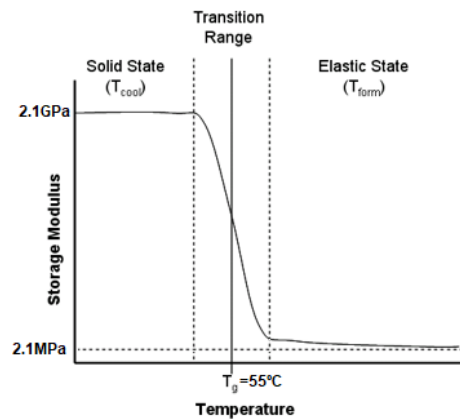


Figure 20 – The modulus of elasticity of the SMP changes orders of magnitude over the glass transition temperature ($T_g=55^\circ\text{C}$)[78].

To control the temperature of the SMP, a stretchable heater is embedded between two layers of SMP sheets, as shown in Figure 21 – (d). The heater thermally activates the SMP, which consequently changes its stiffness. Initially, SMP pellets, Figure 21 – (a), are transformed into sheets by heat pressing the pellets at 160 °C at a pressure 3000 psi and using spacers (Figures 21 – (b) and (d)) to achieve the desired thickness of $\approx 225\mu\text{m}$. The shape memory effect of the SMP layer is important since in the absence of external actuation forces, this layer is responsible for driving the ASL to its initial pre set position.

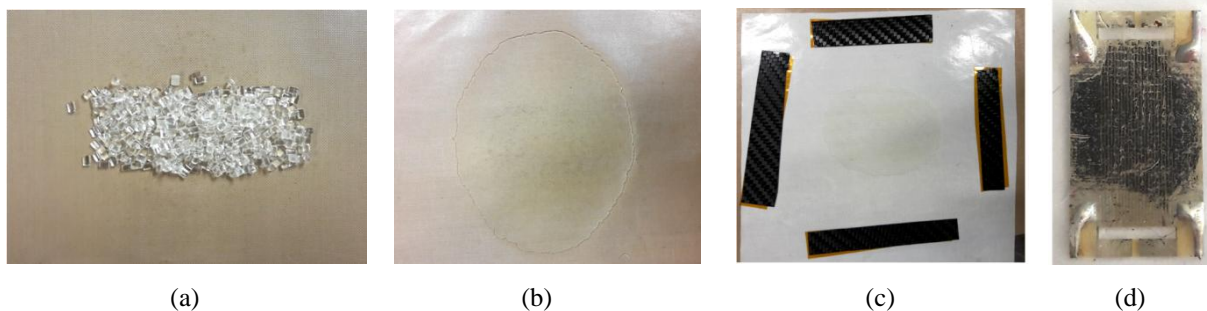


Figure 21 – Embedding process of the stretchable heater inside the SMP Layer: (a) SMP pellets are transformed into SMP sheets, (b). The stretchable heaters is then embedded in between the two SMP sheets using spacers, (c), resulting in the final structure, (d).

To improve the SMP shape recovery a silicone rubber encapsulation is performed. To do it so, the SMP layer with the embedded heater is initially laser cut to transfer the final design to

the assembled layers, as illustrated in Figure 22 – (a). Notice that the outer frame of the heater designed to prevent its elongation and consequent irreversible damage during the embedding process between the SMP layers is cut, making the heater now stretchable only if it is thermally activating the SMP and hence modulating its stiffness. In addition, some holes are cut through the layers, as it is also shown in Figure 22 – (a), to create points that allow increasing the mechanical bonding between the silicone rubber and the remaining structure of the ASL. Furthermore, a glass fiber frame is attached to the cut layers, as presented in Figure 22 – (b), to serve both as a mold for the silicone rubber and as an anchoring point to connect the ASL to the robogami structure [3, 67].

The silicone encapsulation is performed by mixing two parts of Dragon skin-10 from Smooth-on, that react one each other hardening the silicone from its fluid state to its rubber state. Initially, both parts are added to a cup with a 1:1 ratio. Then, a mixer is set to a rotation speed of 2000rpm, which mixes both parts during 1min30s. The silicone is then poured into a Petri dish and degassed inside a vacuum chamber to prevent air bubbles during the encapsulation process. Once degassed, the SMP layer with the heater and glass fiber frame are placed on top of the silicone, while weights are added to sink the layers on the silicone that fills all the existent space inside the structure. Next, the silicone is cured on a hotplate in two different temperature phases, initially at 100°C until the silicone starts to enter the rubber state and then at 140°C to complete the process, avoiding bonding the weights used to sink the structure. The result of the silicone rubber encapsulation is illustrated in Figure 22 – (c). Finally, the outer frame of the ASL is cut on the laser to release it, Figure 22 – (d), becoming a stretchable device when the heater thermally activates de SMP layer, as shown in Figure 22 – (e).

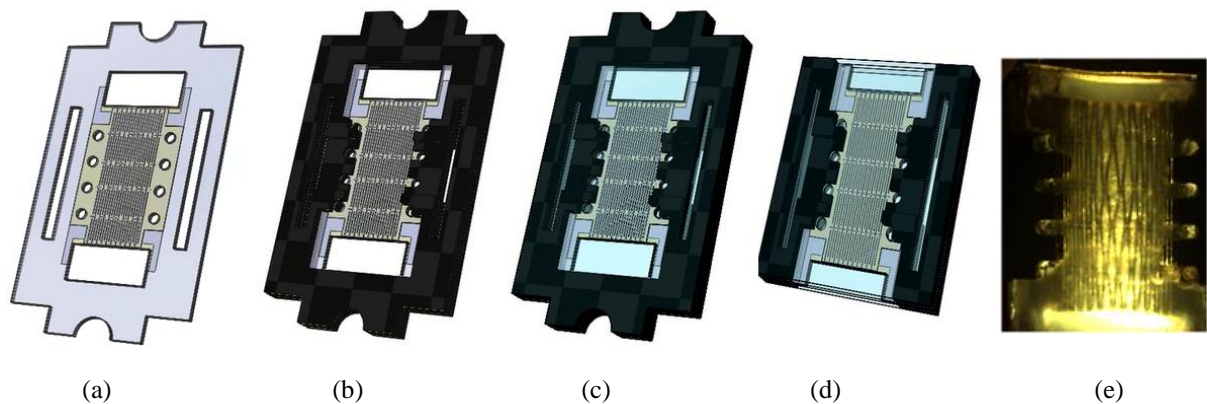


Figure 22 – ASL manufacturing process: A stretchable heater is embedded between two SMP sheets (a). A glass fiber frame is bonded to the SMP layer and the heater (b). The silicone rubber is poured into the structure filling the empty spaces (c). Finally, the aligning outer frame is cut, releasing the heater, (d) and making the device stretchable (e).

3.2 Mathematical model

The following section aims to present the mathematical model for the tendon-driven under-actuated robogami finger previously manufactured. The model hereby presented is an adaptation of the model presented by Birglen, L. *et al.* [5] and Firouzeh, A *et al.* [2]. The following assumptions are made in order to validate the model:

- 1) – The finger is planar (no abduction/adduction motion);
- 2) – All phalanges are coupled through the hinge layer;
- 3) – Only one actuator is used to drive all the phalanges of the finger;
- 4) – The contact forces are normal to the tiles of the fingers and occur at the middle of the tile.

According to Birglen, L. *et al.*, “a grasp is stable if and only if the finger is in static equilibrium” [5]. Thus, the input virtual power of the system should be equal to the sum of the required work for changing the configuration of the robogami finger, W_{ASL} , and the work to move each phalanx against the contact forces, $W_{contact}$, as described in equation (2).

$$\mathbf{F}_t^T \dot{\mathbf{X}} = W_{contact} + W_{ASL} \quad (2)$$

In equation (2) the left side represents the input work, where the elements of F_t are the tendon tension at each joint. The elements of tendon tension matrix are calculated by subtracting the friction forces, F_{fi} , to the input tension, F_{ti} , from the base to the tip joint [4], as shown in equation (3).

$$\mathbf{F}_t^T = [F_{t_0} - F_{f_1} \quad F_{t_0} - F_{f_2} - 2F_{f_1} \quad F_{t_0} - F_{f_3} - 2\sum_{i=1}^2 F_{f_i} \quad \dots] \quad (3)$$

However, since the tendon friction is difficult to be modeled, its terms are neglected and the tendon tension is considered constant and equal to F_{t_0} for all joints.

The input work presented in equation (2) also depends on the elements of $\dot{\mathbf{X}}$, which represents the rate of the tendon displacement caused by the motion of each joint. The relationship between these two parameters is accomplished by introducing a matrix \mathbf{T} that depends on the transmission mechanism used to propagate the actuation torque to the phalanges [5, 26]. As a result, \mathbf{T} is responsible for relating the vector of the angular velocities to the time derivatives of the phalanx joint coordinates, $\dot{\boldsymbol{\theta}}$, as presented in equation (4).

$$\dot{\mathbf{X}} = \mathbf{T}\dot{\boldsymbol{\theta}} = \begin{bmatrix} \frac{\partial X_1}{\partial \theta_1} & 0 & \dots & 0 \\ 0 & \frac{\partial X_2}{\partial \theta_2} & \dots & 0 \\ \vdots & \vdots & \vdots & \vdots \\ 0 & 0 & \dots & \frac{\partial X_n}{\partial \theta_n} \end{bmatrix} \dot{\boldsymbol{\theta}} \quad (4)$$

, where $\frac{\partial X_i}{\partial \theta_i}$ is the transmission ratio between the input and the i^{th} joint.

Since the displacement of the tendon causes the joints to move, the correlation between the tendon displacement and the bending angle at each joint governs the transmission ratio between the tendon force and the torque applied to the respective joint, as represented in Figure 23.

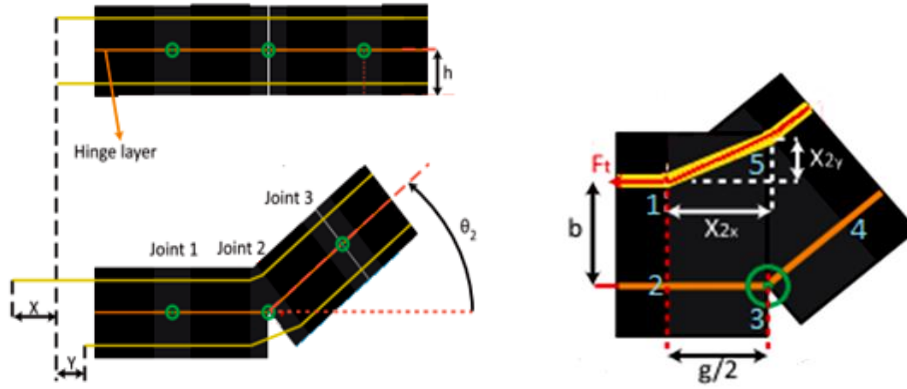


Figure 23 –Schematic of the finger designed and the actuation of the second joint from a cross section side of view. The schematic of the finger with its second joint at an angle θ_2 is presented to illustrate the displacement of the tendon. The point of interaction between the tendon and the glass fiber layer is magnified to show the tendon displacement and the path used to calculate (7) and (8).

From the figure above the contribution of the tendon displacement to the bending motion of each joint is given according to equation (5).

$$X_i = g - \sqrt{X_{ix}^2 + X_{iy}^2} \quad (5)$$

, where g is the gap between two consecutive tiles, X_i is the tendon displacement through the i^{th} joint and X_{ix} and X_{iy} the components in each direction, given by equations (6) and (7).

$$X_{ix} = \frac{g}{2}(1 + \cos(\theta_i)) - b \sin(\theta_i) \quad (6)$$

$$X_{iy} = \frac{g}{2}(\sin(\theta_i)) + b(\cos(\theta_i) - 1) \quad (7)$$

, where θ_i is the i^{th} joint angle.

Thus, the transmission ratio, $dX_i/d\theta_i$, that relates the rate of the tendon displacement, dX_i , with the angular velocities of the joints, $d\theta_i$, can be calculated as presented in equation (8). The demonstration can be found in Appendix I.

$$dX_i = \frac{X_{ix}b + X_{iy}(g/2)}{\sqrt{X_{ix}^2 + X_{iy}^2}} d\theta_i \quad (8)$$

Is important to refer that the displacement, X_i , from equation (5), corresponds to the effective displacement that results in the configuration change of the under-actuated finger. However, the input displacement is the sum of effective displacement X_i and the tendon elongation due to the tensile load, as presented in equation (9).

$$X_{\text{total}} = \sum_{j=1}^n X_i + \sum_{j=1}^n \frac{F_t - \sum_{j=2}^{i-1} 2F_{fj}}{k_{t_i}} \quad (9)$$

, where F_t is the tendon tension, F_{fj} are the friction forces of the tendon at each joint and k_{t_i} is the stiffness of each section of the tendon between joints $i-1$ and i . However, since the friction is not being modelled and the stiffness of the tendon is higher than the tendon tension, equation (9) can be reduced to equation (10).

$$X_{\text{total}} = \sum_{j=1}^n X_i \quad (10)$$

For the right side in equation (2), the first term, W_{contact} , corresponds to the work done by the contact forces. It is known that in general, work is the result of a force, F , applied to a point that moves through a displacement, \dot{X} , as presented in equation (11).

$$W = F\dot{X} \quad (11)$$

Furthermore, it is also known that the Jacobian matrix J relates the Cartesian velocities, \dot{X} , with joints velocities, $\dot{\theta}$, [79], as described in equation (12).

$$\dot{X} = J\dot{\theta} \quad (12)$$

Combining equations (11) and (12), one obtains the equation for the work done by the contact forces, as described by equation (13).

$$W_{\text{contact}} = \mathbf{f}^T J\dot{\theta} \quad (13)$$

, where \mathbf{f} is the vector for the contact forces.

The Jacobian matrix, \mathbf{J} , depends on the location of the contact points and the relative orientation of the phalanges [5]. Since the contact forces are being applied at each joint normal to the phalanges, as shown in Figure 24, and the contact point is assumed to happen at the middle of the tiles, where the tactile sensors will be placed, the Jacobian matrix is calculated as shown in equation (14).

$$\mathbf{J} = \begin{bmatrix} k_1 & 0 & \dots & 0 \\ r_{12}^T x_2 & k_2 & \dots & 0 \\ \vdots & \vdots & \vdots & \vdots \\ r_{1n}^T x_n & r_{2n}^T x_n & \dots & k_n \end{bmatrix} \quad (14)$$

, where r_{ki} is the vector from the origin joint point O_k and x_i is the length of the link. In equation (14) it was used that $r_{ii}^T x_i = k_i = l_i/2$ is the distance between the i^{th} joint and the i^{th} contact point, which is equal to half the phalanx length, as initially assumed. The remaining components of the Jacobian matrix can be expressed as

$$r_{ij}^T x_j = k_j + \sum_{k=1}^{j-1} l_k \cos(\sum_{m=k+1}^j \theta_m) \quad (15)$$

, where l_k is the length of the link and θ_m the joint angle. At this point, equation (2) can be rewritten as equation (16).

$$\mathbf{F}_t^T \dot{\mathbf{X}} = W_{\text{contact}} + W_{\text{ASL}} \Leftrightarrow \mathbf{F}_t^T \begin{bmatrix} \frac{\partial X_1}{\partial \theta_1} & 0 & \dots & 0 \\ 0 & \frac{\partial X_2}{\partial \theta_2} & \dots & 0 \\ \vdots & \vdots & \vdots & \vdots \\ 0 & 0 & \dots & \frac{\partial X_n}{\partial \theta_n} \end{bmatrix} = \mathbf{f}^T \mathbf{J} + W_{\text{ASL}} \quad (16)$$

For the required work for changing the configuration of the finger, W_{ASL} , one has to keep in mind that the ASLs behave as springs. Therefore, when the tendon is released, the elastic force applied by the ASLs returns the joints to their pre set position and the finger to a straight configuration [4]. Thus, the work done by the ASLs can be expressed by equation (17).

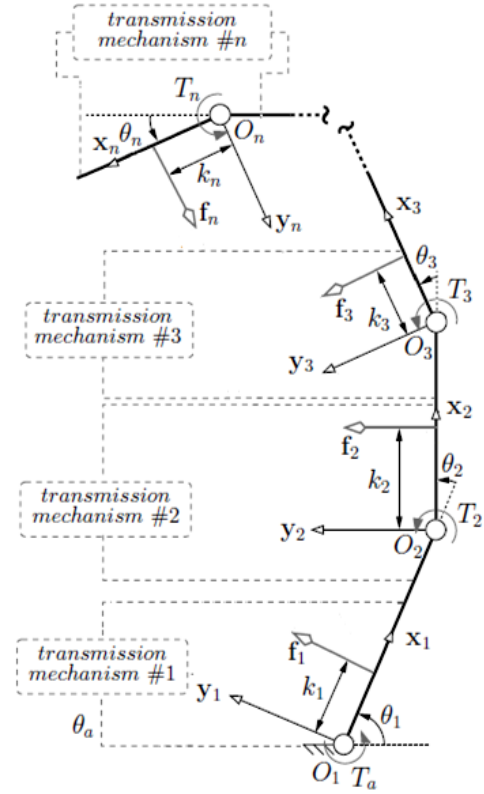


Figure 24 – Conceptual under-actuated finger.

$$W_{ASL} = \mathbf{F}_{ASL}^T \dot{\Delta} = \left(\begin{bmatrix} K_{ASL1} & 0 & \cdots & 0 \\ 0 & K_{ASL2} & \cdots & 0 \\ \vdots & \vdots & \ddots & \vdots \\ 0 & 0 & \cdots & K_{ASLn} \end{bmatrix} \Delta \right)^T \dot{\Delta} = (\mathbf{K}_{ASL} \Delta)^T \dot{\Delta} \quad (17)$$

, where Δ and \mathbf{F}_{ASL} represent the elongation and the force done by the ASLs, respectively. The elements of, \mathbf{K}_{ASLi} , represent the stiffness of the ASL of the corresponding i^{th} joint. The ASL elongation is calculated according to equation (18) and its derivation can be found in Appendix II.

$$\Delta = 2 \left(h + \frac{t_{ASL}}{2} \right) \sin \frac{\theta}{2} \quad (18)$$

, where h is the distance from the neutral plane of the finger (hinge layer) to the ASL attached to it and t_{ASL} is the ASL thickness. Replacing the energy storage rate of the ASLs in equation (2) as demonstrated in Appendix III, yields the following equation which correlates the tendon tension, $\mathbf{F}_t^T \mathbf{T}$, with the angle of the joints, θ , and the ASL stiffness, \mathbf{K}_{ASL} , obtaining,

$$\mathbf{F}_t^T \mathbf{T} = \mathbf{f}^T \mathbf{J} + \left(h + \frac{t_{ASL}}{2} \right)^2 ((\mathbf{K}_{ASL} \sin(\theta)))^T \quad (19)$$

Concluding, equations (10) and (19) fully describe the model of the fingers, allowing to study the effect of the joint stiffness on the reconfiguration of the finger.

CHAPTER 4

STRETCHABLE HEATER

Stretchable sensors possess the advantage of allowing high reversible deformability [68]. Moreover, despite elastic electronic materials display stable and reliable electrical properties upon repeated and multi-axial deformations [68], it is also desirable to produce stretchable devices and circuits out of fragile materials. Thus, given the **limited elastic strain in metals, a pattern that transforms a small strain in the metallic layer into a large displacement**, making it stretchable, needs to be designed. The challenge is to minimize the local stress induced by the deformation alongside with the capability of maintaining a stable electrical connection when deformed. As reviewed before, the patterning of strain-relief motifs in the form of serpentines allows to minimize the local stresses induced by mechanical deformations. Thus, the use of offset rows of slits, inspired in Kirigami patterns, enables stretching a material beyond what its normal tensile properties would allow, as presented in [68, 69, 80, 81].

In this section the manufacturing process and characterization of the stretchable heater is presented. The manufacturing process was developed using clean room techniques, making it compatible with the robogami platform since it can be integrated on the layer-by-layer manufacturing process. Moreover, such manufacturing process allows producing more than one heater on a single batch, resulting in a decreased variability of their characteristics. Finally, the possibility of using the stretchable heaters as temperature sensors is studied, since it allows saving space and avoids extra sensors that would have to be incorporated in order to determine the ASL stiffness.

4.1 Stretchable heater design

In this section the design of the stretchable heater is presented. The requirements for the design are the following ones:

- 1) The dimensions of the heater should fit on the finger structure to be embedded inside the SMP layers.
- 2) The heater should be a stretchable structure to allow its integration and continuous operation when the joints are actuated and consequently bent.
- 3) They should operate at 1W of power consumption when a 6V power supply is used.

The design of the heater was initially developed using a CAD software to dimension the device as desired (8.1mm x 14.4 mm) and superimpose the different layers that compose the device structure, as shown in Figure 25. The stretchable heater is composed by five different serpentine paths and a mesh pattern of offset slits that provide the necessary stretchability to the device. Thus, both **first and second requirements are accomplished**.

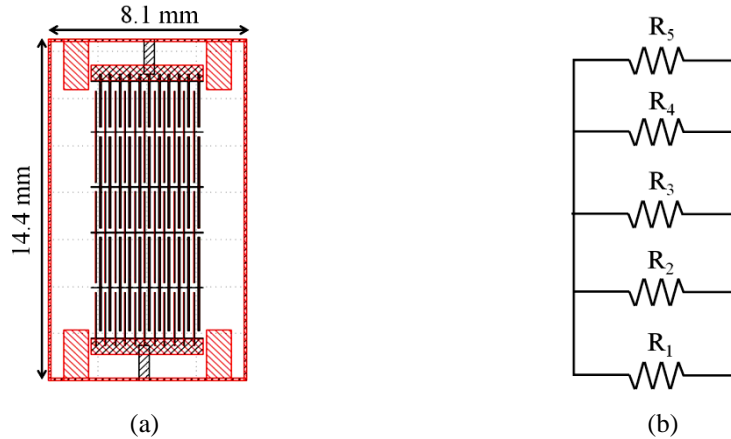


Figure 25 – Layout of the proposed design for the device, (a). The structure is composed by 5 serpentine paths and 4 contact pads. Besides these features, it is possible to observe two T-shapes in upper and lower middle of the design. Their function is to ensure the electrical insulation between the two pairs of contact pads, so that the resistance can be measured using those contact pads (upper pair and lower pair). (b) Equivalent circuit for the 5 serpentine paths.

To meet the **third requirement**, a simple calculation described by equation (20), allows obtaining the expected resistance for the device to be manufactured.

$$R = \frac{V^2}{P} = 36\Omega \quad (20)$$

, where R is the resistance of the stretchable heater, P is the power consumption and V the voltage across the heater.

As it is possible to observe in Figure 25 – (b) the equivalent circuit of the structure geometry consists of five parallel resistances, meaning that the individual resistance value of each serpentine path should be 5 times higher than the overall resistance value for the device. Therefore, each serpentine path should present a resistance value of 180Ω . It is important to refer that this approximation is only valid if the geometry of all serpentine paths are equal, leading therefore to an ideal voltage divider with five resistances of equal value.

From the geometry of the serpentine path, presented in Figure 26, it is possible to calculate each serpentine resistance value and hence the value for the equivalent resistance of the heater. The dimensions of the device are presented on Table V for each serpentine path.

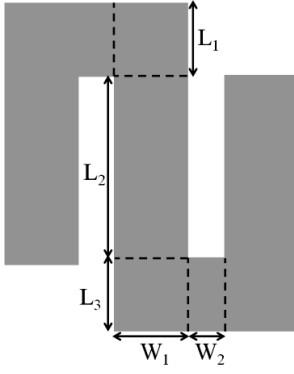


Figure 26 – Each serpentine path is composed by 23 micro beams with the dimensions shown in Table V.

TABLE V – Micro beams dimensions for each of the serpentine paths.
The resistance of each serpentine path is given by equation (21).

	R ₁	R ₂	R ₃	R ₄	R ₅
L ₁ (mm)	0.394	0.183	0.183	0.184	0.183
L ₂ (mm)	1.548	1.943	1.548	1.943	1.627
L ₃ (mm)	0.183	0.183	0.182	0.183	0.315
W ₁ (mm)	0.160	0.160	0.160	0.160	0.160
W ₂ (mm)	0.040	0.040	0.040	0.040	0.040

To calculate the resistance of the serpentine path, the accumulation of particles in the corners of the serpentine path has to be taken into account, since they contribute differently to the resistance value than the beams structure. A good approximation is to consider that the sheet resistance in the corners contributes only 56% to the resistance value [82, 83]. Therefore, since each serpentine is composed by $N=23$ beams, the resistance for each serpentine is generally given by equation (21).

$$R_i(\Omega) = \frac{\rho}{t} \left[\frac{N}{W_1} (0.56(L_1 + L_3) + L_2) + \frac{N-1}{2W_2} (L_1 + L_3) \right] \quad (21)$$

, where ρ is the electrical resistivity of the metallic layer that composes the serpentine path and $t=250\text{nm}$ is its thickness.

Calculating each resistance based on the values of Table V and equation (21), the following table is obtained with the resistance value for each serpentine that compose the structure of the heater.

TABLE VI – Resistance values for each of the serpentine paths that compose the structure of the devices.

R ₁ (Ω)	R ₂ (Ω)	R ₃ (Ω)	R ₄ (Ω)	R ₅ (Ω)
181.3	173.6	149.4	173.7	174.2

Thus the equivalent resistance can be found,

$$R_{eq} = \frac{1}{\frac{1}{R_1} + \frac{1}{R_2} + \frac{1}{R_3} + \frac{1}{R_4} + \frac{1}{R_5}} = 33.9\Omega \quad (22)$$

, which according to equation (20) leads to an input voltage value of 5.8V for the **power consumption requirements to be achieved.**

4.2 Stretchable heater manufacturing process

One of the **advantages** of the developed manufacturing process for the stretchable heater hereby presented is its **compatibility with techniques used in a clean room environment**. In the following section it will be explained the manufacturing process of the proposed device, justifying the reasons for each of the chosen processes. Further information can be found in the process outline presented in Appendix IV. The process is initiated with a 10cm silicon wafer, Figure 27 – (a).

4.2.1 Layers deposition

Initially, two metallic layers, Tungsten-Titanium (WTi) followed by an Aluminium (Al) layer, are deposited by a physical vapour deposition (sputtering) system due to the high melting temperature of the WTi (around 3422°C) and the uniformity deposition achieved, which is higher than a thermal evaporation system. Thus, an initial planar surface is obtained, which avoids variations on the thickness of the layers further manufactured. The sputtered layers will act as back electrode for releasing the final heater structure from the wafer. Therefore, the thickness of both sputtered layers does not have a specified value, as long as it allows a good electrical contact and a planar surface to start the manufacturing of the device. Thus, 100nm of WTi followed by 400nm of Al, are sputtered, as shown in Figure 27 – (b).

Once the metallic layers have been deposited, the first layer that will compose the structure of the device is coated. This layer is only structural and therefore, having into account similar processes [69], a 14µm layer of polyimide PI2611 is manually coated on top of the Al layer. On a first stage, the surface of the wafer has to be treated to improve the adhesion between layers, preventing their delamination when a strain is induced due to bending deformation. According to the information available [84] (Appendix IV – Figure 75) a dehydration surface treatment has to be performed previously to the polyimide coating. The dehydration is performed by placing the wafer on top of a hot plate at 120°C during 10min. Then, after the wafer cools down at room temperature, an adhesion promoter is applied and coated on its surface (VM651) using a wet bench coater. The wafer is then rotated at a speed of 500rpm during 10s, followed by another 30s at 3000rpm while nitrogen is introduced in the coating chamber to help spreading the adhesion promoter on the Al surface.

Once the adhesion promoter is spread across the surface, the polyimide layer is coated. A total 14µm thick polyimide layer is coated by performing two consecutive 7µm thick coating processes. The reason to divide the coating process into two is due to the high thickness that

needs to be coated. Thus, the first $7\mu\text{m}$ are coated at 1974rpm followed by a soft cure to allow the deposition of the second $7\mu\text{m}$ polyimide layer without mixing both layers completely. The soft bake process is performed by placing the wafer on top of a hotplate initially at 65°C during 3min and then at 105°C during another 3min. As it cures, the solvent on the polyimide is evaporated and the polyimide layer is compressed, which leads to an arising stress between the two polyimide layers. Thus, the soft bake with a temperature ramp decreases not only the probability of delaminating or cracking occurring as also avoids a thermal shock on this layer. Finally, the wafer is cooled down during 10s on a metallic plate at room temperature before proceeding to the second polyimide coating.

Having into account that the rotating speed of the previous polyimide coating was about 1900rpm (corresponding to $7.28\mu\text{m}$ thickness), the thickness compensation is now performed to achieve the desired final thickness. Therefore, the new polyimide coating should be $6.72\mu\text{m}$ thick. Once again, a new soft bake was performed followed by the full cure of the polyimide layer. The full cure is achieved by placing the wafer inside an oven with the capacity to heat up to 300°C [84]. The cure is performed with a temperature ramp recipe pre defined for the polyimide layer, which takes approximately 5h to reach the final temperature. At this point a planar surface of polyimide on top of the wafer is expected, as shown in Figure 27 – (c).

The next step of the process is to deposit the metallic layers that will compose the serpentine path of the heater, Titanium (Ti) and mainly Platinum (Pt). Despite the possibility of thermally evaporating both layers, since they will be deposited on top of polyimide, the use of oxygen plasma is necessary to improve the adhesion between the polyimide and the metallic layers, and so a sputtering system is used. After the Ti layer is sputtered, the layer of interest, Pt, is also sputtered. The thickness of the new layer is defined based on the calculations performed on the theoretical model presented on the section 4.1. At this point, the layers on top of the wafer should be as presented in Figure 27 – (d).

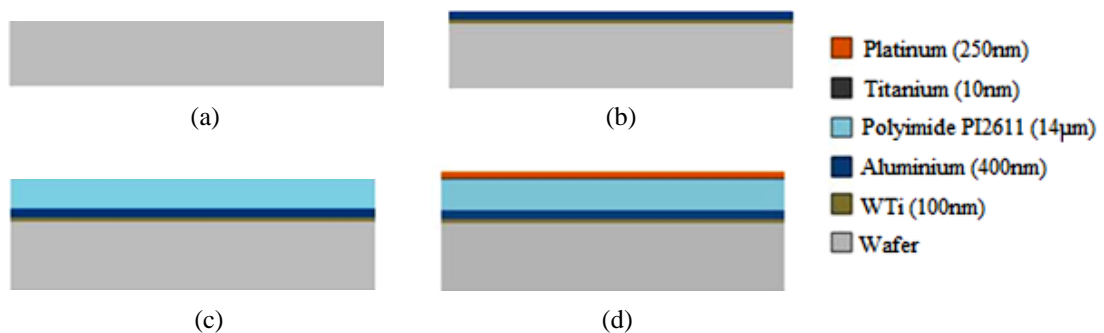


Figure 27 – Illustration of the cross section of the layers on top of the wafer. The process starts with a 10cm diameter wafer (a). Then, a WTi and Al layer are sputtered (b). Next, a polyimide coating is performed (c). Finally, the metallic layers that compose the serpentine metallic path are sputtered (d). The heights of the layers are not at scale.

4.2.2 Serpentine path patterning

The next step is to pattern the previously deposited layers to define the serpentine path structure, whose design is presented in Figure 28. To do it so, a photolithography step is performed.

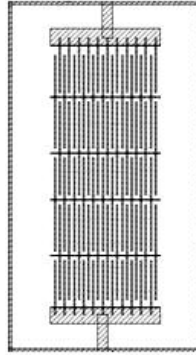


Figure 28 – Layout transferred during the DWL patterning. This mask will be transferred using a laser and will pattern the photoresist that allows defining the metallic layers that will compose the structure of the device.

Since the photoresist is going to be coated on top of a metallic layer, it is necessary to improve its adhesion by performing a dehydration step, as recommended in Appendix IV – Figure 76. The dehydration process is performed on the same coating machine as the photoresist is coated. For this process a pre defined recipe is chosen having into account the desired thickness to be coated, as can be consulted using Figure 77 from Appendix IV. In this case, a $2\mu\text{m}$ positive photoresist, AZ9221, is used as a sacrificial layer to transfer the desired pattern. The thickness of the photoresist is chosen according to the thickness of the metallic layer, which theoretically is 260nm thickness. Once the coating of the photoresist is performed it is necessary to cure it at 105°C [85] during 130s to solidify the photoresist.

Afterwards, the photoresist is exposed to transfer the designed pattern, presented in Figure 28, using a Direct Writing Laser (DWL) Technique. Another option would be manufacturing a hard mask and expose the photoresist directly using that same mask. However, the manufacturing process of the heaters is not meant to be a mass production process and so it was decided to use a DWL technique due to production costs. The details concerning the DWL process can be found in Appendix IV – Figure 78.

The next step is to develop the photoresist. Since the photoresist used is positive, the parts where it was exposed will be removed during the development, because the exposed photoresist becomes soluble to the remover (AZ400K). For further details consult Appendix IV – Figure 79.

Lastly, a photoresist reflow is performed. The reflow process allows curving the photoresist vertical walls, Figure 29 – (b), which is desirable since the next step of the process will consist on etching the exposed metallic layers. Consequently, if the photoresist walls are completely vertical, during the etching process there is an increased probability for the etched metallic particles to accumulate on the corner's interface between the metallic layers and the photoresist, leading to the creation of fences, Figure 29 – (a).

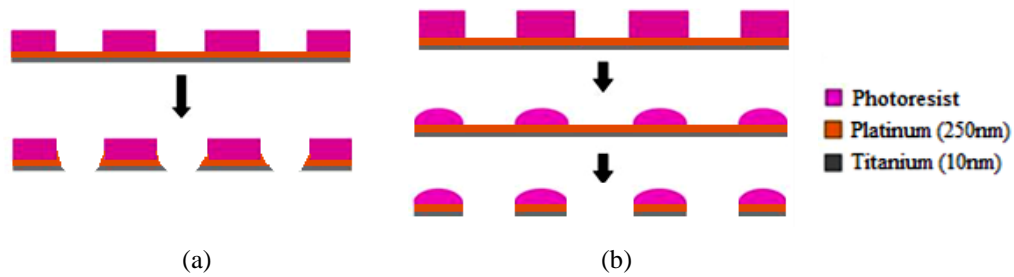


Figure 29 – Illustration of the photoresist reflow process. If the reflow is not performed, then, during the metal etching process of the underneath metallic layers fences can occur due to accumulation of particles on the corners of the interface between the two layers (a). If the reflow is performed the curvature of the top surface of the photoresist will prevent particle's accumulation in the interface between the two layers (b).

The reflow process is performed by placing the wafer on top of a hotplate at 115°C during 3min. Thus, the solvent present on the photoresist is evaporated and consequently the photoresist is compressed and curved. It is important to notice that if the compression due to the evaporation of the solvent present on the photoresist is too high, the underneath layers can peel or crack, which is not desirable. Such problem justifies the long time and temperature of the reflow process. Since only the top surface of the photoresist is not attached to the remaining layers, the curvature occurs only at the top due to the adhesion forces between the photoresist and the metallic layer underneath it. By the end of the photolithography process the layer cross section illustrated in Figure 30 – (b) on the wafer is obtained.

After the photolithography process, the exposed metallic layers can be etched, defining the serpentine path for the heater. A pure physical etching process is performed using an ion beam, which is bombarded against the surface of the wafer. The ions from the beam impinge on the exposed surface of the metallic layers, removing their atoms due to the kinetic energy being transferred. To ensure that the corners in the interface of the photoresist with the metallic layers are also etched, the wafer is placed with a 10° angle of inclination on the substrate holder. A secondary mass ion spectroscopy system is used to detect the end point for the etching process, ensuring that only the desired layers were etched. At this point, the structure for heater serpentine path has been micro machined, as illustrated in Figure 30 – (c).

The final step for defining the serpentine path is to perform a photoresist strip to remove the remaining photoresist used in the previous photolithography step. The photoresist strip is performed in 2 separate processes: a physical and a chemical strip. Firstly, the physical strip of the photoresist is performed by exposing the wafer to an oxygen plasma (further details in Appendix IV – Figure 80). The initial physical strip is responsible for striping the hardened crust that composes the photoresist surface due to the reflow process. The physical strip performed etches approximately 350nm from the 2 μ m of photoresist initially coated. Then, a chemical etching strip removes the remaining photoresist (see Appendix IV – Figure 81 for further details). Finally, to ensure that all the photoresist was properly removed, an additional 30s oxygen plasma was performed. At this point the wafer has the layer composition indicated in Figure 30 – (d).

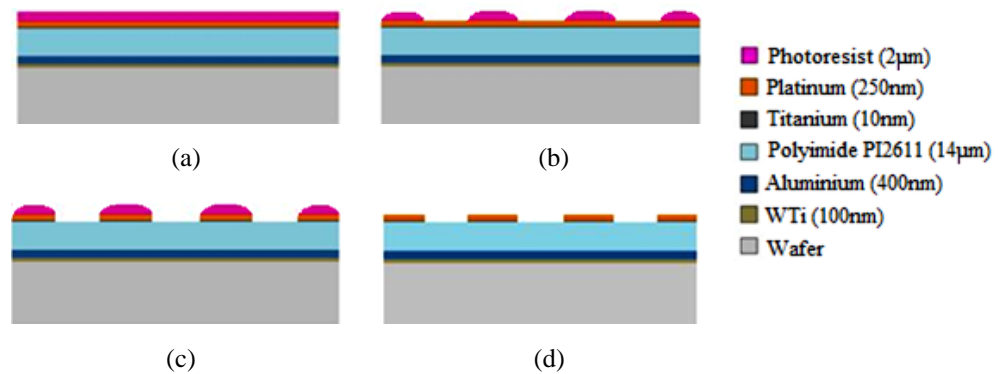


Figure 30 – Illustration of the cross section of the layers to define the serpentine path. A photoresist coating is initially performed (a). Then, the photoresist is patterned using a DWL technique exposing the metallic layers underneath (b). An ion beam etching patterns the metallic layers exposed (c). Finally the photoresist used as sacrificial layer is stripped (d).

In order to evaluate if the dimensions after the etching process were in agreement with the dimensions of the design, microscopic observations were performed. The results are presented in Figure 31. Despite some observed discrepancies, the dimensions are close to those conceived in the initial design. The reason for the mismatching dimensions can be explained by the 10° angle at which the wafer was placed during the etching process of the metallic layers that compose the serpentine path. Thus, an over etch of the metallic layer might have occurred, which explains the fact of the dimensions of the metallic layer are smaller and the size of the gaps between two consecutive beams are greater than expected.

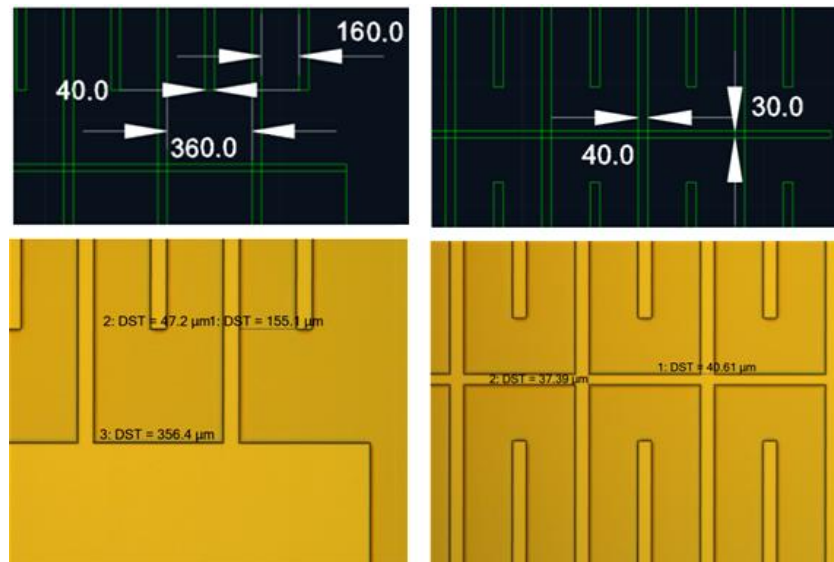


Figure 31 – Comparison between the dimensions of the design on the CAD (upper images) and the dimensions of the structure observed under the microscope (lower images).

The height measurement of the metallic layers was performed using a profilometer, allowing the measurement of the step between the metallic layer and the polyimide underneath it, as shown in Figure 32.

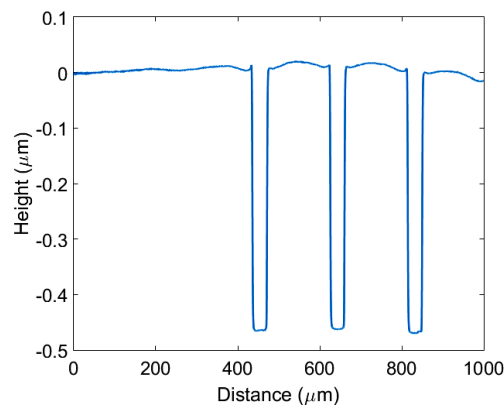


Figure 32 – Profilometer measurement in order to determine the step height of the metallic layers.

According to the designed model, the expected height of the metallic layer was approximately 10nm of Ti + 250nm of Pt = 260nm in total. However, from Figure 32 it is possible to observe three minimum peaks with height values of 465.8nm, 463.5nm and 470.3nm. The difference between the expected and the obtained results lies on the previous photoresist strip with oxygen plasma performed after the chemical strip. Since the oxygen plasma is not selective to the chemical species to etch and the polyimide etch rate is very close to the photoresist, an over etch of the polyimide layer underneath the metallic layer occurred. Thus, if we take this into account and recalculate the expected step height, one obtains the result shown in equation (23).

$$\text{Step height} = 10\text{nm} + 250\text{nm} + \frac{350\text{nm}}{1\text{min}} \times 30\text{s} = 435\text{nm} \quad (23)$$

This value only differs by a maximum of 35.3nm difference to the measured height, which can be explained by small differences of the height of the Titanium and Platinum layers. Still, this over etch is not a problem since a new polyimide layer will be coated on top of the surface of the wafer to insulate the metallic layers that composes the heater.

4.2.3 Mesh pattern structure

To define the mesh pattern an insulating layer to isolate the metallic layers needs to be coated. The polyimide coating process is carried out as previously performed for the first polyimide layer, with the exception for the polyimide type being used (PI2610) and the thickness being coated, 2 μm . The difference between the two types of polyimide is the solvent concentration used to dilute the polyimide, being the PI2610 less viscous. At this point, all the layers that compose the final structure of the device are stacked on top of the wafer and the serpentine path structure is defined, as shown in Figure 33 – (a). However, it is still necessary to pattern the final structure to define the mesh pattern that allows the device to become stretchable. Thus, a new photolithography step is performed.

Prior to the second photolithographic step, a 300nm layer of Silicon Dioxide, SiO₂, Figure 33 – (b), is sputtered on top of the coated polyimide layer. This new layer aims to function as a hard mask for the second lithographic step. Since it is necessary to etch approximately 16 μm of polyimide (14 μm +2 μm) and the etch rate of the polyimide is very close to the etch rate of the photoresist, it would be necessary to deposit a layer of 20 μm of photoresist to ensure that the etching process goes through the entire exposed polyimide layer. However, a 20 μm photoresist coating is not recommended since the baking process for curing the photoresist would induce a great amount of stress on the polyimide surface underneath, which could possible lead to its peeling/delamination or cracking. Thus, the Silicon layer protects the polyimide layer and so, the thickness of the photoresist layer to be coated is diminished.

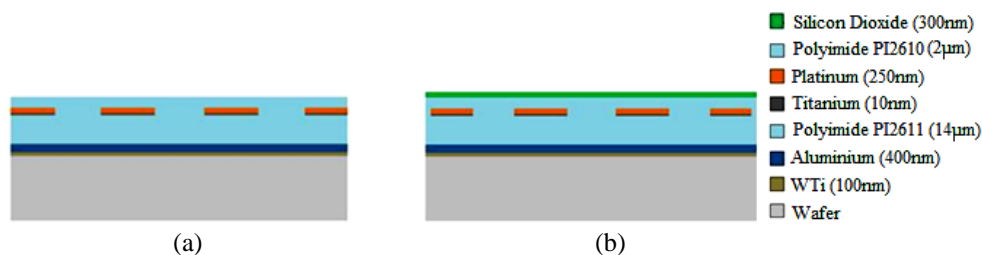


Figure 33 – Illustration of the layers cross section prior to the photolithography step. A polyimide layer is initially coated (a) and a silicon layer is sputtered to act as a hard mask (b).

Once the SiO₂ layer is properly sputtered, it is time to proceed to the second photolithography process. As a result, the slits of the stretchable heater mesh will be defined. The second photolithography process is performed in the same way as the first photolithography with the exception of the transferred design, as shown in Figure 34.

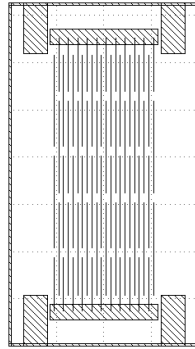


Figure 34 – Layout for the second photolithography step. This mask will be transferred using a laser that will pattern the photoresist defining the structure of all the polyimide layers previously coated. In order to align this design with what has already been manufactured, alignment crosses are used.

In addition, to the structure to be patterned, it is necessary to take into account the alignment between the new design and what has already been micro machined. Thus, the overlapping design with the structure on the wafer is performed using alignment marks patterned in the first photolithography step and on the design for the second photolithography. In the end of this process the sacrificial layer is patterned with the desired design for the mesh structure, as can be seen in Figure 35.

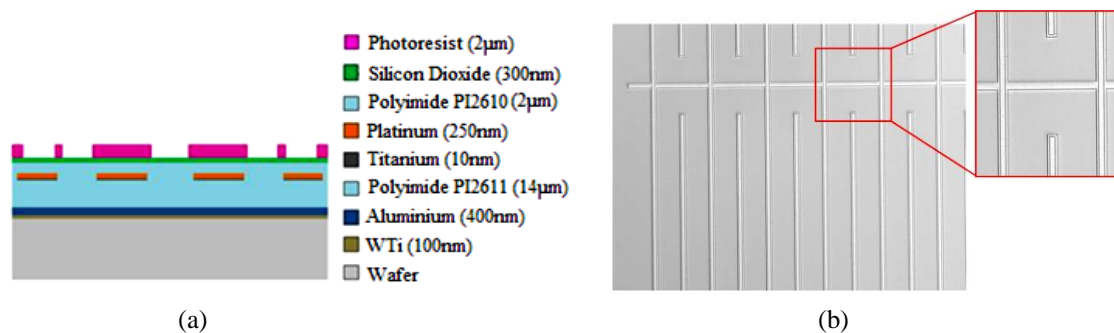


Figure 35 – Illustration of the cross section of the layers after the second photolithography step. The heights of the layers are not at scale (a). Microscopic observation of the photoresist patterned after the second photolithography step. As can be seen in the zoomed image the vertical lines in between different serpentine paths correspond to the location where the polyimide will be etched to define the mesh pattern for the stretchable structure.

With the sacrificial layer patterned, the remaining layers can be etched to obtain the final mesh structure. Initially, the Silicon Dioxide layer is etched using a dielectric etcher (SPTS APS). In this process an ICP (Inductive Coupled Plasma) is combined alongside with some gases that are introduced in the etching chamber, namely with He/H₂/C₄F₈. The combination

of alternating steps between chemical and physical etching allows achieving an anisotropic etch, which leads to steep walls with high aspect ratio. This process is also known as DRIE (Deep Reactive Ion Etching) [86]. The etching machine possesses an end point detection system that evaluates the spectroscopy of the light spectra emitted by the plasma during the etching process [87]. Since the light emitted differs from layer to layer due to their physical and chemical properties, the light spectra will also differ, being therefore correlated with the layer being etched. As a result, the process can be manually stopped once the end point is reached.

Initially, the exposed Silicon layer is etched allowing accessing to the polyimide layer that will be etched to define the slits of the mesh pattern, as illustrated in Figure 36 – (a). Then, the polyimide layers are etched to provide access to the contact pads and define the mesh structure of the device, as shown in Figure 36 – (b). Once the polyimide etching process is concluded, a new resist stripping, like the ones previously described, is performed to remove the sacrificial layer, as depicted in Figure 36 – (c). Afterwards, a new dielectric etching process is performed to remove the remaining Silicon Dioxide used as a hard mask, Figure 36 – (d).

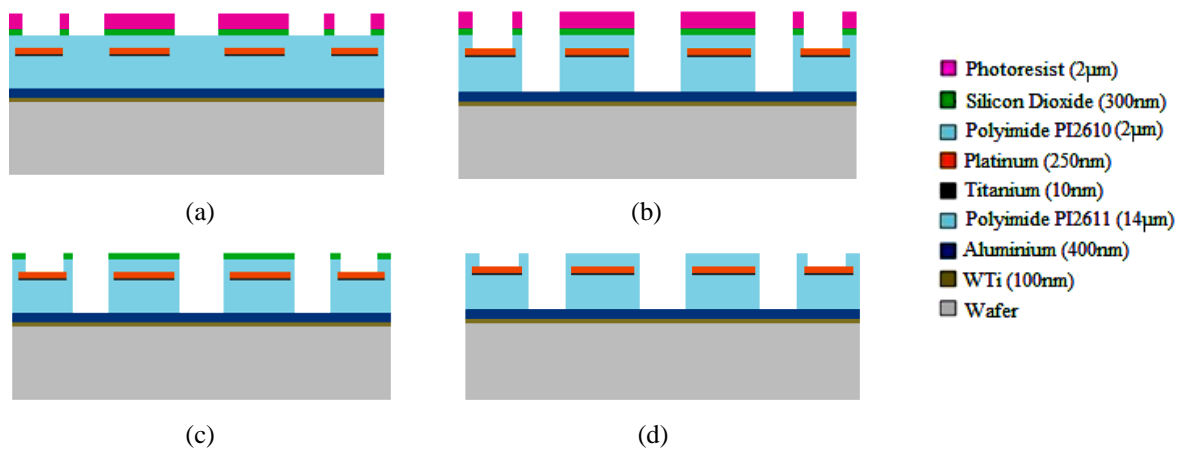


Figure 36 – Illustration of the cross section of the layers after the mesh pattern is defined. The SiO_2 is etched to provide access to the polyimide layer (a). The polyimide layer is then etched, defining the mesh pattern and providing access to the contact pads (b). Finally, the sacrificial layers are etched (c) and stripped (d). The heights of the layers are not at scale.

However, during the etching process of the remaining Silicon Dioxide, the metallic layers for the contact pads, exposed to the plasma, were also etched, Figure 37. An explanation for what succeeded was found on failing in the detection of the endpoint for the etching process of the Silicon layer. Since there was not a stopping layer, such as a Titanium layer, between the Silicon Dioxide and the Platinum layer, during the final etching process, there was not

enough differentiation between the two layers due to the small difference between the emission intensity of them [87].

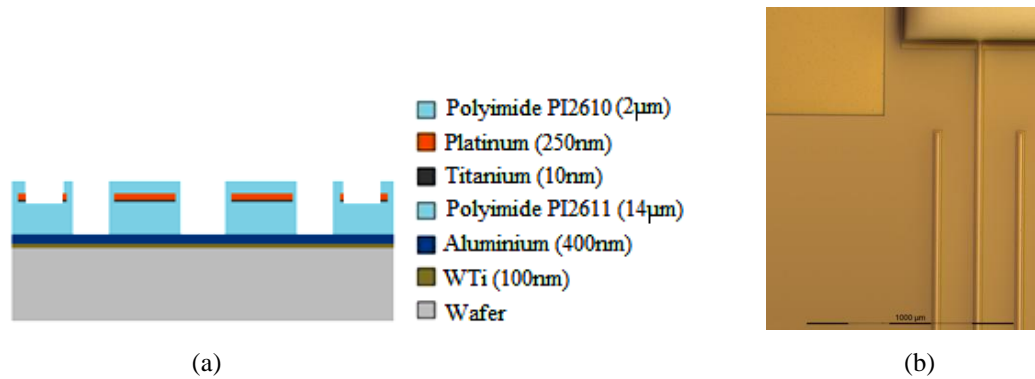


Figure 37 – Illustration of the cross section of the layers after the remaining SiO_2 is etched (a). As can be seen the metallic layers that compose the contact pads were also etched, which was not expected. The heights of the layers are not at scale. Microscopic observation of the contact pads after the SiO_2 and polyimide etching process (b). As can be seen in the figure above, the contact pad (at the left upper corner) does not possess any metal left.

Consequently, a new plan had to be put in practice in order to define the new contact pads. This way, a new L-shaped contact pad, as shown in Figure 38, was designed.

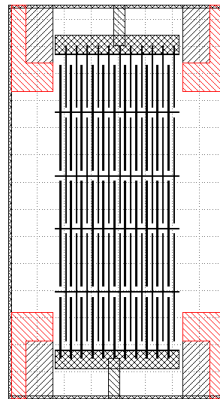


Figure 38 – Layout for the third photolithography step. The mask will be transferred using a laser and will pattern the photoresist that will define the structure of the new contact pads (shown in red).

To pattern the new shape for the contact pads, a third photolithography was performed. Since the Silicon Dioxide was all removed, in order to avoid any risk it was decided that a photolithography with a thicker resist would be performed. Since the polyimide that will be etched has a thickness of $2\mu\text{m}$, a $14\mu\text{m}$ photoresist coating was performed, as illustrated in Figure 39 – (a). Due to the thickness needed to be coated a different photoresist was used, AZ9260. Such photoresist is used in high topography substrates to achieve steep walls with high aspect ratio. Moreover, due to its high density a thick film can be coated, as desired. Like in any other photolithography performed during the presented manufacturing process, the

photoresist is initially coated, then, exposed and finally developed, resulting in a cross section similar to the one illustrated in Figure 39 – (b).

Once the L-shaped design for the contact pads has been transferred to the photoresist a new etching step for the polyimide on top of the metallic layer that will define the contact pads is performed. The etching process is performed on a different machine (STS Multiple ICP) to avoid passing the endpoint detection. In this case, an oxygen chemistry plasma is used to etch the polyimide and differently to the previous etching process, the endpoint detection consists now in the analysis of light interferometry. Thus, as the polyimide layer is etched, a laser is pointed to its surface and the incident light is reflected in the interfaces between different layers. As a consequence, the reflected beams will interfere with each others, either constructively or destructively, creating a sinusoidal intensity signal with periodic oscillations called fringes [87]. Thus, as soon as the polyimide layer is fully etched the fringes disappear and a constant signal is measured. At this point the etching process is manually stopped, resulting in the exposure of the contact pads, as illustrated in Figure 39 – (c).

Finally, a new resist strip is performed in order to remove the remaining photoresist. At this point the manufacturing process of the device is finished, with a cross section as the one depicted in Figure 39 – (d).

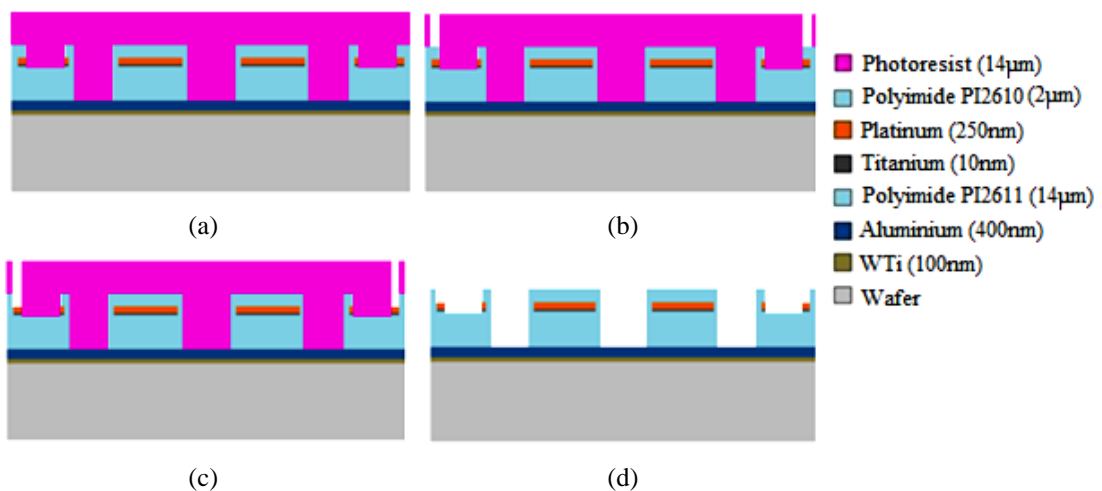


Figure 39 – Illustration of the cross section of the layers after the new photolithography step. Initially, the photoresist is coated (a) and then exposed and developed (b). The polyimide layer is etched where the photoresist was removed (c). Finally, the remaining photoresist is removed (d). The heights of the layers are not at scale.

The microscopic observation of the contact pad is shown in the Figure 40.

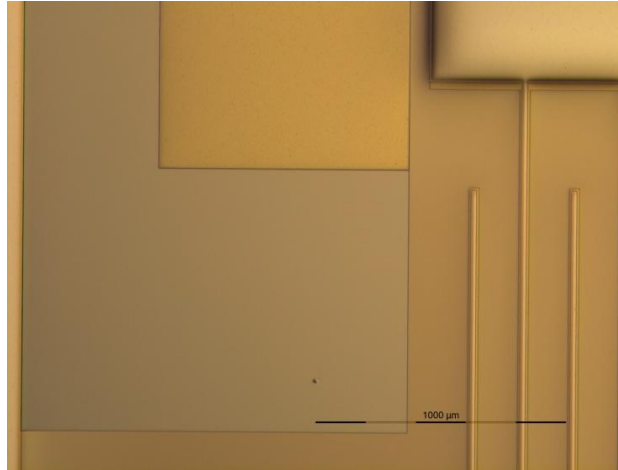


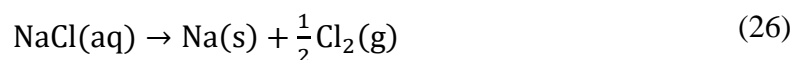
Figure 40 – Microscopic observation of the new L-shaped contact pads. The metallic layer is shinier indicating the presence of metal.

4.2.4 Device release

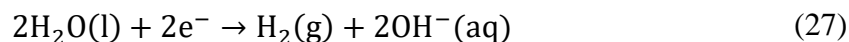
Finally, an anodic dissolution is performed in order to release the devices from the wafer. The anodic dissolution consists in an electrochemical oxidation of a metal surface resulting in the liberation of ions into the electrolyte [88]. Initially, a solution of Sodium Chloride is prepared and the wafer is placed in the solution along with a Platinum wafer used as a cathode, as shown Figure 41. A voltage supplier is then connected to both wafers and an electric current is passed through the electrodes to the molten salt where chemical reactions take place at the electrodes. Since the Aluminium produces cations during its oxidation, the wafer must be connected to the positive terminal of the power supply, to attract the anions. The chemical process leads to a chain of chemical reactions presented below. Thus, since the first polyimide layer is attached to the Aluminium layer, the devices are released from the wafer while this layer is oxidized. As the Aluminium is oxidized, the Tungsten-Titanium is not affected and continues to be used as an electrode to allow the current to pass through the wafer. The schematic of the setup along with the chemical reactions are as followed [89, 90].



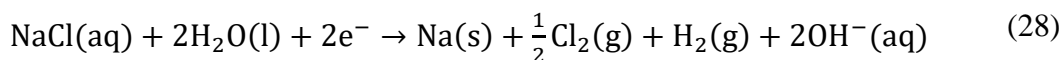
The Sodium and Chloride ions, Na^+ and Cl^- , respectively, react one with each other to form Sodium Chloride, NaCl , as shown in equation (26).



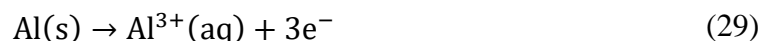
On the other hand, the reduction equation for water molecules, H_2O results in Hydrogen molecules, H_2 , and Hydroxide ions, OH^- , as equation (27) demonstrates.



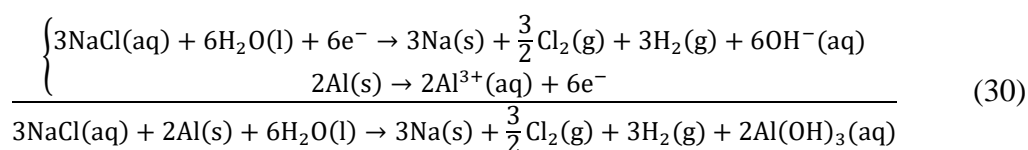
Therefore, equation (28) is the equilibrium equation when combining Sodium Chloride with water.



The oxidation equation for the Aluminium is given by equation (29), where the Aluminium loses an electron and forming an Aluminium ion.



Thus, the reduction-oxidation equation for the Aluminium in water is given by the set of equations (30).



, which results in Sodium solid particles, $\text{Na}(\text{s})$, and gases, $\text{Cl}_2(\text{g})$ and $\text{H}_2(\text{g})$, that form bubbles during the anodic releasing process, as it was observed during the process. The final device is shown in the microscopic observation present in Figure 42 – (a) and with a layer cross section composition illustrated in Figure 42 – (b).

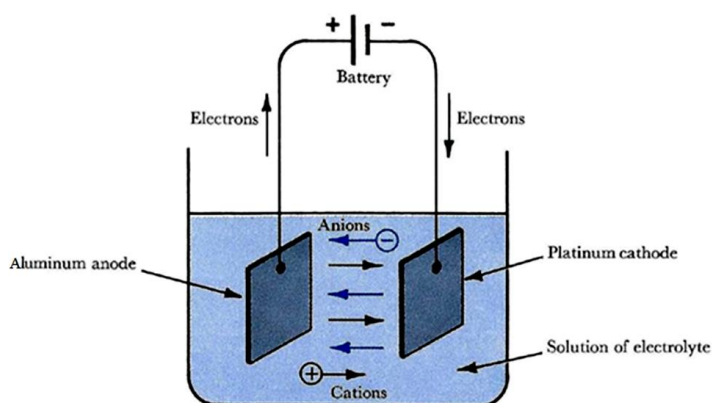


Figure 41 – Illustration of the anodic dissolution setup and its working principle.

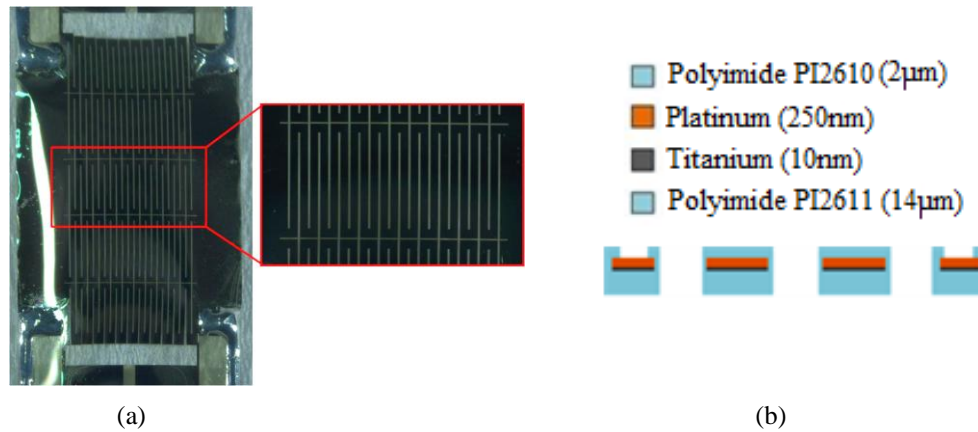


Figure 42 – Final stretchable heater. Microscopic observation of the stretchable device. In the right side of (a) one of the five serpentine paths is zoomed in. In (b) is illustrated the cross section view of the layers that compose the final device.

Finally, a multimeter was used to determine the resistance value of the heaters manufactured. A batch of 20 devices was produced during the cleanroom process presented in this thesis. The average and standard deviation for the resistances value measured directly was of $(31.54 \pm 1.29)\Omega$, which differs from the theoretical value of 33.94Ω by a minimum and maximum resistance value of 1.11Ω and 3.69Ω , respectively. The difference can be explained by small differences on the dimensions obtained during the manufacturing process, as presented in Figure 31. Thus, since the heaters presented a low resistance value, a small difference on their dimension represents a deviation with a greater contribution. Even though, it is possible to conclude that the manufacturing process was successful since it allowed to obtain the desired structures with dimensions near the conceived in the initial design, demonstrating the higher control achieved by the cleanroom manufacturing process.

4.3 Stretchable heater characterization

In this section, the previous manufactured stretchable heaters are characterized and the possibility of using them as temperature sensors is explored. The **resistance change** can occur as a result of two effects: **mechanical deformation** and **temperature variation**.

The **mechanical deformation effect** is due to the transformation from a stretching deformation into a bending deformation in the micro-beams around the notch that connects the different micro-beams of the serpentine path [67]. As a result, different parts will be in compression and in tension, as presented in Figure 43. The metallic serpentine path is composed by periodic micro-beams with the same distance between each other. Thus, it is expected that their tension and compression contributions to the deformation effect are equally distributed. As a result, the device is rather insensitive to strain, since the effect of the

parts in tension and compression cancel each other out. Thus, **the only effect causing the resistance change should be the temperature change** due to heating dissipation.

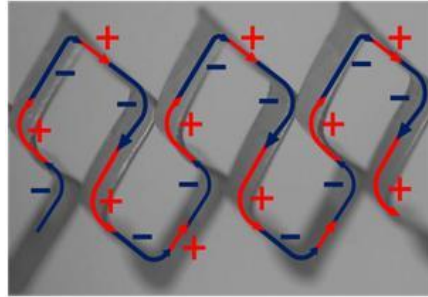


Figure 43 –Stretchable mesh. The mechanical deformation causes the micro beams to twist out-of-plane and bend about their axis of lowest moment of inertia, which requires less energy leading to positive and negative strain in different sections of the metallic layer. Since the metallic layer is uniform and the micro beams present always the same dimensions the different sections of the metal layer in tension and compression cancel each other out, making the device rather insensitive to strain.

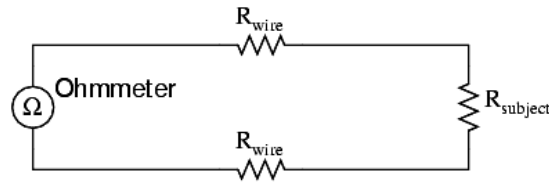
Concerning the **temperature effect contribution** to the resistance change, it is known that the resistance change due to the temperature variation is described by equation (31).

$$R = R_{ref}[1 + \alpha(T - T_{ref})] \quad (31)$$

,where R represents the resistance for a given temperature T , R_{ref} it is the conductor resistance for a given reference temperature T_{ref} (in general 25°C) and α is the temperature coefficient of resistance. This coefficient represents the resistance variation factor per temperature degree [91]. Thus, according to equation (31), it is expected that the resistance changes linearly with temperature.

4.3.1 Resistance measurement and acquisition

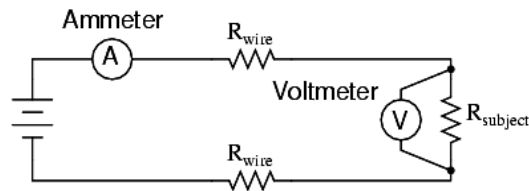
One of the main challenges of being able to measure the resistance of the stretchable heaters is to **cancel the wire's resistance during the measurement**. In order to measure the resistance of the heaters in real time, the current passing through the heater and the voltage drop across it needs to be acquired in real time. So, long electrical wires need to be soldered and attached to device, which represents a problem. Usually, the wire's resistance is very small, only a few ohms, depending primarily on the gauge (size) of the wire. However, if the connecting wires are very long, and/or the component to be measured has a very low resistance, as it is the case, the measurement error introduced by the wire's resistance will be substantial [91], as illustrated in Figure 44. Therefore, a **sensing method** needs to be designed in order **to cancel the contribution from the wire's resistance**.



Ohmmeter indicates $R_{\text{wire}} + R_{\text{subject}} + R_{\text{wire}}$

Figure 44 –Equivalent circuit for measuring the resistance of the device when long wires are connected to it [91].

A **4-wire sensing method**, also known as Kelvin’s sensing method, consists on **measuring the device’s resistance using an Ammeter and a Voltmeter**, Figure 45. Thus, using Ohm’s Law it is possible to determine the resistance of the component by measuring the current going through the heater and the voltage dropped across it.



$$R_{\text{subject}} = \frac{\text{Voltmeter indication}}{\text{Ammeter indication}}$$

Figure 45 –Equivalent circuit for measuring the resistance of the device using Kelvin’s method [91].

At first it appears that there is not any advantage on this method, since one is measuring the voltage through a long pair of resistive wires, introducing resistance back into the measuring circuit. However, the current is the same at all points, and so the length of the wires is not a problem, since they are connected in series with the heater. The same does not apply to the voltage measurement, leading to a new connection by another pair of wires containing resistance. Even though, if the resistance of the voltmeter is high compared to the resistance being measured on the heater, the current passing through the wires is small, as illustrated in Figure 46.

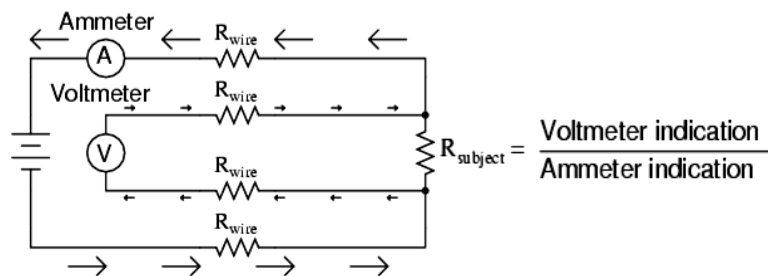


Figure 46 –Equivalent circuit for measuring the resistance of the device using Kelvin’s method and having into account the effect of the wires resistance for the voltmeter connection. Although the long wires introduce a new resistance, the current that flows through these wires is almost zero and so its effect can be neglected [91].

Thus, those long wires connecting the voltmeter across the subject resistance will drop insignificant amounts of voltage, resulting in a voltmeter indication that is nearly the same as if the voltmeter was connected directly across the heater [91].

The designed circuit has four main blocks (as can be seen in Appendix V – Figure 85):

- **Heater driving circuit**, composed by a NMOS working as a switch to input a PWM signal to the heater, allowing to control the temperature achieved by it.
- **Voltage sensing circuit** composed by a differential amplifier to measure the voltage across the heater.
- **Current sensing circuit** composed by an instrumentation amplifier INA225.
- **Active filtering stage** to filter the noise of the electric network, 50Hz.

The heater driving board consists on a N-channel MOSFET working as a switch. A SSM3K09FU N-channel MOSFET was chosen due to its characteristics, mainly the switching time and the low drain-source resistance value [92]. **Depending on the PWM signal** being input, which varies between GND and 3.3V being applied by a Teensy 3.6 board, **the MOSFET is at a cut-off or saturation region**. The gate input voltage, V_{GS} , is taken to a positive voltage level to turn the device “ON” ($V_{GS}=3.3V$) or at a zero voltage level to turn the device “OFF” ($V_{GS}=0V$). Thus, when the PWM is at zero, the gate of the MOSFET is grounded, and so $V_{GS}<V_{th}$ (where $V_{th}=1.8V$ for SSM3 N-channel MOSFET). As a consequence, no drain current flows ($I_D=0A$) and so the MOSFET operates as an open switch (cut-off region). Also, a $10k\Omega$ gate-charge resistor is used to reduce the gate-source voltage to 0V when the input signal is open-circuited [93]. On the other hand, when the PWM signal is High, the gate-source voltage is greater than the threshold voltage $V_{GS}>V_{th}$ and a maximum drain current flows ($I_D=V_{DD}/R_{heater}$). Ideally, $V_{DS}=0V$, but due to the drain-source resistance value, a very small voltage output, approximately zero, will be dropping at V_{DS} [94], [95]. As a result, the MOSFET operates as a low resistance (closed switch) and the 9V being applied at HEAT 1 activates the heater, raising its temperature. Thus, **modulating the duty cycle** of a 915.527Hz PWM signal, as described by equation (32), **different temperature values are achieved by the heater**, as shown in Figure 47. The PWM frequency is chosen based on the desired resolution (16-bits) and the CPU speed (180MHz) [95].

$$\text{"ON" Time (s)} = \frac{\%duty\ cycle}{915.527Hz} \quad (32)$$

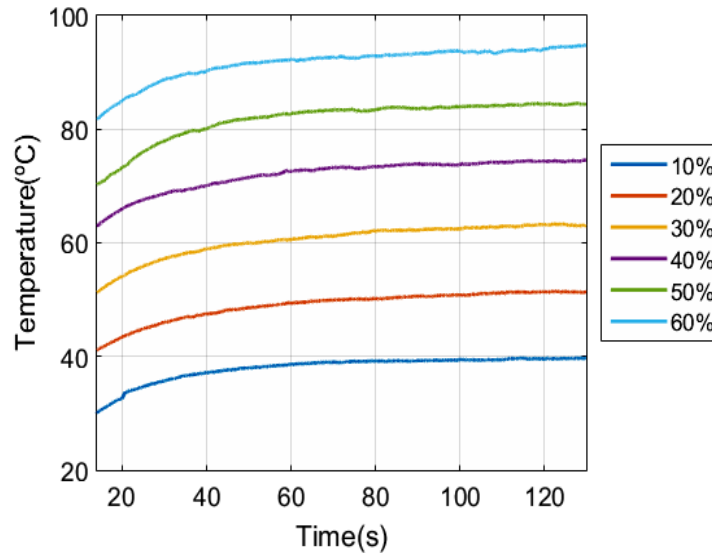


Figure 47 –Assigning different duty cycles for the input PWM signal allows achieving different steady temperatures.

The **voltage sensing circuit** is composed by a simple differential amplifier with 1/3 gain and a voltage follower. The chosen gain value is due to the maximum input voltage that can be applied to the input pins of the Teensy board. On the other hand, the voltage follower provides electrical impedance transformation, preventing the signal source from being affected by voltages that the load may produce. An OP4428 operational amplifier [96] (Op Amp) with dual supply was used, due to its high response speed with a slew rate of $10\text{V}/\mu\text{s}$ and bandwidth of 33MHz. Such characteristics are desired, allowing maintaining a high precise and fast response to the voltage drop being measured for the applied PWM signal. The operation amplifier is supplied using a 12V and -12V DC/DC converter to avoid saturating when the 9V signal is applied to the heater. Furthermore, decoupling capacitors are used on the power supply for shunting the noise caused by the remaining circuit elements, reducing therefore its effect on the rest of the circuit.

The **current sensing circuit** is composed by a current sensing-amplifier (INA225) [97] that senses drops across current-sensing resistors and has a voltage output corresponding to the current sensing value. The INA225 high signal bandwidth allows higher precisions measurements, enabling current-sensing with maximum drops across a shunt resistor as low as 10mV, reason why it was chosen. Furthermore, the possibility of choosing between four discrete gains is an advantage, since the gain can be chosen based on the desired sensitivity and dynamic input range. Thus, a discrete gain level of 50V/V was selected applying different tensions to two gain-select terminals (GS_0 and GS_1) and a $300\text{m}\Omega$ shunt resistor was chosen as the current-sensing resistor. The selected value for the shunt resistor was based on the required accuracy of the current measurement and power dissipation. The larger the voltage

across the resistor, the more accurate of a measurement can be made. However, power dissipation and the voltage drop across this resistor have to be taken into account. Thus, if a 3.3V full-scale output voltage is desired and the selected gain is 50V/V, a power dissipation of 14.5mW is required, which is **acceptable for the application** presented [97].

Finally, an **active filtering stage using a 2nd order filter with Sallen-Key configuration** is used as a low pass filter with unitary gain to remove the network noise of 50Hz and obtain the DC value of the PWM signal being measured. In order to do it, a MCP6292 rail-to-rail operational amplifier is used, since these Op Amps are usually recommended for this type of filtering stages applications, as can be seen according to the manufacturer datasheet [98]. The Sallen-Key filter design is one of the most widely known 2nd order filter designs. The main advantage of this topology relies on requiring only a single Op Amp for the gain control and four passive RC components to accomplish the tuning [99] while allowing obtaining a steep roll-off rate(-40dB/decade) that is twice than 1st order filters [99]. Thus, the quality of the filter is improved since the signal will be cut very near the cut-off frequency without compromising the remaining frequencies. The dimensions for the RC components can be found in Appendix V. The filter presents a good quality factor ($Q=0.703$) and a damping factor ($\zeta=0.711$) near the critically damped value of $\zeta=0.7071$ [99], revealing that the frequency response is near the correct value.

4.3.2 Temperature effect contribution

As previously mentioned the **PWM signal is responsible for controlling the temperature** being reached by the heater. In this section we present the heater characterization by measuring its resistance when different duty cycles are assigned to the input signal. The repeatability and variability response of different heaters to temperature variations are presented.

The repeatability and variability of the resistance of the heaters to temperature effects were initially studied using a thermal camera. To test the **repeatability of the heater under the same temperature conditions** the following protocol was defined: Initially, **one random heater** is chosen and **three sets of tests** are performed. In **each set** of tests **the duty cycle range varies from 10% to 60%**, due to the possibility of damaging the heater since the temperature reached is higher than 100°C, **in 10% steps**. **For each duty cycle** the heater is activated during **90s to reach a steady state temperature** and **30s of data are acquired** afterwards. To test the **variability**, the **same protocol** was applied to each of **three different**

random samples. The resistance was measured using the circuit presented in subsection 4.3.1. The mean normalized resistance is then calculated to minimize the weight of possible outliers or remaining noise contributions and bias conditions such as the initial resistance value of the heater at room temperature. The results for both tests are presented in Figure 48.

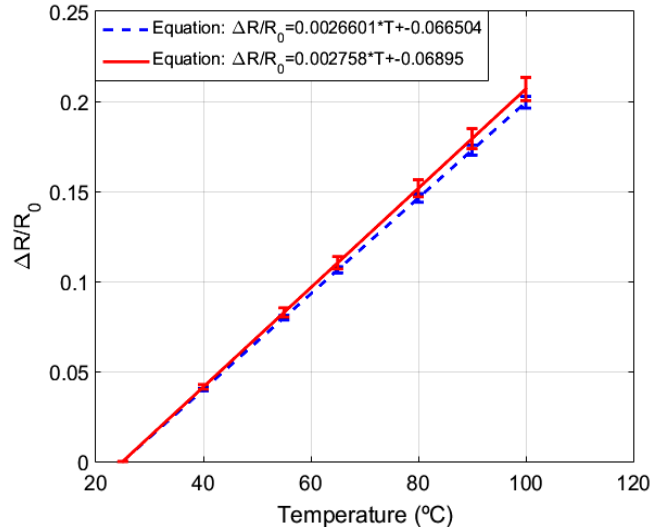


Figure 48 – **Repeatability** and **variability** test the stretchable heaters. The **resistance increases linearly** with temperature according to the equations shown on top of the chart. Each point represents 3 tests for a given temperature achieved by a duty cycle assigned value. The error bars represent the standard deviation per set of 3 tests. The blue dashed line represents the repeatability results while the red line represents the variability results.

As expected according to equation (31), the **resistance changes linearly with the increasing temperature**. For both study cases the equations that relate the normalized resistance with the temperature are presented. The heaters demonstrated **high repeatability** with a maximum error of 1.62% of the normalized resistance value. Concerning the variability, the maximum error was 3.11% of the normalized resistance value. Thus, the **resistance of the heaters can be correlated with their temperature** according to equation (33) with a maximum error of 3.11%.

$$\frac{\Delta R}{R_0} = 0.002758T + 0.06895 \quad (33)$$

, where ΔR is the difference between the measured resistance and R_0 , which represents the resistance value at room temperature $T_0=25^\circ\text{C}$.

4.3.3 Mechanical deformation effect contribution

Concerning the **mechanical deformation effect** on the heater resistance, the following protocol was applied. Initially the ASL is heated during 120s, at a 35% duty cycle PWM

signal, reaching an equilibrium temperature of 85 ± 3 °C. Then, the **ASL attached to the finger is bent three times with the same tendon displacement**, until reaching the joint limit. The resistance is measured and the result is presented in Figure 49.

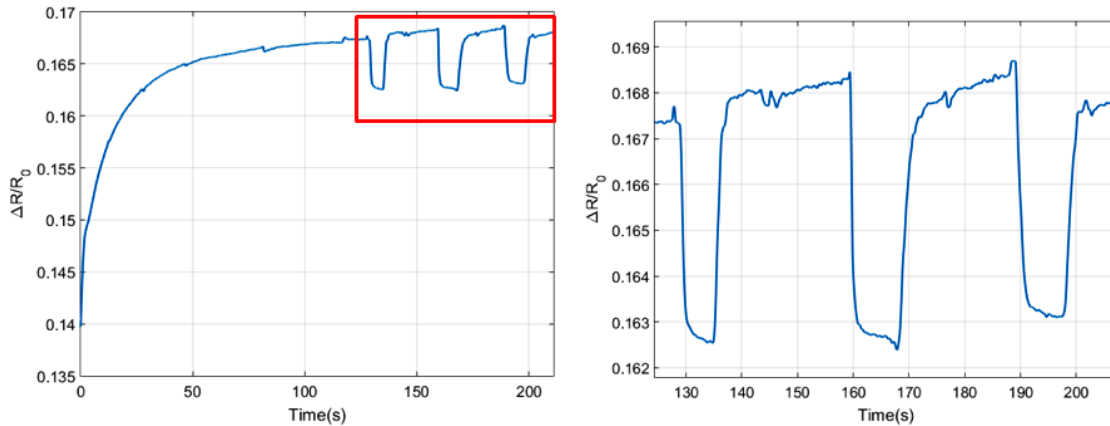


Figure 49 –The temperature and mechanical deformation effects on the resistance of the heaters were studied by initially activating the heater during 120s, after which a bending motion was applied three times, as zoomed in the left figure.

The strain caused by the heater deformation causes a resistance change on the heater, which can affect the heater temperature being reached. As it is possible to observe, the resistance change due to temperature effect until equilibrium is reached is 16.74% of the normalized resistance value, while due to mechanical deformation is (0.47 ± 0.04) %. Thus, the mechanical deformation contribution is more than 35 times lower than the temperature effect contribution. However, it cannot be neglected and so the heater can only be used as a temperature sensor to achieve the desired ASL stiffness before the heaters are stretched, as shown in Figure 50 [4]. During the bending motion the resistance value of the heater will vary. Once the joint is restored to its pre set position, a maximum drift of (0.10 ± 0.03) % of the normalize resistance value is expected.

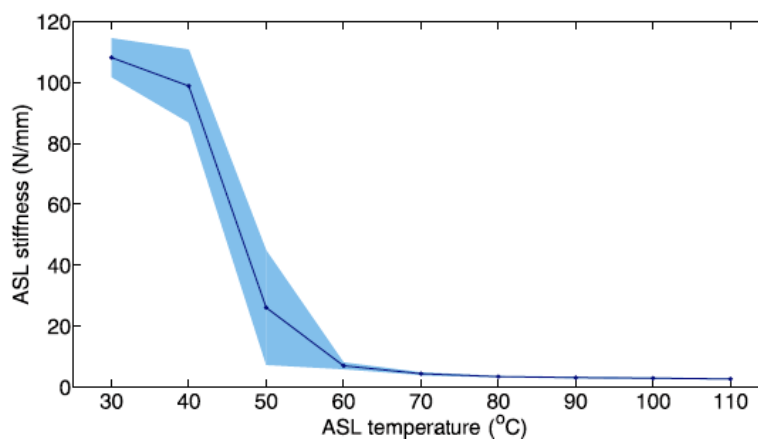


Figure 50 – Stiffness of the ASL as a function of its temperature. The shaded area shows the standard deviation of the data points [4].

CHAPTER 5

TACTILE SENSING INTEGRATION

The integration of tactile sensors on the tendon-driven robogami under-actuated gripper allows studying the interaction between the objects being grasp and the gripper by quantifying the contact force exerted by the fingers [18] – [22].

In this chapter three industrial sensors are compared to choose the most suitable to be integrated in the gripper fingers. Once chosen, the contact sensors is characterized with further detail to develop a model that calculates the contact forces based on the operating conditions of the gripper. Finally, different grasp modes are assigned to the gripper by adjusting the ASL stiffness of the under-actuated fingers to grasp different sized objects, whilst integrating tactile sensors provides the feedback to study effective grasp configurations and hence improve grasping quality.

5.1 Tactile sensors performance comparison

The final step for the construction of the gripper is to integrate a tactile sensing system that allows studying the interaction between the gripper and the objects being grasped. Initially, three tactile sensors were considered: FSR 400 Short (from INTERLINK ELECTRONICS) [100], TakkStrip (from RightHand Labs) [101] and Capacitive Sensors (from SingleTact) [102], all shown in Figure 51. The sensors differ on their working principle, meaning that the sensors that compose the TakkStrip are barometric sensors [103], while the ones from SingleTact are capacitive and the FSR 400 Short ones are resistive sensors.

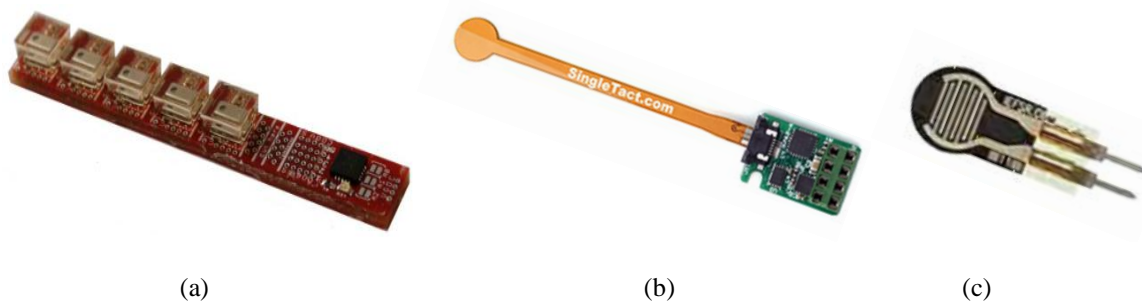


Figure 51 – Tactile sensors considered to be integrated on the tendon-driven robogami under-actuated gripper: (a) – TakkStrip; (b) – SingleTact; (c) – FSR400 Short.

In order to choose the most suitable sensor the following requirements are evaluated:

- 1) **Ease of integration**, i.e., the sensors should be integrated on the fingers tiles and should be compatible with the layer-by-layer manufacturing system for easy replacement if needed.
- 2) **Repeatability**, i.e., under the same loading conditions the sensor should present a repeatable response. Furthermore, their response needs to be characterized to correlate the sensor output with the amount of force being applied.
- 3) **Good response under different temperature conditions**. As can be observed in Figure 52, when the ASLs are thermally activated by the stretchable heater, the tiles of the fingers structure are heated as well due to the glass fiber layers being thermally conductive.

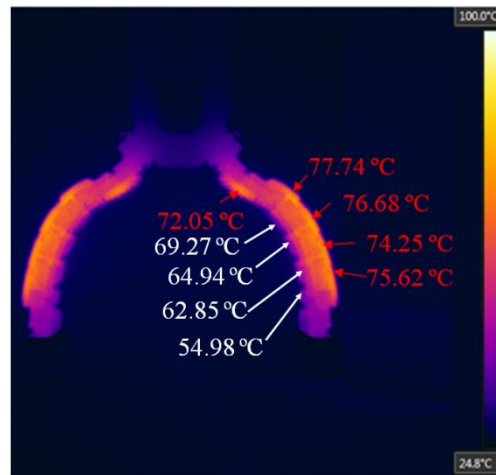


Figure 52 – When the heaters thermally activate the ASL layers the finger structure is heated as well due to the thermal conductivity of the glass fiber layers.

- 4) It is desirable that a **communication interface** has already been established, since it is not a goal of the project to develop an interface communication between the sensor and the host device to acquire the signals being measured.

In Table VII are summarized the sensors characteristics for closer comparison.

TABLE VII – Tactile sensors characteristics for comparison.

Characteristics	FSR 400 Short [100]	TakkStrip [101]	SingleTact [102]
Dimensions	Sensing area Circle of 5.6mm diameter	Sensing area <u>Thickness</u> : 3.5mm with silicone cast	Sensing area Circle of 8mm diameter
	<u>Thickness</u> : 0.30mm	<u>Length</u> : 5mm	<u>Thickness</u> : 0.35mm
	<u>Tail length</u> : 15.8mm	<u>Width</u> : 3mm	<u>Tail length</u> : 50mm
	<u>Tail width</u> : 6.35mm		<u>Tail width</u> : 3.5mm
Price	10.97\$	149\$/strip with 5 sensors and microcontroller	19.95\$ for the sensor + 29.95\$ for the electronic interface
Ease of integration	Compatible with the fingers dimensions and layer-by-layer manufacturing process	NOT Compatible with the fingers dimensions and layer-by-layer manufacturing process	Compatible with the fingers dimensions and layer-by-layer manufacturing process
Communication Interface	Not developed	I ² C communication	I ² C communication

As can be seen in Table VI, due to its dimensions, compatibility with the manufacturing process and ease of integration, the TakkStrip sensors were excluded. In order to decide between the remaining options, the sensors were submitted to tests under different heating and loading conditions.

The **protocol** followed for the experiments is illustrated on the flowchart of Figure 53. **Each sensor** is submitted to **two different temperatures**: room temperature (25°C) and 60°C, due to the temperature achieved by the tiles when the heaters are activated. For each temperature, **each sensor is loaded with weights ranging from 50gm to 200gm**, in 50gm increments. Finally **for each loaded weight at a given temperature three trials are performed** to get statistically significant results. A SMD thermistor is used to measure the temperature (NTCS0402E3223FMT by Vishay) [104] near the sensors.

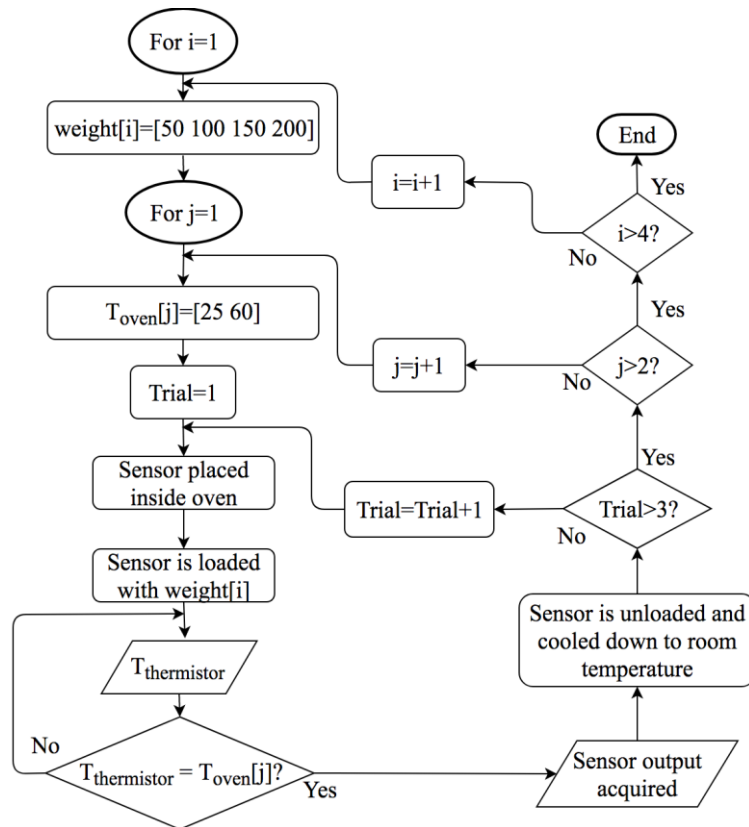
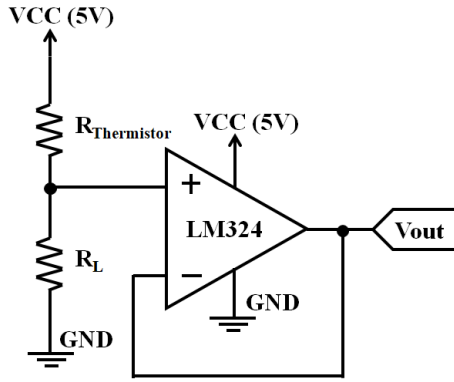


Figure 53 – Flowchart of the protocol defined for the tactile sensors comparison.

5.1.1 Voltage to temperature conversion

Thermistors are temperature-sensing elements that display large changes in resistance in proportion to small changes in temperature. Unlike Resistance Temperature Detectors (RTDs), which are made of metal, Negative Temperature Coefficient (NTC) thermistors are generally made of ceramics or polymers [105]. Depending on the material that composes the thermistors higher temperature sensitivity coefficients can be achieved. Despite thermistors are slightly less precise than RTDs they provide a faster, stable and accurate response [106, 107]. In addition, their cost is lowered by the lack of signal conditioning circuits, which are often needed when dealing with RTDs [105]. For this reason, for a simple voltage-to-temperature conversion, the thermistor is connected to a measuring resistor in a voltage divider topology, which in turn is connected to a voltage follower, as illustrated in Figure 54. The voltage follower provides electrical impedance transformation from one circuit to another thus preventing the signal source from being affected by any currents that the load may produce.



$$V_{out}(V) = \frac{R_L V_{CC}}{R_L + R_{Thermistor}} \quad (34)$$

Figure 54 – Electronic circuit used to acquire the voltage across the thermistor.

Since the resistance of the NTC thermistor, $R_{Thermistor}$, decreases with increasing temperature, according to equation (34) the output voltage should increase. The load resistance, R_L , is chosen to ensure that the output voltage, V_{out} , is within the limits of the power supply, V_{CC} , being input to the Op Amp to avoid saturation (near the rail values). Thus, if the output voltage is defined to be at minimum 1.5V for the resistance value of the thermistor at reference temperature of 25°C, then R_L , can be obtained using equation (34).

$$R_L = \frac{V_{out} R_{Thermistor}}{V_{CC} - V_{out}} = \frac{1.5V \times 22k\Omega}{5V - 1.5V} = 8.25k\Omega \quad (34a)$$

Since the maximum temperature value measured at the tiles using the thermal camera, Figure 52 on section 5.1, was of 77.74 °C, consulting the datasheet [104], a resistance value of 3628.43Ω is expected for the thermistor. Thus, the maximum output voltage expected is given by equation (34b).

$$V_{out} = \frac{R_L V_{CC}}{R_L + R_{Thermistor}} = \frac{8.25k\Omega \times 5V}{8.25k\Omega + 3628.43\Omega} = 3.47V \quad (34b)$$

Considering that the output voltage varies between 1.5V and 3.47V, the operational amplifier can have a single supply configuration, meaning that the amplifier has only one supply rail (+Vcc). Therefore, the output voltage will only swing between +Vcc and the ground rail without any risk of saturating the output voltage.

To convert the output voltage to temperature, the relationship between the resistance and the temperature must be described in detail. The best approximation known to date is the Steinhart-Hart formula, published in 1968 [108] and described by equation (35).

$$\frac{1}{T} = A + B \ln(R) + C [\ln(R)]^3 \quad (35)$$

The above equation is a third-order approximation, where A , B and C are called the Steinhart-Hart parameters. These parameters are specified for each thermistor as a part of the datasheet. In addition, R is the thermistor resistance at a given temperature T . In the present case, the equation for the temperature being measured by the thermistor is given by equation (36).

$$T(K) = \frac{1}{A + B \ln(R_{Thermistor}/R_{25}) + C [\ln(R_{Thermistor}/R_{25})]^2 + D [\ln(R_{Thermistor}/R_{25})]^3} \quad (36)$$

, where $A = 3.35402 \times 10^{-3}$, $B = 2.912036 \times 10^{-4}$, $C = 4.048347 \times 10^{-6}$, $D = 1.702977 \times 10^{-7}$ and $R_{25}=22k\Omega$ is the resistance value at $T=25$ °C used as a reference. Thus, according to equation (36) the only changing variable is the thermistor resistance, $R_{Thermistor}$.

Concluding, measuring the voltage drop across the sensing resistor allows calculating the thermistor resistance. Using equation (34) combined with equation (36) allows correlating the voltage drop across the thermistor with the temperature at which the sensors are exposed. Consequently, the tactile sensors data can be acquired for the temperatures of interest.

5.1.2 Test comparison

To ensure that the weights positioning was the same in all tests, a 3D printed cup structure was attached to the top surface of the sensors, as depicted in Figure 55 – (b), ensuring the vertical position of the weights and the force orientation normal to the sensors surface in all tests. **The goal was to represent, as close to reality as possible, the operating conditions that the sensors will be submitted once integrated on the fingers of the gripper.**

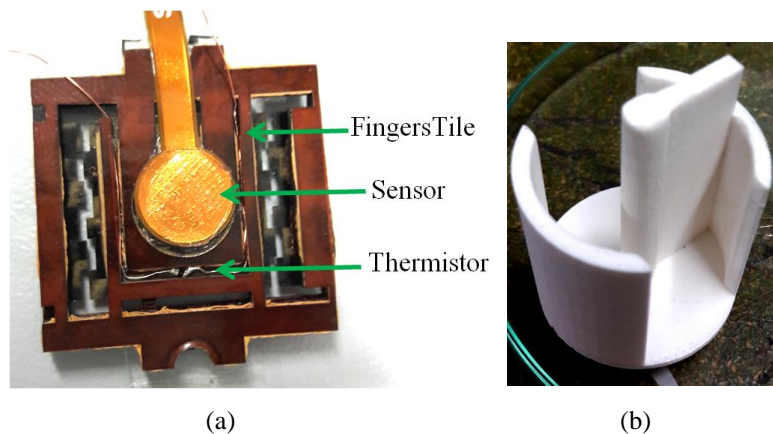


Figure 55 – Setup to test the temperature and loading effects on the capacitive sensors. The sensor is placed on top of a tile structure with the same glass fiber structure as the fingers and a thermistor is placed near the sensor to acquire the temperature (a). A 3D printed cup ensures that the weight positioning is kept constant during all tests (b).

Once the results are acquired, the mean and standard deviation for the three tests performed to both sensors at both temperatures are calculated. The results of the normalized sensors output are presented in Figure 56, where the red dashed line represents the data acquired at room temperature ($T=25\text{ }^{\circ}\text{C}$) and the blue line at $T=60\text{ }^{\circ}\text{C}$. In addition, in both figures the standard deviations represented by the error bars translate the repeatability achieved per temperature and loaded weight for each sensor.

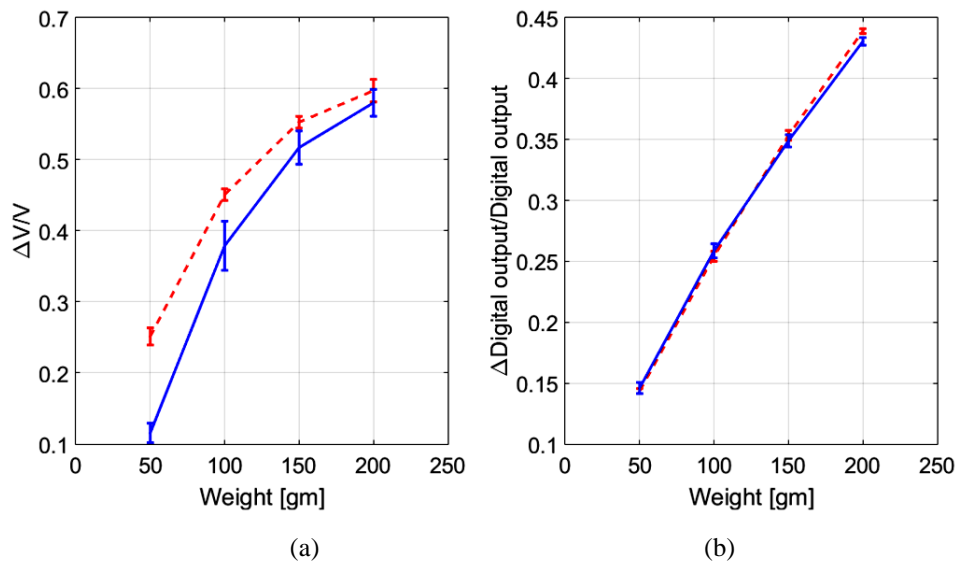


Figure 56 – Test results comparing FSR400 (a) and SingleTact capacitive sensors (b) under different loading and temperature conditions. Each test was performed three times. The red dashed curve represents the data acquired at $T=25\text{ }^{\circ}\text{C}$ while the blue lined curve represents $T=60\text{ }^{\circ}\text{C}$.

As can be observed in Figure 56 – (a) the **FSR400 sensors** present a **poor repeatability**, especially at higher temperatures, with a maximum standard deviation of 1.58%, and 3.45% of the full output range, respectively for $T=25\text{ }^{\circ}\text{C}$ and $T=60\text{ }^{\circ}\text{C}$. Concerning the **SingleTact** capacitive sensors, whose results are presented in Figure 56 – (b), the **repeatability is higher**, with maximum standard deviations of 0.42% at room temperature ($T=25\text{ }^{\circ}\text{C}$) and 0.59% at $T=60\text{ }^{\circ}\text{C}$ of the full output range, respectively. Furthermore, is possible to observe that **the temperature did not affect the linearity of the capacitive sensors response** (99.76% at $T=25\text{ }^{\circ}\text{C}$ and 99.58% at $T=60\text{ }^{\circ}\text{C}$).

Concluding, the results show that the **capacitive sensors from SingleTact are the best choice to integrate in the gripper, due to their repeatability under different loading and temperature conditions and compatibility with the layer-by-layer manufacturing process.**

5.2 Tactile sensor characterization

Above, the capacitive sensors were chosen as the most suitable for studying the contact forces between the objects being grasped and the gripper. Next follows their characterization with further detail to create **a model capable of predicting the amount of force being applied on top of the sensor**. The following protocol, depicted on Figure 57, was defined.

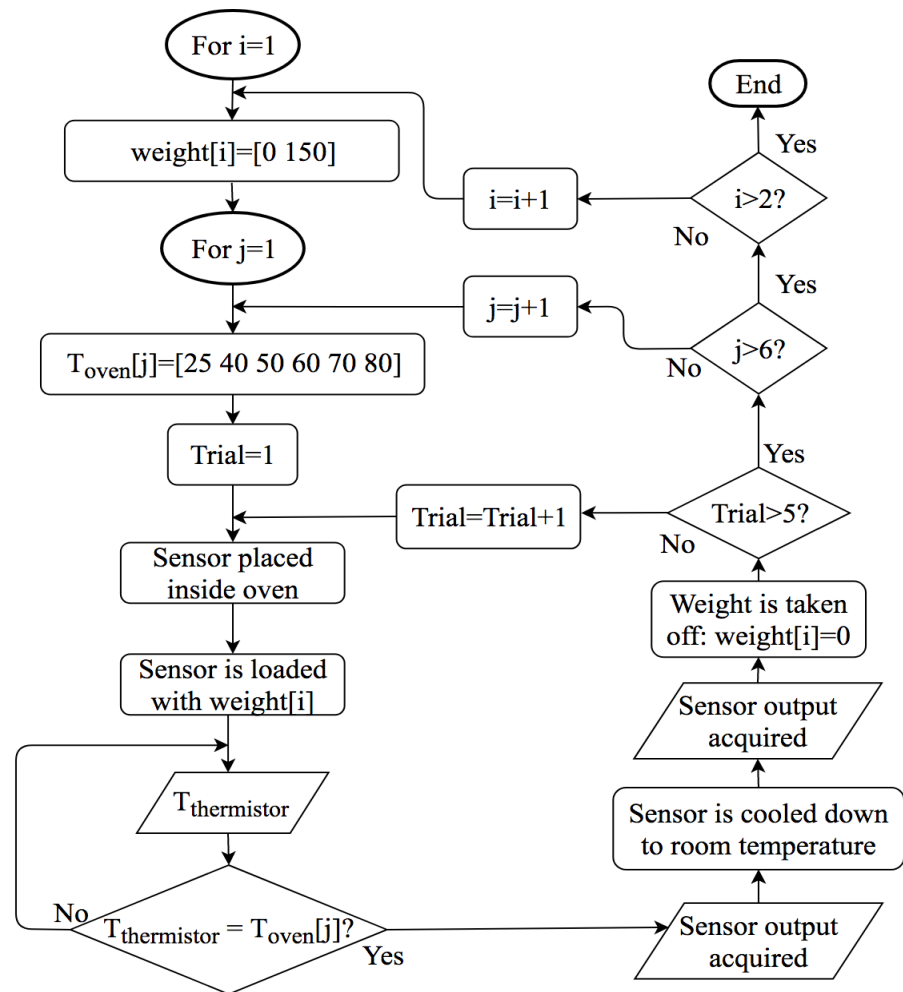


Figure 57 – Flowchart of the protocol defined for the tactile sensors characterization. For each weight and temperature, five trials were performed. During those five trials the sensor output during the heating and cooling process was acquired.

For each temperature five trials were performed and the mean and standard deviation calculated. In both tests the sensor output was acquired during the heating and cooling process to analyze the hysteresis effect on the sensor response. The experiment results are presented in Figure 58.

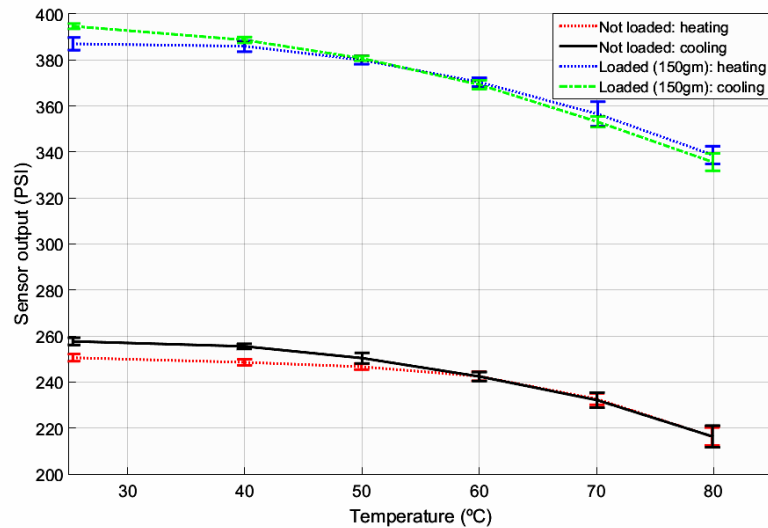


Figure 58 – Test results for the SingleTact capacitive sensors under different loading and temperature conditions. Each set consisted of five trials in which the heating and cooling processes were recorded.

The obtained results show that the sensor maintained a high repeatability, with a maximum error of 1.82% and 2.08% for heating and cooling processes, without any applied load. Under loading conditions the maximum error for the repeatability was 1.50% and 1.12% for the heating and cooling processes, respectively. Furthermore, it was observed a drift of 1.39% and 1.5% from the initial value for the two sets of tests under different loading conditions, after the sensors cooled down to room temperature, being the first reported drift correspondent to the case where no load was applied.

As seen in Figure 56 – (b), the sensor response to different loading conditions can be linearly approximated. Thus, the relation between the loaded weight and the sensor output for a given temperature can be determined, as shown in Figure 59.

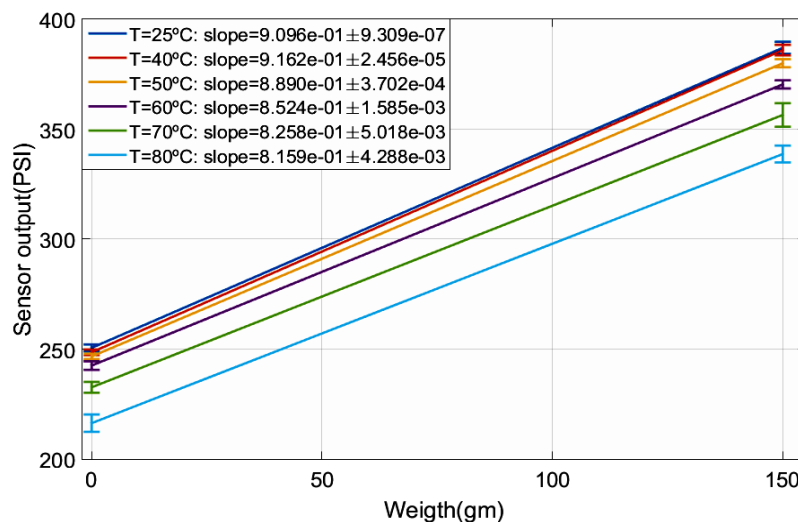


Figure 59 – Since in good approximation the sensor output is a linear function of the loaded weight, the relation between the weight and sensor output can be found for each temperature.

The loaded weight can be found using equations (37) and (38). Equation (37) describes the slope that correlates the output sensor with the loaded weight as a function of the temperature near the tactile sensor. Meanwhile, equation (38) is used to find the loaded weight as a function of the sensor output.

$$\text{slope} = aT^4 + bT^3 + cT^2 + dT + e \quad (37)$$

$$\text{weight}(\text{gm}) = \frac{1}{\text{slope}} (S_{\text{output}} - B_{\text{output}}) \quad (38)$$

, where $a=1.072\text{E-}9$, $b=-3.285\text{E-}6$, $c=5.331\text{E-}4$, $d=-2.485\text{E-}2$ and $e=1.440$. In equation (38) S_{output} and B_{output} represent, respectively, the sensor output when loaded at a given moment and the sensor baseline, given by the sensor output without any load at temperature T .

The obtained model was then validated performing a third test by subjecting different sensors to different temperatures and loading conditions. The results can be observed in Table VIII, in which the initial two rows represent the same sensor with different loading conditions at equal temperature. Third, fourth and fifth rows represent different sensors with the same loaded weight (150gm) but subject to different temperatures. Finally, the last two rows of data were obtained using the same sensor but varying the loading and temperature conditions. Thus, the effect of all variables (loading, temperature and sensor variability) can be tested for the model prediction.

TABLE VIII – Validation results from the model prediction.

T (°C)	B_{output} (PSI)	S_{output} (PSI)	Expected weight (gm)	δ Expected weight (gm)	Real weight (gm)
28.28	237.31	281.29	47.92	1.82	50
28.24	237.31	320.83	91.01	3.37	100
38.5	250.07	390.11	152.37	3.64	150
50.0	237.11	376.04	156.43	4.43	150
64.75	242.17	368.4	150.56	5.39	150
32.56	232.45	275.70	46.87	1.10	50
28.28	232.45	318.29	93.56	1.74	100

The uncertainty on the predicted weight, δ , was obtained using error propagation [109]. The error propagation takes into account the standard deviation of the temperature and sensor output obtained during the tests, as described by equation (39).

$$\delta \text{weight}(\text{gm}) = \text{weight} \sqrt{\left(\frac{\delta \text{slope}}{\text{slope}}\right)^2 + \left(\frac{\delta(S_{\text{output}} - B_{\text{output}})}{S_{\text{output}} - B_{\text{output}}}\right)^2} \quad (39)$$

The results show a maximum error of 5.92gm between the predicted and the real weight, which represents an uncertainty of 0.058N on the contact forces being calculated using the model equations.

5.3 Tactile sensors integration

In order to integrate the tactile sensor in the tiles of the fingers, a shaped-column structure is manufactured. The structure is composed by alternated glass fiber and polyimide bonding layers. Thus, thanks to the unique layer-by-layer manufacturing process the height of the support column can be adjusted according to equation (40) for the sensors to detect a minimum radius of curvature of an object, as illustrated in Figure 60 – (a).

$$\begin{cases} R \sin \theta = d \\ R(1 - \cos \theta) = h \end{cases} \Rightarrow R(\text{mm}) = \frac{d}{\sin(2 \arctan(h/d))} = 4.45 \text{mm} \quad (40)$$

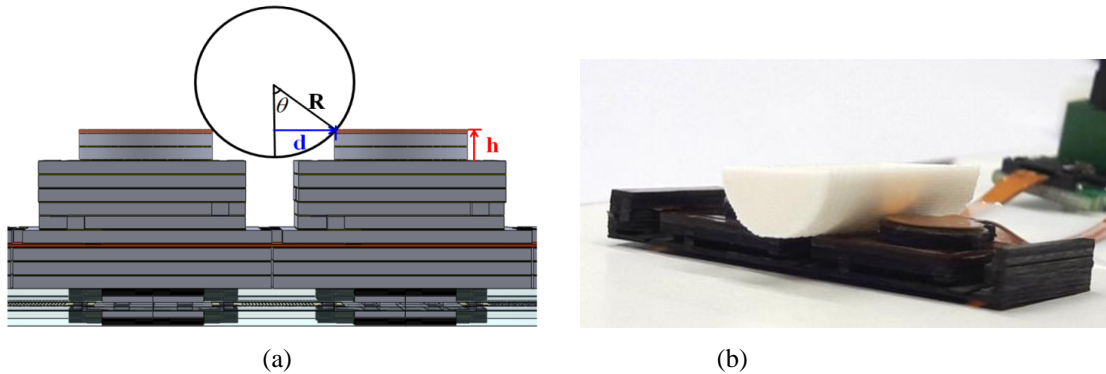


Figure 60 – Minimum radius detected by the contact sensors. The left figure, (a), represents the schematic with the dimensions for the test performed in the right figure, (b).

, where R is the radius of curvature of the object, d the distance from the center of the object to the tactile sensor edge, h the height of the tactile sensor support and θ the angle from the center of the object to the edge of the sensor, as illustrated in Figure 60 – (a).

The hypothesis was then tested by placing a three 3D printed half cylinder with 4, 4.45 and 5mm radius curvature on top of the sensor, as illustrated in Figure 60 – (b), and observing if the sensor was able to detect the object being placed on top of it. Results showed that the minimum radius curvature detected by two consecutive sensors was of 5mm.

In addition to the sensors integration, thermistors were also placed on the fingers tiles, as shown in Figure 61.

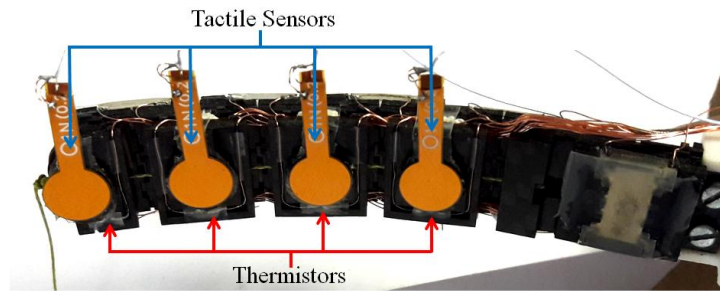


Figure 61 – Final structure of the tendon-driven robogami under-actuated finger. Four tactile sensors and thermistors were placed at the tiles of each finger.

The tactile sensors communicate with a Teensy board 3.6 using a I^2C protocol. Thus, the sensors act as slaves while the Teensy board as a master. In an I^2C bus two signals are required, the SCL (clock signal) and the SDA (data signal), as shown in Figure 62. The clock signal is always generated by the bus master, who initiates the communication by leaving the SCL high and pulling the SDA low as a start bit. As a consequence, all slaves are put on notice that a transmission is about to start. The master then sends the address of the slave it wants to communicate with to every slave connected to it. Next, each slave compares the sent address with its own, sending a low voltage acknowledge bit (ACK) back to the master if the address matches. The SCL is pulled low and the SDA sets the first data bit level while keeping the SCL low. At this point the data begins being transmitted. The data is sampled when the SCL rises for the first bit. The master will continue to generate clock pulses at a regular interval and the data will be placed on the SDA by the slave every time a pulse is generated by the clock. The final bit is followed by a clock pulse, during which SDA is pulled low in preparation for the stop bit. Finally, the stop bit is signaled when SCL rises, followed by SDA rising, thus terminating the communication [110]–[112].

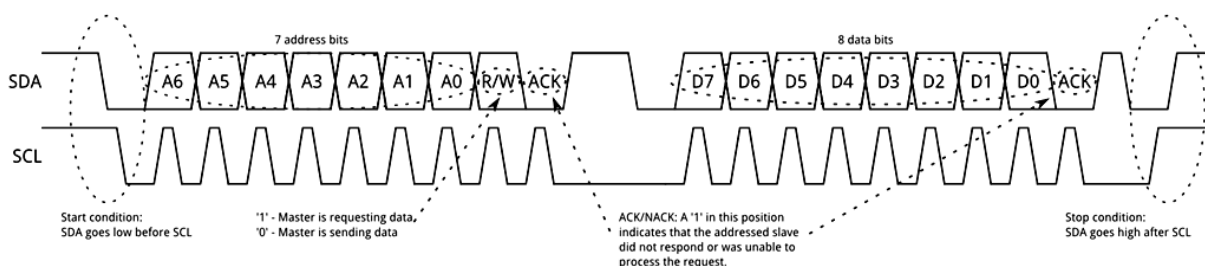


Figure 62 – Data Frame of an I^2C communication [112].

5.4 Thermistors integration

To integrate the thermistors, an adaption of the circuit presented in Figure 54 was made. Since **each finger possesses 4 thermistors**, it is required a solution to read 8 thermistor voltages while minimizing the number of required pins to read it. A multiplexer offers the advantage of minimizing the number of required input pins on the Teensy board. Thus, a multiplexer with 8 inputs and one output was used, 74HC4051 [113].

A multiplexer is a device that selects one of several analogue or digital input signals and forwards the selected input into a single output [114]. This way, a single input signal (output from the multiplexer) can be connected to the Teensy board, economizing connections over a single channel.

The selection of each channel is accomplished by the digital value assigned for the selector wires. Depending on the number of input channels needed, n , the number of selector wires also varies as an $\log_2(n)$ function. So, if the system needs to read eight input signals, eight input channels on the multiplexer are needed, which requires three selector wires (S0 to S2). Logic Table IX shows how pins are connected to select each of the input channels.

TABLE IX – 74HC4051 Logic Table.

\bar{E}	S2	S1	S0	I/O Connected to A
L	L	L	L	A0
L	L	L	H	A1
L	L	H	L	A2
L	L	H	H	A3
L	H	L	L	A4
L	H	L	H	A5
L	H	H	L	A6
L	H	H	H	A7
H	X	X	X	None

Since the multiplexer is powered at 5V, “L”, for “low” is any voltage between 0 and 2V, while “H”, for “high”, is any voltage between 3 and 5V [115]. Finally, to enable the multiplexer, the enable pin (E), must be set to low. The circuit used to determine the temperature near the tactile sensors is presented in Figure 63.

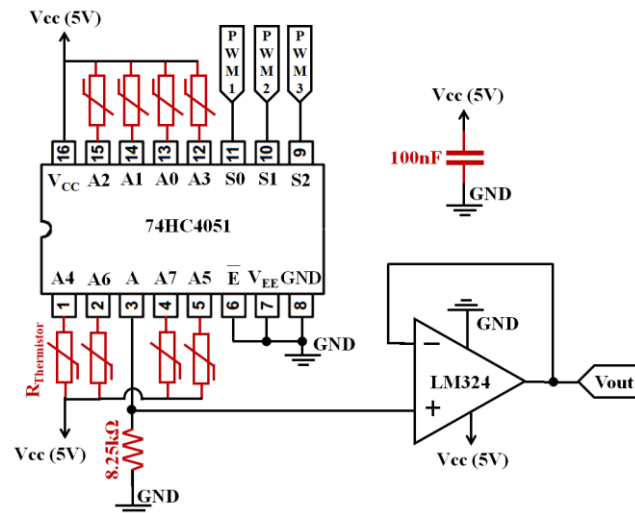


Figure 63 – Multiplexer circuit with voltage follower to measure the voltage drop across each thermistor.

At this moment, the fingers from the gripper are fully assembled and a linear motor, L16-P by Actuonix [116] with a designed and 3D printed motor house are attached to the manufactured fingers, completing the tendon-driven robogami under-actuated gripper, as shown in Figure 64.

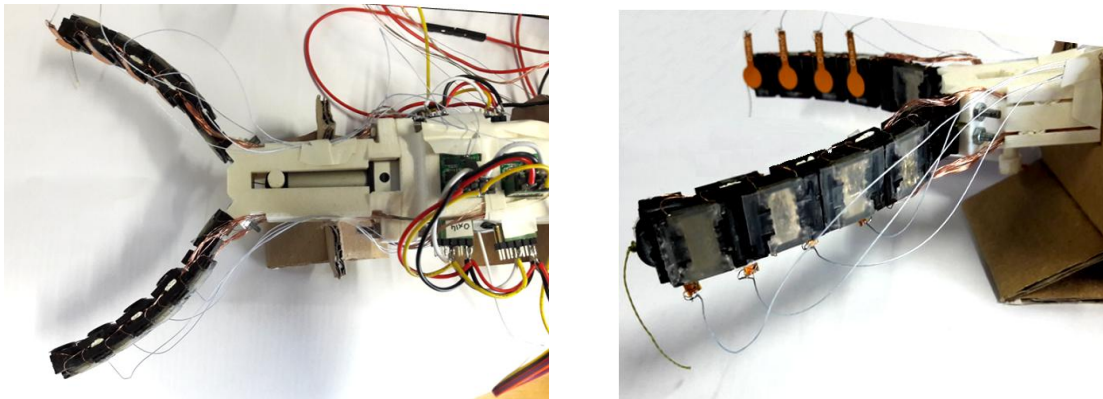


Figure 64 – Tendon-driven robogami under-actuated gripper with adjustable stiffness joints and tactile sensing.

5.5 Study of effective grasps configurations

The versatility of an under-actuated gripper depends on its capacity to adapt to the tasks being performed. One of the main advantages presented by under-actuated grippers is their ability to conform to the shape of different objects. Fingers shape conformity to an object is especially advantageous when **heavy and large objects** need to be lifted, since it requires a larger amount of force to be exerted on the object. Thus, enveloping the object in a so-called **power grasp** [2, 43, 117] allows securing the object. However, for **smaller and fragile objects**, enveloping the object is not the best solution towards grasping it, since shape

conformity can lead to instabilities on the performed grasp, resulting in the ejection or slipping motion of the object [21, 52, 54]. In such cases, a **precision grasp** configuration allows grasping an object only by the distal phalanges [5, 117].

5.5.1 Adjustable grasp modes of operation

Depending on the size and shape of the object, different configurations for the fingers of the gripper can be assigned by modulating the stiffness of the ASL.

In the **power grasp mode**, the gripper secures the object between the fingers tips and the base. To perform it, **joints 2-5 are activated** at their most compliant state, as shown in Figure 65 – a). Thus, for larger objects, the overall compliance and conformity of the fingers allows them to conform to the shape of the object and envelop it.

The second grasp mode of the gripper studied is the **precision grasp** of objects between the finger tips. In this case, **only joints 2 and 3 are activated** at their most compliant state, as presented in Figure 65 – b). Since less joints are active a larger displacement and small orientation of the tip occurs and so, the orientation of the gripper has to be adjusted based on the size of the object to avoid losing grasping stability.

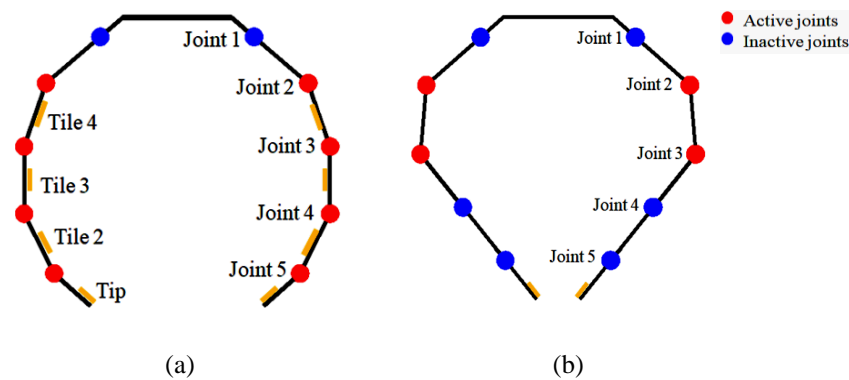


Figure 65 – Adjustable modes of operation are accomplished by adjusting the ASLs stiffness. A **power grasp mode** is achieved by activating joints 2-5 (a), while a **precision grasp mode** is achieved by activating only joints 2 and 3 (b).

Finally, the compliance of the tendon-driven robogami under-actuated finger can be significantly increased by activating the first joint, as it was presented by Firouzeh, A. *et al* [2]. The **increased compliance** of the finger is desired in **grasping soft and delicate objects** since the gripper does not apply large contact forces in this mode, as demonstrated in Figure 66. The increased compliance of the finger is achieved by activating the base joint, as depicted in Figure 66 – (b). Thus, the contact force is limited since the base joint automatically adjusts itself, providing inherent softness. On the other hand, if the base joint is

set on its stiff mode, the lack of compliance of the gripper leads to the deformation of the foam being grasped, as shown in Figure 66 – (a).

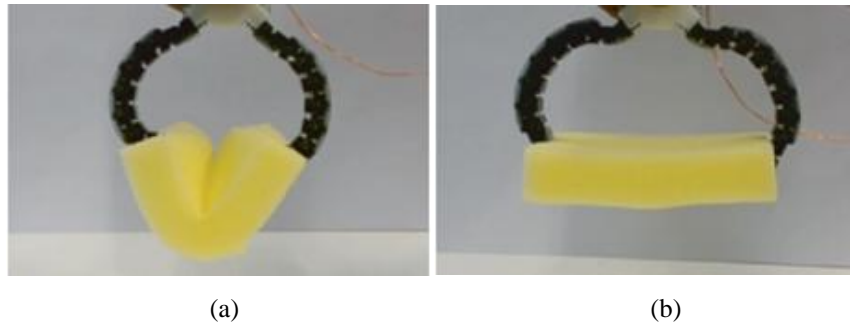


Figure 66 – Grasp of foam with different stiffness settings. If the base compliance is stiff, (a), the gripper applies a large force, deforming the foam. However, if the compliance at the base is soft, the contact force is limited and when the object is contacted, the base joint adjusts itself, (b) [2].

5.5.2 Effective grasp configurations results

The study of effective grasp configurations is initiated by **simulating the free motion of the tendon-driven robogami under-actuated gripper when there is not an object to be grasped**. Using the model equations (10) and (19) provided in section 3.2, a simulation software script, whose pseudo-code is presented in the table below, was developed to calculate the best configuration.

TABLE X – Pseudo-code for simulating the free motion of the tendon-driven robogami under-actuated gripper

Input variables:	Number of joints, n
	ASLs temperature, $ASL Temp$
	Total tendon displacement, X_{total}
	ASLs temperature, $ASLTemp$
Output variables:	Joints angle, θ
	Tip position in the x and y direction, $posEndX$ and $posEndY$, respectively
Constants	Length of the link, l
	Gap between tiles, g
	Tendon distance from the neutral plane, b
	Distance from the neutral plane to the ASL, h
	ASL thickness, t
	Maximum tendon tension, $tendonMax$
Joints limit, θ_{limit}	

The initial conditions to solve the problem are defined. Initially the angle of the joints, the tendon displacement and the tendon tension are zero.

```
 $\theta(1:n)=0;$ 
tendonD=0;
tendonT=0;
```

Then, while the tendon tension is lower than the maximum tendon tension and the tendon displacement does not reach the total displacement the problem of finding the right configuration is solved for a given tendon displacement.

1. The upper and lower boundaries for the joints angle and tendon tension are defined.
2. The problem is defined by calling an auxiliary function to solve equations (10) and (19), with given options (solver, function tolerance, maximum number of function evaluations and maximum number of iterations) and initial conditions.
3. The problem returns the joints angle and tendon tension and calculates the position of each tile using

```
WHILE (tendonT < tendonMax & tendonD < Xtotal)
{
    Upperlim=[  $\theta_{limit}$  ; tendonMax];
    Lowerlim=[  $\theta$ ; tendonT];

    x0=[ $\theta$ ; tendonT];
    options=(@lsqnonlin, FunTol, MaxFunEval,
    MaxIter);
    fun=@Aux
    problem=(lsqnonlin, fun,x0, Upperlim, Lowerlim,
    options);

    [solutions]=solve(problem);

     $\theta$ =solutions(1:n);
    tendonT=solutions(n+1);
    x0=[ $\theta$ ; tendonT];

    X(1)=0; Y(1)=0
    FOR i=1
        X(i+1)=X(i)+l(i)*cos(sum( $\theta(1:n)$ ));
        Y(i+1)=Y(i)-l(i)*sin(sum( $\theta(1:n)$ ));
    END

    tendonD=tendonD+constant;
```

direct kinematics. }

END

4. The initial conditions are updated based on the new solutions.
5. The tendon displacement is incremented by a constant value.

The auxiliary function is responsible for finding the minimum error that fits the problem to be solved. Thus, *lsqnonlin* starts at the initial point x_0 and finds the optimal solution for the tendon tension and the angle of the joints, returning an array of those values corresponding to the minimum found.

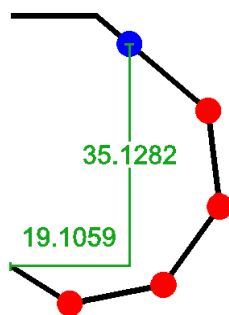
AUX: *solutions=solve(problem)*

$$F_t^T T - f^T J - \left(h + \frac{t_{ASL}}{2} \right)^2 ((K_{ASL} \sin(\theta))^T = 0$$

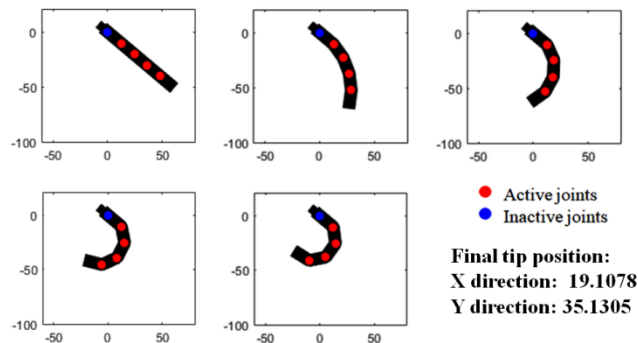
$$X_{total} - \sum_{j=1}^n X_i = 0$$

END

Using the initial designed dimensions for the length of the links and the joints limit, a CAD software designed prediction was made to compare with the simulated results, Figure 67 – (a) and (c). The simulation was performed for both **power and precision grasps** and the results are illustrated in Figure 67 – (b) and (d), respectively.



(a)



(b)

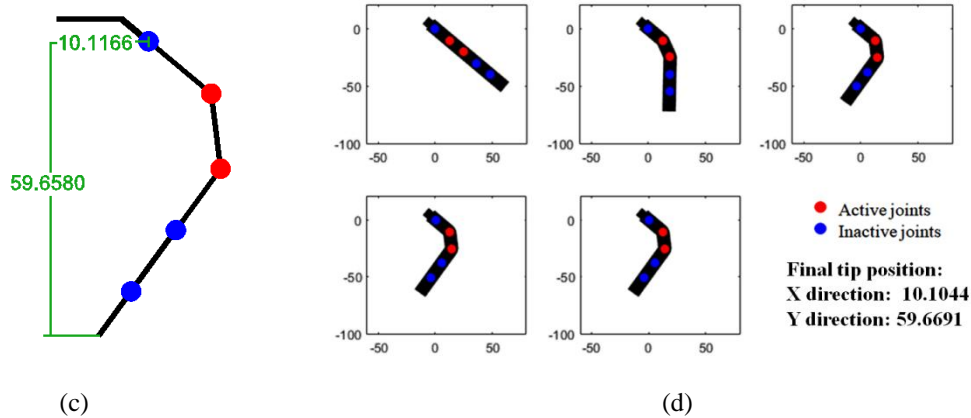


Figure 67 – Model simulations results for **power**, (b), and **precision grasps**, (d). The results are compared to the expected configuration (a) and (c).

The simulation results show that the model can accurately predict the configuration of the fingers with a maximum error of 0.12%. Simulations with grasping objects were not performed due to the difficulty of modeling friction forces.

In order to develop a control strategy for the gripper based on the feedback provided by tactile sensors, it is necessary to study effective grasp configurations and define thresholds to a general sized object, as it was also described in [23]. To perform the tests that compose this study, the following strategy, illustrated in Figure 68, was used:

- 1) The selected heaters thermally activate the SMP layers to adjust the stiffness of the desired ASLs. This activation occurs during 120s to ensure that the SMP layers are at their elastic state. Since the variability of the heaters and SMP thickness is approximately the same for all ASLs, thanks to the cleanroom manufacturing process, it is expected that the joints stiffness is approximately equal for the activated joints.
- 2) Once 120s have been passed, the values measured using the contact sensors and thermistors placed at the tiles of the finger provide a baseline for the contact force to be calculated.
- 3) The linear motor actuator starts pulling the tendon at a constant rate and consequently the bending motion of the joints occurs. The contact forces are acquired and calculated in real time.
- 4) Once the motor reaches a pre-defined position (to assure that it does not damage permanently the fingers in contact with the object) the motor stops pulling, acquiring the contact forces at the maximum tendon tension.
- 5) Once the forces have been acquired, the motor releases the wire, the fingers return to their preset position and the object being grasped is loosened.

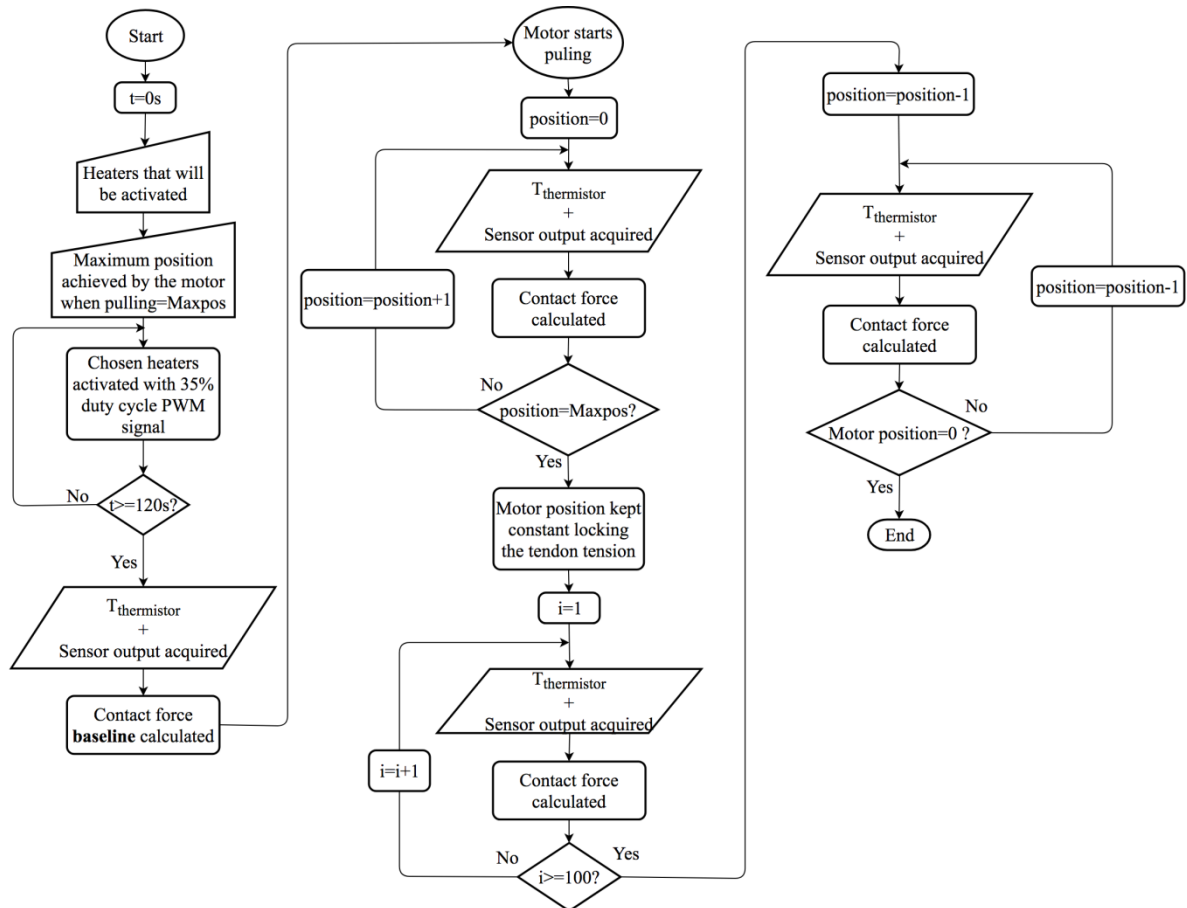
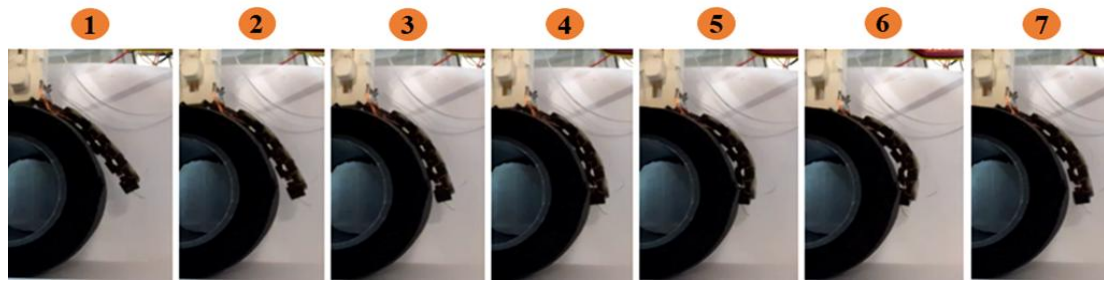


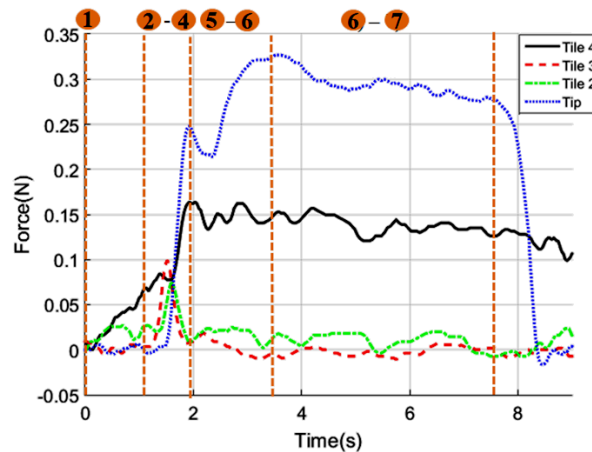
Figure 68 – Flowchart for studying the contact forces with different grasp configurations.

To understand how **power grasp** allows grasping objects by enveloping them, Figure 69 depicts the grasping phase of an object recorded by a camera and the corresponding signals from the contact sensors. First, the **gripper is placed on top of the object** (point 1). Then, after **modulating the joints stiffness** to achieve the configuration shown in Figure 67 – (a), the **tendon is pulled** and consequently the active joints start moving, leading the **fingers to conform to the object shape** from the base to the tip (points 2 – 4). The **continuously increasing tendon displacement** causes the tiles at the **middle joints to lose contact** with the object (points 5 – 6). However, the **contact forces** at the tip and near the base of the gripper (Tile 4) have **increased** by a factor of 4 and 2, respectively, compared to the point where all tiles were in contact with the object. This result shows that **losing contact points does not mean a decrement on grasping quality**. One can easily observe that the object is still locked inside the gripper. In fact, a higher amount of contact force, compared to when all tiles were in contact with the object, was recorded. The main question would be to **determine what is preferable in terms of grasping quality: higher number of contact points with lower contact forces per point or vice-versa**. According to [24], the number of contact points should be maximized to improve the ability to contact with unknown surfaces, while

tactile signals provide the necessary feedback to guide the fingers to actively comply to the sensed shape.



(a)



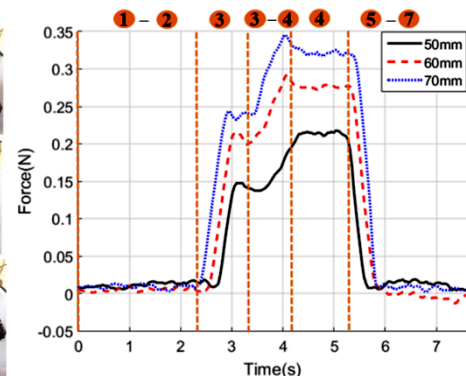
(b)

Figure 69 – **Power grasp** allows lifting heavier and larger objects by enveloping them between the robotic fingers (a). As a result, contact forces increase from the base to the tip of the finger. The continuously increasing tendon displacement increases the contact forces but at the cost of losing two contact points (b).

Concerning the **precision grasp**, the contact forces between the gripper and different sized objects were studied. The objects sizes vary from 50mm, 60mm and 70mm diameter (top to bottom snapshots of Figure 70).



(a)



(b)

Figure 70 – **Precision grasp modes** allows handling smaller and delicate objects by grasping them between the distal phalanxes (a). Objects with 50mm (black curve), 60mm (red dashed curve) and 70mm diameter (blue curve) were grasped and their contact forces acquired (b).

By analyzing the data provided by the sensors and the snapshots it is possible to observe that the initial contact with the objects starts at point 3. From that point on, the **increasing tendon displacement leads to an increment on the contact forces**, as observed in points 3-4 in Figure 70 – (a) and (b). Thus, since for **larger object** the initial **contact is initiated sooner**, for those objects **higher contact forces** are achieved, as observed in point 4 in Figure 70 – (a) and (b). However, **if the object is not properly grasped** in its initial phase of contact, the continuous **increase of output force could lead to the object ejection**. Therefore, a **compromise between the output contact force and the object** size and weight needs to be determined to avoid such cases. Hence the **importance of tactile sensors to improve and ensure secure and stable grasp**. If the object diameter is such that the tips of the fingers grasp the object at its upper part, the pinch motion will cause the object to **slip if the contact force is not enough** to grasp it or ultimately **ejects it**, if the **contact forces are too high**. Another case happens if the **weight of the object is higher than the forces** capable of handling the object. In such case, the force due to the weight loaded will be higher than the tendon tension to keep the active ASLs at a fixed position, **causing the object to fall**, as shown in Figure 71.

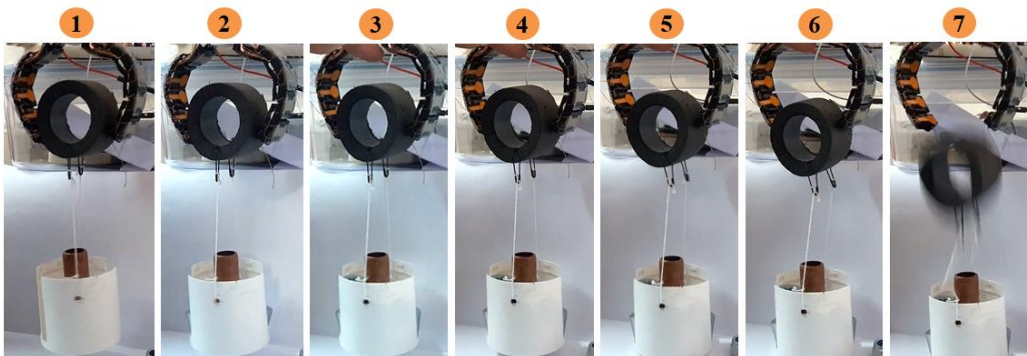


Figure 71 –Precision grasp of 50mm cylinder. Initially the gripper was able to handle the weight attached to the object (1). A 32gm weight was added in (point 2) and the gripper kept the object in position. At point 3 a new 32gm weight was added. From that point the gripper was not able to secure the object, causing it to fall.

Concluding, in this chapter the **importance of integrating tactile sensing systems to understand the interaction forces between the gripper and the objects was demonstrated**. Ultimately, the **integration of tactile systems can improve grasping quality while acting as safety complements** to the inherent softness that characterizes under-actuated grippers.

CHAPTER 6

CONCLUSION AND FUTURE WORK

6.1 Conclusion

The worked carried out during this past year is the next step of an **ongoing research to study effective grasps configurations using a tendon-driven robogami under-actuated gripper with adjustable stiffness joints and tactile sensing**. Such study is duly justified due to scientific works that show the ejection and slipping motion of different objects being grasped. Thus, the development of such gripper serves as a basis for future developments where the stiffness of the joints can be controlled and automatically adjusted according to the feedback provided by tactile sensors, improving grasps quality and ensuring safer interactions between the gripper and the surrounding environment.

The **main contributions** to knowledge of this research are divided in two parts: the technical and scientific contributions. The **technical contribution** is related to the **manufacturing process of the stretchable heaters using cleanroom techniques** to decrease the production costs while decreasing the heaters variability and achieving higher control on the designed features. Furthermore, the **integration of tactile sensors** in this version of the gripper is innovative compared to previous versions. Concerning the **scientific contribution**, this one is related to the **initiation of effective grasps configuration study using tactile sensors**. In this study, the grasping phase of an object, using a power grasp configuration, and the contact forces for different sized objects, using precision grasp, were recorded. Hence, the **importance of tactile sensors integration on under-actuated grippers was demonstrated to improve grasp configurations and consequently the grasping quality**.

The work herein presented included in a **first stage an extensive literature review** of the most important works related to under-actuated grippers and their evolution, from simple to complex designs, where adjustable compliance mechanisms and sensorial systems have been introduced to improve the versatility of the gripper when performing different tasks. Such review allowed **understanding and realizing what has already been done in the under-actuation robotic field**, with special focus on soft grippers, and **identifying problems and aspects to improve** on under-actuated robotic grippers.

During this research a **tendon-driven robogami under-actuated gripper with adjustable stiffness joints and tactile sensing was manufactured**. On a **first phase**, the tendon-driven robogami under-actuated **gripper structure was manufactured through a unique layer-by-**

layer manufacturing process. Such process allows integrating multiple functional layers to achieve the desired versatility to perform different tasks. Thus, the robogami platform makes the manufacturing process scalable and customizable. Then, in a **second phase**, an **adjustable stiffness layer** mainly composed by a stretchable that thermally activates an SMP layer to adjust its stiffness **was manufactured and embedded in the finger structure.** The **stretchable heater** was **manufactured using clean room techniques**, which allowed accomplishing a higher control on the manufactured structure. As a result of this process, several heaters were manufactured on a single batch, allowing reducing the variability between them, as it was then demonstrated as a result of their characterization. **Finally**, in order to study effective grasps configurations a **tactile sensing system** needed to be **integrated** as well. Thus, in a **third phase**, **three tactile sensors were compared** based on their repeatable response under different loading and temperature conditions and ease of integration. **The selected tactile sensor was then integrated onto the tendon-driven robogami under-actuated gripper.** Once the gripper was fully assembled, **two different grasps were studied while grasping different objects, a power and a precision grasp.** To perform both configurations the **joints stiffness was modulated by activating different ASLs.** The ASL activation is achieved by **adjusting its stiffness** accordingly. Concluding, **the study showed the importance of integrating tactile sensors to understand the interaction forces between the gripper and the object.**

The work herein presented enabled to answer the research questions outlined in the introduction section.

RQ1: “Is it possible to produce a tendon-driven robogami under-actuated gripper with adjustable modes of operation and integrated tactile sensing using fast and low-costs manufacturing processes?”. The robogami platform is a planar and foldable robotic platform that uses precise fabrication methods using a UV laser to micro machine quasi 2-D layers that are assembled together using heat pressing processes. Such fast and low-cost manufacturing process allows reducing the overall cost production of the gripper. Moreover, the adjustable stiffness layer is manufactured using the same platform with the exception of the stretchable heater that is manufactured using clean room techniques. Despite the clean room micromachining process is not a cheap process, the advantage of producing a batch with more than 20 heaters on a single run allows reducing the cost while maintaining the quality of the manufactured devices. In addition, the tactile sensors integrated are also compatible with layer-by-layer manufacturing process, and so their replacement is easily achieved.

RQ2: “Is the clean room manufacturing process of stretchable heaters advantageous?”. As it was presented in chapter 4.2 of this thesis, the manufacturing process of stretchable heaters using clean room micromachining techniques allows achieving a higher control of the designed features. However, the biggest advantage lies in the possibility of manufacturing several heaters in a single batch, resulting in a lower variability of the heaters resistance change due to temperature effects, as it was also tested and presented. Also, due to the high quality inherent to the clean room manufacturing process, the heaters present a highly repeatable response to temperature variation and mechanical deformation, which is highly desirable in order to avoid repeated calibrations.

RQ3: “Can the stretchable heaters be used as temperature sensors as well?”. As it was studied, the resistance change in the heater can occur as a result of two effects: mechanical deformation and temperature variation. The resistance of the heater demonstrated a repeatable behavior that was characterized when the temperature changed. However, when mechanically deformed it was not possible to ensure that only the mechanical deformation effect occurred. The reason is explained as follows: to measure the heater resistance, a PWM signal is input to the heater so that the current passing through the serpentine paths and the voltage across the heater can be measured, allowing to calculate its resistance. However, when inputting a PWM signal, the heater inherently starts heating and the temperature at which it stabilizes depends on this resistance value. When mechanically deforming the heater, its resistance changes as well, as observed in section 4.3.3. However, one of two cases might be occurring. First, when deformed, the resistance of the heater changes and hence the temperature at which the ASL is being activated changes as well. Second, when the ASL is bent, its surface exposed to the air is increased and so its temperature might consequently decrease, leading to a decreasing resistance value being measured. Thus, using a PWM signal to study the mechanical deformation effect is not the best option since it is not possible to isolate only the mechanical contribution. A proposed solution would be to measure the resistance using a multimeter, while bending the ASL inside an oven at constant temperature. Thus, the resistance variation would only be caused by the mechanical deformation since the ASL is always at the same temperature and there is not any signal being applied to the heater, causing its temperature to rise. However, despite the results obtained so far, show that the heater can only be used as a temperature sensor when the finger is at a fixed position and no deformation occurs, when the

mechanical deformation effect changes the resistance of the heater, the heater demonstrated a good resistance recovery after being deformed.

RQ4: “Can tactile sensors be used to improve grasping quality and ensure safer interactions between grippers and the surrounding environment?”. Despite some results were obtained, more tests must be performed to evaluate and correlate the grasping configurations with the contact forces measured by the integrated tactile sensors. However, it was possible to conclude that tactile sensors have an important role to understand the contact forces between the gripper and its surrounding environment and hence their feedback can be used to ensure secure and safer grasps.

6.2 Future work

The **main goal of the research team is the development of under-actuated grippers with adjustable stiffness joints capable of adapting to several objects being grasped**. However, several aspects can still be improved with the final goal of achieving robustness, autonomy and precision to grasp different objects. Thus, the next subsections provide insight on what still needs to be improved.

6.2.1 Adjustable stiffness layer improvement

One of the **major problems** on the presented version of the tendon-driven robogami under-actuated gripper **is the adjustable stiffness layer (ASL) robustness**. A **new integration method** of the ASL on the finger should be developed since the use of glue to attach it to the fingers makes the replacement of the damaged ASLs difficult. One possible solution is inspired in puzzle structures, making the **ASLs modular structures that can slide to fit the finger structure**, as shown in Figure 72. Thus, the ASL structure can be easily replaced on top of the fingers if damaged while still holding together to the finger when stretched.

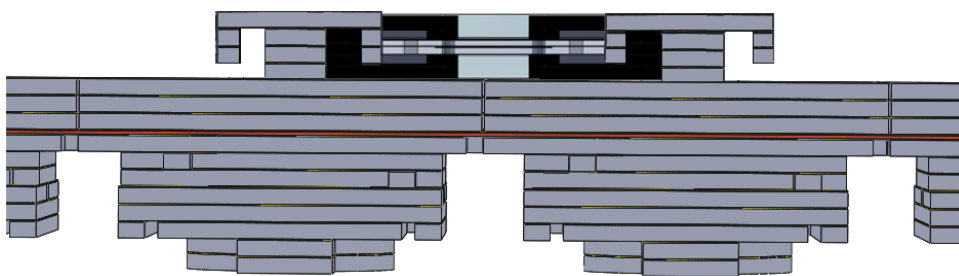


Figure 72 –Proposed design for future ASLs. The puzzle outer frame structure allows to easily replace the ASL if damaged.

6.2.2 Stretchable heaters improvements

Another problem found during this research is the heaters robustness, which should be improved to be able to handle more testing cycles. To do it so, the thickness of the stretchable heater should be increased and the number of serpentine paths reduced to still meet the power consumption requirements. Moreover, to overcome the problem of using the stretchable heaters as temperature sensors, double sided heaters could be produced to cancel the mechanical deformation effect. It is known that when deformed the serpentine path is partly in tension and partly in compression [67]. Thus, if the ASL structure consists of two heaters faced against each other in such way that one is the negative of the other, than the tension and compression parts of both heaters would cancel each other out, making the ASL structure rather insensitive to strain and only accountable for the temperature effect, as desired.

6.2.3 Effective grasps configurations

Finally, concerning the study of effective grasp configurations, future works include to specify more tests and validate them by comparing the simulated contact forces with experimental results. These simulations, with the proposed pseudo-code presented in Table XI could use the model described in section 3.2 of this thesis for calculating the contact forces.

TABLE XI – Pseudo-code for simulating the free motion of the tendon-driven robogami under-actuated gripper

Input variables:	Number of joints, n
	ASLs temperature, $ASL Temp$
	Total tendon displacement, X_{total}
Output variables:	ASLs temperature, $ASL Temp$
	Joint's angle, θ
Constants	Contact Forces, F
	Length of the link, l
	Gap between tiles, g
	Tendon distance from the neutral plane, b
	Distance from the neutral plane to the ASL, h
	ASL thickness, t
	Max tendon tension, $tendonMax$
	Joint's limit, θ_{limit}
Object size, $objdiam$	

The position of each link of the finger is calculated based on the points that defined them (X_i, Y_i) and (X_{i+1}, Y_{i+1}) , as shown in Figure 73.

$X(1)=0; Y(1)=0;$
 $\underline{FOR} i=1:n$
 $X(i + 1) = X(i) + l(i)\cos(\sum_{i=1}^n \theta_i)$
 $Y(i + 1) = Y(i) - l(i)\sin(\sum_{i=1}^n \theta_i)$
 \underline{END}

The distance from the middle of each link $(X_{contact}, Y_{contact})$ to the center of the object (C_x, C_y) is calculated and compared to the size of the object, r . If the distance, d , is equal or lower than the object size that means the finger is in contact with object.

$\underline{FOR} i=1:n$
 $X_{contact}(i + 1) = X(i) + \frac{l(i)}{2} \cos(\sum_{i=1}^n \theta_i)$
 $Y_{contact}(i + 1) = Y(i) - \frac{l(i)}{2} \sin(\sum_{i=1}^n \theta_i)$
 $d(i) = \sqrt{(X_{contact}(i) - C_x)^2 + (Y_{contact}(i) - C_y)^2}$
 \underline{END}
 $\underline{IF} d(i) \leq r$
Calculates contact force;
 \underline{ELSE}
 $F_{contact}(i)=0;$
 \underline{END}

To calculate the contact forces, the slope of each link is initially determined. Then, the slope normal to each link is calculated. The intersection between the line normal to each link that contacts the object boundary, i.e., which is at a distance equal to radius of the object is determined. Next, indentation of the finger, i.e., how much “inside” the object is the contact point of the finger, is found. Finally, the contact force considering the stiffness of the object, k_{indent} , is calculated

$\underline{FOR} i=1:n$
 $slope(i) = \frac{Y(i+1)-Y(i)}{X(i+1)-X(i)}$
 $slope2(i) = -\frac{1}{slope(i)}$
 $\left\{ \begin{array}{l} r = \sqrt{(X_{max}(i) - C_x)^2 + (Y_{max}(i) - C_y)^2} \\ Y_{max}(i) = slope2(i) * (X_{max}(i) - X_{contact}(i)) + Y_{contact}(i) \end{array} \right.$
 $ind(i) = \sqrt{(X_{max}(i) - X_{contact}(i))^2 + (Y_{max}(i) - Y_{contact}(i))^2}$
 $F_{contact}(i) = k_{indent} * indent(i)$
 \underline{END}

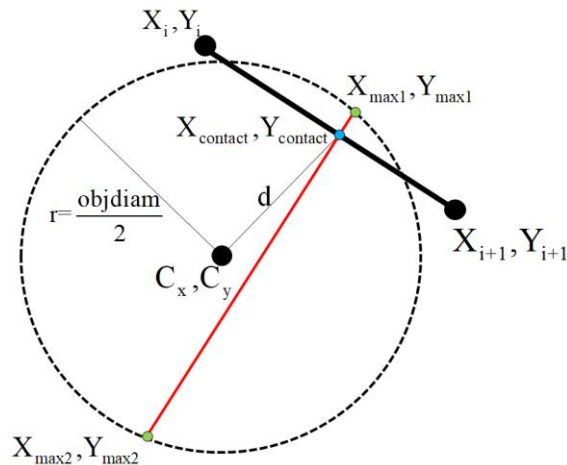


Figure 73 –Schematic showing how contact forces can be calculated on future simulations.

Concerning future experiments to study effective grasps configurations, the following ideal tests should be performed. For power grasps using simple-shaped objects, such as cylinders, the object size and weight would be the variables of interest. Thus, varying only the radius of curvature of the object and maintaining its weight constant, the grasping phase for different size objects can be studied. On the other hand, varying the weight of an object allows studying the amount of applied force capable of handling the objects without slipper events occurring. This last test would also be performed for precision grasps. As a consequence, the desired threshold that relates the contact force with the size of the object could be determined. Concluding, using the feedback provided by the contact sensors with the results obtained for the above mentioned tests, a control strategy could be put in practice to automatically adjust the gripper configuration, thus improving grasping quality and ensuring secure and safer grasps.

REFERENCES

- [1] F. L. Hammond, J. Weisz, A. A. De La Llera Kurth, P. K. Allen, and R. D. Howe, “Towards a design optimization method for reducing the mechanical complexity of underactuated robotic hands,” *Proc. - IEEE Int. Conf. Robot. Autom.*, pp. 2843–2850, 2012.
- [2] A. Firouzeh and J. Paik, “Grasp Mode and Compliance Control of an Underactuated Origami Gripper Using Adjustable Stiffness Joints,” *IEEE/ASME Trans. Mechatronics*, vol. 22, no. 5, pp. 2165–2173, 2017.
- [3] A. Firouzeh and J. Paik, “An under-actuated origami gripper with adjustable stiffness joints for multiple grasp modes,” 2017.
- [4] A. Firouzeh, M. Salerno, and J. Paik, “Stiffness Control with Shape Memory Polymer in Underactuated Robotic Origamis,” *IEEE Trans. Robot.*, vol. 33, no. 4, pp. 765–777, 2017.
- [5] L. Birglen, T. Laliberté, and C. Gosselin, *Underactuated Robotic Hands*, vol. 40. 2008.
- [6] A. Bicchi, “Hands for dexterous manipulation and robust grasping: A difficult road toward simplicity,” *IEEE Trans. Robot. Autom.*, vol. 16, no. 6, pp. 652–662, 2000.
- [7] S. Hirose and Y. Umetani, “The development of soft gripper for the versatile robot hand,” *Mech. Mach. Theory*, vol. 13, no. 3, pp. 351–359, 1978.
- [8] A. Rovetta, I. Franchetti, and P. Vicentini, “United States Patent (4351553),” vol. 96, no. 19, pp. 62–66, 1980.
- [9] J. Yang, E. P. Pitarch, K. Abdel-Malek, A. Patrick, and L. Lindkvist, “A multi-fingered hand prosthesis,” *Mech. Mach. Theory*, vol. 39, no. 6, pp. 555–581, 2004.
- [10] S. Groothuis, R. Carloni, and S. Stramigioli, “A Novel Variable Stiffness Mechanism Capable of an Infinite Stiffness Range and Unlimited Decoupled Output Motion,” *Actuators*, vol. 3, no. 2, pp. 107–123, 2014.
- [11] D. Aukes, B. Heyneman, V. Duchaine, and M. R. Cutkosky, “Varying spring preloads to select grasp strategies in an adaptive hand,” *IEEE Int. Conf. Intell. Robot. Syst.*, pp. 1373–1379, 2011.
- [12] J. Choi, S. Hong, W. Lee, S. Kang, and M. Kim, “A robot joint with variable stiffness using leaf springs,” *IEEE Trans. Robot.*, vol. 27, no. 2, pp. 229–238, 2011.
- [13] F. Lotti and G. Vassura, “A novel approach to mechanical design of articulated fingers for robotic hands,” *IEEE/RSJ Int. Conf. Intell. Robot. Syst.*, vol. 2, no. October, pp. 2–7, 2002.

- [14] W. Wang and S.-H. Ahn, "Shape Memory Alloy-Based Soft Gripper with Variable Stiffness for Compliant and Effective Grasping," *Soft Robot.*, 2017.
- [15] A. Firouzeh, M. Salerno, and J. Paik, "Soft pneumatic actuator with adjustable stiffness layers for Multi-DoF Actuation," *IEEE Int. Conf. Intell. Robot. Syst.*, vol. 2015–Decem, pp. 1117–1124, 2015.
- [16] W. Shan, T. Lu, and C. Majidi, "Soft-matter composites with electrically tunable elastic rigidity," *Smart Mater. Struct.*, vol. 22, no. 8, 2013.
- [17] A. M. Dollar and R. D. Howe, "A Robust Compliant Grasper via Shape Deposition Manufacturing," *IEEE/ASME Trans. Mechatronics*, vol. 11, no. 2, pp. 154–161, 2006.
- [18] J. Y. Nagase, S. Wakimoto, T. Satoh, N. Saga, and K. Suzumori, "Design of a variable-stiffness robotic hand using pneumatic soft rubber actuators," *Smart Mater. Struct.*, vol. 20, no. 10, 2011.
- [19] K. Takashima, K. Sugitani, N. Morimoto, S. Sakaguchi, T. Noritsugu, and T. Mukai, "Pneumatic artificial rubber muscle using shape-memory polymer sheet with embedded electrical heating wire," *Smart Mater. Struct.*, vol. 23, no. 12, 2014.
- [20] S. Hong *et al.*, "Highly Stretchable and Transparent Metal Nanowire Heater for Wearable Electronics Applications," *Adv. Mater.*, vol. 27, no. 32, pp. 4744–4751, 2015.
- [21] H. Tsutsui, Y. Murashima, N. Honma, and K. Akazawa, "Robot hand with soft tactile sensors and underactuated control," *Proc. Annu. Int. Conf. IEEE Eng. Med. Biol. Soc. EMBS*, pp. 4148–4151, 2013.
- [22] D. M. Aukes *et al.*, "Design and testing of a selectively compliant underactuated hand," *Int. J. Rob. Res.*, vol. 33, no. 5, pp. 721–735, 2014.
- [23] P. Akella, R. Siegwart, and M. Cutkosky, "Manipulation with soft fingers: contact force control," *Proceedings. 1991 IEEE Int. Conf. Robot. Autom.*, no. April, pp. 652–657, 1991.
- [24] N. Sommer and A. Billard, "Multi-contact haptic exploration and grasping with tactile sensors," *Rob. Auton. Syst.*, vol. 85, pp. 48–61, 2016.
- [25] R. Tedrake, "Fully-actuated vs Underactuated Systems," 2015. [Online]. Available: <http://underactuated.mit.edu/underactuated.html>.
- [26] L. Birglen and M. C. Gosselin, "Kinetostatic Analysis of Underactuated Fingers," vol. 20, no. 2, pp. 1–12, 2004.
- [27] T. Okada, "Computer Control Of Multijointed Finger System For Precise Object-Handling," *IEEE Trans. Syst. Man Cybern.*, vol. 12, no. 3, pp. 289–299, 1982.

-
- [28] J.K. Salisbury and J. Craig, “Articulated hands: Force control and kinematics issues,” *Int. J. Robot. Researh, Vol. 1, No. 1.*, pp. 4–17, 1982.
- [29] S. C. Jacobsen, E. K. Iversen, D. F. Knutti, R. T. Johnson, and K. B. Biggers, “Design of the Utah M.I.T. Dextrous Hand,” *Int. Conf. Robot. Autom.*, pp. 1520–1532, 1986.
- [30] J. Butterfass, G. Hirzinger, S. Knoch, and H. Liu, “DLR’s multisensory articulated hand. I. Hard- and software architecture,” *Proceedings. 1998 IEEE Int. Conf. Robot. Autom. (Cat. No.98CH36146)*, vol. 3, pp. 2081–2086, 1998.
- [31] S. Haidacher *et al.*, “DLR hand II: hard- and software architecture for information processing,” *2003 IEEE Int. Conf. Robot. Autom. (Cat. No.03CH37422)*, vol. 1, pp. 684–689, 2003.
- [32] C. F. Ruoff and J. K. J. Salisbury, “United States Patent (4921293),” no. 19, 1990.
- [33] H. L. P. Meusel and J. B. G. Hirzinger, “DLR ’ s multisensory articulated Hand Part II : The Parallel Torque / Position Control System,” no. May, pp. 2087–2093, 1998.
- [34] C. Y. Brown and H. H. Asada, “Inter-finger coordination and postural synergies in robot hands via mechanical implementation of principal components analysis,” *IEEE Int. Conf. Intell. Robot. Syst.*, pp. 2877–2882, 2007.
- [35] P. Y. Chua, T. Ilschner, and D. G. Caldwell, “Robotic manipulation of food products – a review,” 2006.
- [36] M. Salerno, K. Zhang, A. Menciassi, and J. S. Dai, “A Novel 4-DOF Origami Grasper With an SMA-Actuation System for Minimally Invasive Surgery,” *IEEE Trans. Robot.*, vol. 32, no. 3, pp. 484–498, 2016.
- [37] M. C. Carrozza, B. Massa, S. Micera, R. Lazzarini, M. Zecca, and P. Dario, “The Development of a Novel Prosthetic Hand—Ongoing Research and Preliminary Results,” vol. 7, no. 2, pp. 108–114, 2002.
- [38] S. Superiore, S. Anna, P. Sant, and A. Valdera, “Experimental analysis of the proprioceptive and exteroceptive sensors of an underactuated prosthetic hand,” 2004.
- [39] M. C. Carrozza *et al.*, “The SPRING Hand: Development of a Self-Adaptive Prosthesis for Restoring Natural Grasping,” *Auton. Robots*, vol. 16, no. 2, pp. 125–141, 2004.
- [40] D. M. Lane *et al.*, “AMADEUS: Advanced Manipulation for Deep Underwater Sampling,” *Robotics*, no. December, 1997.
- [41] N. Ulrich and V. Kumar, “Grasping using Fingers with coupled Joints,” *ASME Trends Dev. Mech.*, vol. 3, pp. 201–207, 1988.
- [42] B. Rubinger, M. Brousseau, J. Lymer, C. Gosselin, T. Laliberté, and J.-C. Piedboeuf, “A Novel Robotic Hand-SARAH For Operations on the International Space Station,”
-

- no. 1, pp. 1–8, 2002.
- [43] B. Gao, S. Yang, H. Jin, Y. Hu, X. Yang, and J. Zhang, “Design and Analysis of Underactuated Robotic Gripper with Adaptive Fingers for Objects Grasping Tasks,” pp. 987–992, 2016.
- [44] H. Dong, E. Asadi, C. Qiu, J. Dai, and I. M. Chen, “Geometric design optimization of an under-actuated tendon-driven robotic gripper,” *Robot. Comput. Integr. Manuf.*, vol. 50, no. September 2017, pp. 80–89, 2018.
- [45] M. A. McEvoy and N. Correll, “Thermoplastic variable stiffness composites with embedded, networked sensing, actuation, and control,” in *Journal of Composite Materials*, 2015, vol. 49, no. 15, pp. 1799–1808.
- [46] K. Takashima, N. Zhang, T. Mukai, and S. Guo, “Fundamental Study of a Position-keeping Module Using a Shape-memory Polymer,” *J. Robot. Soc. Japan*, vol. 28, no. 7, pp. 905–912, 2010.
- [47] Y. Yang, Y. Chen, Y. Wei, and Y. Li, “Novel Design and Three-Dimensional Printing of Variable Stiffness Robotic Grippers,” *J. Mech. Robot.*, vol. 8, no. 6, p. 061010, 2016.
- [48] C. Guo, L. Zhou, and J. Lv, “Effects of expandable graphite and modified ammonium polyphosphate on the flame-retardant and mechanical properties of wood flour-polypropylene composites,” *Polym. Polym. Compos.*, vol. 21, no. 7, pp. 449–456, 2013.
- [49] H. Koerner, G. Price, N. A. Pearce, M. Alexander, and R. A. Vaia, “Remotely actuated polymer nanocomposites - Stress-recovery of carbon-nanotube-filled thermoplastic elastomers,” *Nat. Mater.*, vol. 3, no. 2, pp. 115–120, 2004.
- [50] J. W. Cho, J. W. Kim, Y. C. Jung, and N. S. Goo, “Electroactive shape-memory polyurethane composites incorporating carbon nanotubes,” *Macromol. Rapid Commun.*, vol. 26, no. 5, pp. 412–416, 2005.
- [51] A. M. Schmidt, “Electromagnetic activation of shape memory polymer networks containing magnetic nanoparticles,” *Macromol. Rapid Commun.*, vol. 27, no. 14, pp. 1168–1172, 2006.
- [52] M. Stachowsky, T. Hummel, M. Moussa, and H. A. Abdullah, “A Slip Detection and Correction Strategy for Precision Robot Grasping,” *IEEE/ASME Trans. Mechatronics*, vol. 21, no. 5, pp. 2214–2226, 2016.
- [53] K. Weiss and H. Worn, “The working principle of resistive tactile sensor cells,” in *IEEE International Conference Mechatronics and Automation, 2005*, 2005, no. July,

- pp. 471–476.
- [54] Y. Xin *et al.*, “PVDF tactile sensors for detecting contact force and slip: A review,” *Ferroelectrics*, vol. 504, no. 1, pp. 31–45, 2016.
- [55] L. P. Jentoft, Y. Tenzer, D. Vogt, J. Liu, R. J. Wood, and R. D. Howe, “Flexible, stretchable tactile arrays from MEMS barometers,” *2013 16th Int. Conf. Adv. Robot. ICAR 2013*, 2013.
- [56] J. Li, J. Liang, X. Jian, W. Hu, J. Li, and Q. Pei, “A flexible and transparent thin film heater based on a silver nanowire/heat-resistant polymer composite,” *Macromol. Mater. Eng.*, vol. 299, no. 11, pp. 1403–1409, 2014.
- [57] S. Choi *et al.*, “Stretchable Heater Using Ligand-Exchanged Silver Nanowire Nanocomposite for Wearable Articular Thermotherapy,” *ACS Nano*, vol. 9, no. 6, pp. 6626–6633, 2015.
- [58] D. Kim *et al.*, “Transparent flexible heater based on hybrid of carbon nanotubes and silver nanowires,” *Carbon N. Y.*, vol. 63, pp. 530–536, 2013.
- [59] A. Y. Kim *et al.*, “Oxidation-resistant hybrid metal oxides/metal nanodots/silver nanowires for high performance flexible transparent heaters,” *Nanoscale*, vol. 8, no. 6, pp. 3307–3313, 2016.
- [60] D. Jung, D. Kim, K. H. Lee, L. J. Overzet, and G. S. Lee, “Transparent film heaters using multi-walled carbon nanotube sheets,” *Sensors Actuators, A Phys.*, vol. 199, pp. 176–180, 2013.
- [61] Y. H. Yoon *et al.*, “Transparent film heater using single-walled carbon nanotubes,” *Adv. Mater.*, vol. 19, no. 23, pp. 4284–4287, 2007.
- [62] R. Zhou, P. Li, Z. Fan, D. Du, and J. Ouyang, “Stretchable heaters with composites of an intrinsically conductive polymer, reduced graphene oxide and an elastomer for wearable thermotherapy,” *J. Mater. Chem. C*, vol. 5, no. 6, pp. 1544–1551, 2017.
- [63] D. Sui, Y. Huang, L. Huang, J. Liang, Y. Ma, and Y. Chen, “Flexible and transparent electrothermal film heaters based on graphene materials,” *Small*, vol. 7, no. 22, pp. 3186–3192, 2011.
- [64] J. Kang *et al.*, “High-performance graphene-based transparent flexible heaters,” *Nano Lett.*, vol. 11, no. 12, pp. 5154–5158, 2011.
- [65] B. W. An *et al.*, “Stretchable, Transparent Electrodes as Wearable Heaters Using Nanotrough Networks of Metallic Glasses with Superior Mechanical Properties and Thermal Stability,” *Nano Lett.*, vol. 16, no. 1, pp. 471–478, 2016.
- [66] S. Petsch *et al.*, “Smart artificial muscle actuators: Liquid crystal elastomers with

- integrated temperature feedback,” *Sensors Actuators, A Phys.*, vol. 231, pp. 44–51, 2015.
- [67] A. Firouzeh and J. Paik, “The Design and Modeling of a Novel Resistive Stretch Sensor with Tunable Sensitivity,” *IEEE Sens. J.*, vol. 15, no. 11, pp. 6390–6398, 2015.
- [68] N. Vachicouras, C. M. Tringides, P. B. Campiche, and S. P. Lacour, “Engineering reversible elasticity in ductile and brittle thin films supported by a plastic foil,” *Extrem. Mech. Lett.*, vol. 15, pp. 63–69, 2017.
- [69] A. Baldwin and E. Meng, “A kirigami-based Parylene C stretch sensor,” *Proc. IEEE Int. Conf. Micro Electro Mech. Syst.*, no. January, pp. 227–230, 2017.
- [70] T. C. Shyu *et al.*, “A kirigami approach to engineering elasticity in nanocomposites through patterned defects,” *Nat. Mater.*, vol. 14, no. 8, pp. 785–789, 2015.
- [71] Z. Wang, L. Zhang, S. Duan, H. Jiang, J. Shen, and C. Li, “Kirigami-patterned highly stretchable conductors from flexible carbon nanotube-embedded polymer films,” *J. Mater. Chem. C*, vol. 5, no. 34, pp. 8714–8722, 2017.
- [72] M. K. Blees *et al.*, “Graphene kirigami,” *Nature*, vol. 524, no. 7564, pp. 204–207, 2015.
- [73] J. Vanfleteren *et al.*, “Printed circuit board technology inspired stretchable circuits,” *MRS Bull.*, vol. 37, no. 3, pp. 254–260, 2012.
- [74] J. Song, H. Jiang, Y. Huang, and J. A. Rogers, “Mechanics of stretchable inorganic electronic materials,” *J. Vac. Sci. Technol. A Vacuum, Surfaces, Film.*, vol. 27, no. 5, pp. 1107–1125, 2009.
- [75] A. Firouzeh, Y. Sun, H. Lee, and J. Paik, “Sensor and actuator integrated low-profile robotic origami,” *IEEE Int. Conf. Intell. Robot. Syst.*, pp. 4937–4944, 2013.
- [76] DuPont™, “Pyr Lux FR Bond Ply ® Technical Information,” *Direct*. [Online]. Available: http://www.dupont.com/content/dam/dupont/products-and-services/electronic-and-electrical-materials/flexible-rigid-flex-circuit-materials/documents/Pyr LuxLFbondply_DataSheet.pdf.
- [77] Swiss-composite, “Glass Fiber Frame Technical Information,” 2018. [Online]. Available: <https://www.swiss-composite.ch/pdf/Produkteuebersicht.pdf>.
- [78] S. Technologies, “Shape Memory Polymer MM5520 Technical Information.” [Online]. Available: <http://www2.smp techno.com/en/smp/>.
- [79] J. J. Craig, *Introduction To Robotics - Mechanics And Control*, Third. Pearson Education International, 2005.
- [80] E. Vyhmeister, “Graphene Kirigami And Its Use In Biocompatible Strain Sensor,”

-
- Honor Thesis*, 2016.
- [81] N.-S. Jang, K.-H. Kim, S.-H. Ha, S.-H. Jung, H. M. Lee, and J.-M. Kim, “Simple Approach to High-Performance Stretchable Heaters Based on Kirigami Patterning of Conductive Paper for Wearable Thermotherapy Applications,” *ACS Appl. Mater. Interfaces*, 2017.
- [82] “Serpentine Resistance Path.” [Online]. Available: http://www.prenhall.com/howe3/microelectronics/pdf_folder/lectures/tth/lecture4.fm5.pdf. [Accessed: 09-Oct-2018].
- [83] ATP, “Integrated TaN Resistors.” [Online]. Available: <http://www.thinfilm.com/resistors.html>. [Accessed: 09-Oct-2018].
- [84] “Polyimide Full Cure.” [Online]. Available: https://cmi.epfl.ch/photo/photo_process/files/Sawatec_processPI.php. [Accessed: 17-Oct-2018].
- [85] “Photoresist Soft Bake.” [Online]. Available: https://cmi.epfl.ch/photo/photo_process/files/AZ9200_spincurve.php. [Accessed: 17-Oct-2018].
- [86] J. H. Correia and J. P. Carmo, *Introdução às Microtecnologias no Silício*. LIDEL edições técnicas, 2010.
- [87] “SPTS Machine.” [Online]. Available: http://www.spts.com/uploaded_files/shared/App_Briefs/EPD-letter.pdf. [Accessed: 04-Feb-2018].
- [88] P. Marcus, *Corrosion Mechanisms in Theory and Practice Third Edition*, 3rd Editio. CRC Press, 2011.
- [89] J. Petrovic and G. Thomas, “Reaction of Aluminum with Water to Produce Hydrogen,” 2008.
- [90] “Electrolysis of Water.” [Online]. Available: <http://www2.uni-siegen.de/~pci/versuche/english/v21-2.html>. [Accessed: 09-Oct-2018].
- [91] T. R. Kuphaldt, *Lessons in Electric Circuits - Volume I - DC*, 5th Editio. 2006.
- [92] Toshiba, “SSM3K09FU,” 2014. [Online]. Available: <https://toshiba.semicon-storage.com/info/docget.jsp?did=19599&prodName=SSM3K09FU>. [Accessed: 09-Oct-2018].
- [93] Toshiba, “MOSFET Gate Drive Circuit,” 2018. [Online]. Available: <https://toshiba.semicon-storage.com/info/docget.jsp?did=59460&prodName=TK5Q65W>. [Accessed: 09-Oct-
-

- 2018].
- [94] “MOSFET as a Switch.” [Online]. Available: https://www.electronicstutorials.ws/transistor/tran_7.html. [Accessed: 09-Oct-2018].
- [95] G. Minas, *Sebenta - Microelectrónica II.* .
- [96] T. Instruments, “OPAx22x High Precision , Low Noise Operational Amplifiers,” 2015. [Online]. Available: <http://www.ti.com/lit/ds/sbos110b/sbos110b.pdf>. [Accessed: 09-Oct-2018].
- [97] T. Instruments, “INA225,” 2014. [Online]. Available: <http://www.ti.com/lit/ds/symlink/ina225.pdf>. [Accessed: 09-Oct-2018].
- [98] Microchip, “MCP6292,” 2007. [Online]. Available: <http://ww1.microchip.com/downloads/en/DeviceDoc/21812e.pdf> . [Accessed: 09-Oct-2018].
- [99] T. Instruments, “Analysis of the Sallen-Key Architecture Application Report,” 2002.
- [100] Interlink, “FSR 400.” [Online]. Available: https://cdn2.hubspot.net/hubfs/3899023/Interlinkelectronics/November2017/Docs/Datasheet_FSR.pdf. [Accessed: 11-Oct-2018].
- [101] RightHandLabs, “TakkStrip.” [Online]. Available: <https://www.labs.righthandrobotics.com/takkstrip>. [Accessed: 11-Oct-2018].
- [102] SingleTact, “SingleTact Miniature Force Sensors.” [Online]. Available: <https://www.singletact.com/>. [Accessed: 11-Oct-2018].
- [103] Y. Tenzer, L. Jentoft, and R. Howe, “<p>Inexpensive and Easily Customized Tactile Array Sensors using MEMS Barometers Chips</p>,” *IEEE R&A Mag.*, vol. 21, no. c, p. 2013, 2012.
- [104] “NTC Thermistor by Vishay.” [Online]. Available: <https://pt.mouser.com/datasheet/2/427/ntcs0402e3t-247386.pdf>. [Accessed: 11-Oct-2018].
- [105] “NTC Thermistors.” [Online]. Available: <http://www.resistorguide.com/ntc-thermistor/>. [Accessed: 11-Oct-2018].
- [106] “Selecting a Thermistor or RTD.” [Online]. Available: <https://www.digikey.com/en/articles/techzone/2012/mar/selecting-a-thermistor-or-rtd>. [Accessed: 11-Oct-2018].
- [107] “Difference between Thermistor and RTD.” [Online]. Available: <http://www.differencebetween.net/technology/difference-between-thermistor-and-rtd/>. [Accessed: 11-Oct-2018].
-

-
- [108] J. S. Steinhart and S. R. Hart, “Calibration curves for thermistors,” *Deep. Res. Oceanogr. Abstr.*, vol. 15, no. 4, pp. 497–503, 1968.
- [109] “A Summary of Error Propagation.” [Online]. Available: http://ipl.physics.harvard.edu/wp-uploads/2013/03/PS3_Error_Propagation_sp13.pdf. [Accessed: 11-Oct-2018].
- [110] “I²C.” [Online]. Available: [https://en.wikipedia.org/wiki/I²C](https://en.wikipedia.org/wiki/I%C2%B2C). [Accessed: 11-Oct-2018].
- [111] “Basics of the I²C communication protocol.” [Online]. Available: <http://www.circuitbasics.com/basics-of-the-i2c-communication-protocol/>. [Accessed: 11-Oct-2018].
- [112] “I²C communication protocol.” [Online]. Available: <https://learn.sparkfun.com/tutorials/i2c>. [Accessed: 11-Oct-2018].
- [113] “74HC4051 Multiplexer.” [Online]. Available: <http://www.ti.com/lit/ds/symlink/cd74hct4053.pdf>. [Accessed: 11-Oct-2018].
- [114] T. Dean, *Network + Guide to Networks*, 6th Edition. 2013.
- [115] “Logic levels.” [Online]. Available: <https://learn.sparkfun.com/tutorials/logic-levels/all>. [Accessed: 11-Oct-2018].
- [116] “Linear Motor.” [Online]. Available: <https://www.actuonix.com/L16-Linear-Actuators-p/116-p.htm>. [Accessed: 11-Oct-2018].
- [117] G. A. Kragten, M. Baril, C. Gosselin, and J. L. Herder, “Stable precision grasps by underactuated grippers,” *IEEE Trans. Robot.*, vol. 27, no. 6, pp. 1056–1066, 2011.
- [118] “Second Order Filters.” [Online]. Available: <https://www.electronicstutorials.ws/filter/second-order-filters.html>. [Accessed: 19-Oct-2018].

APPENDIX I – RATE OF TENDON DISPLACEMENT

As seen in section 3.2., the tendon displacement is given by equation (41)

$$X_i = g - \sqrt{X_{i_x}^2 + X_{i_y}^2} \quad (41)$$

Differentiating the above equation in order to the joints angle, one obtains equation (42a)

$$\frac{dX_i}{d\theta_i} = -\frac{1}{2} \frac{1}{\sqrt{X_{i_x}^2 + X_{i_y}^2}} (2X_{i_x}(X_{i_x}') + 2X_{i_y}(X_{i_y}')) = -\frac{1}{\sqrt{X_{i_x}^2 + X_{i_y}^2}} (X_{i_x}(X_{i_x}') + X_{i_y}(X_{i_y}')) \quad (42a)$$

, where X_{i_x}' and X_{i_y}' are described by equation (43a) and (44a).

$$X_{i_x}(X_{i_x}') = X_{i_x} \left[-\frac{g}{2} \sin(\theta_i) - b \cos(\theta_i) \right] \quad (43a)$$

$$X_{i_y}(X_{i_y}') = X_{i_y} \left[\frac{g}{2} \cos(\theta_i) - b \sin(\theta_i) \right] \quad (44a)$$

Looking at the terms inside the brackets in (43a) and (44a) it is possible to rewrite both equations using equations (7) and (8) from section 3.2, resulting in equations (43b) and (44b).

$$X_{i_x}(X_{i_x}') = X_{i_x} \left[-\frac{g}{2} \sin(\theta_i) - b \cos(\theta_i) + b - b \right] = X_{i_x} (-X_{i_y} - b) \quad (43b)$$

$$X_{i_y}(X_{i_y}') = X_{i_y} \left[\frac{g}{2} \cos(\theta_i) - b \sin(\theta_i) + \frac{g}{2} - \frac{g}{2} \right] = X_{i_y} \left(X_{i_x} - \frac{g}{2} \right) \quad (44b)$$

Hence, equation (42a) is rewritten as shown in equation (42b).

$$\frac{dX_i}{d\theta_i} = -\frac{1}{\sqrt{X_{i_x}^2 + X_{i_y}^2}} \left[X_{i_x} (-X_{i_y} - b) + X_{i_y} \left(X_{i_x} - \frac{g}{2} \right) \right] = \frac{X_{i_x} b + X_{i_y} \frac{g}{2}}{\sqrt{X_{i_x}^2 + X_{i_y}^2}} \quad (42b)$$

, as we wish to demonstrate.

APPENDIX II – ASL ELONGATION

According to Figure 74, the elongation can be described by equation (45a).

- ① $\left(h + \frac{t_{ASL}}{2}\right)$
- ② $\left(h + \frac{t_{ASL}}{2}\right) - \left(h + \frac{t_{ASL}}{2}\right) \cos(\theta)$
- ③ $\left(h + \frac{t_{ASL}}{2}\right) \sin(\theta)$

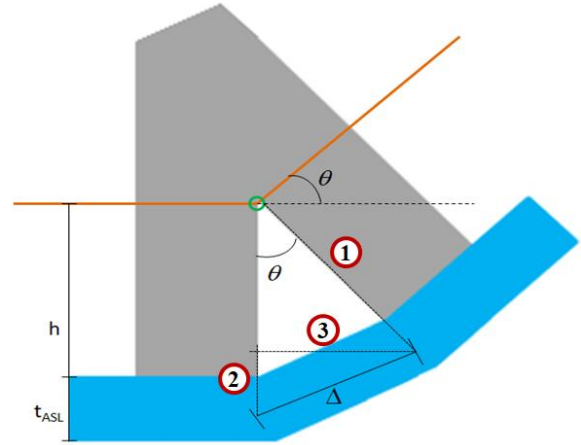


Figure 74 – Schematic of the ASL elongation with the dimensions necessary to calculate the elongation.

$$\begin{aligned}
 \Delta &= \sqrt{\left[\left(h + \frac{t_{ASL}}{2}\right) \sin(\theta)\right]^2 + \left[\left(h + \frac{t_{ASL}}{2}\right) - \left(h + \frac{t_{ASL}}{2}\right) \cos(\theta)\right]^2} = \\
 &= \sqrt{\left(h + \frac{t_{ASL}}{2}\right)^2 [\sin^2(\theta) + (1 - \cos(\theta))^2]} = \\
 &= \left(h + \frac{t_{ASL}}{2}\right) \sqrt{\sin^2(\theta) + 1 + \cos^2(\theta) - 2 \cos(\theta)}
 \end{aligned} \tag{45a}$$

Since $\sin^2(\theta) + \cos^2(\theta) = 1$, then equation (45a) can be written as equation (45b)

$$\Delta = \left(h + \frac{t_{ASL}}{2}\right) \sqrt{2 - 2 \cos(\theta)} = \left(h + \frac{t_{ASL}}{2}\right) \sqrt{2(1 - \cos(\theta))} \tag{45b}$$

Since $1 - \cos(\theta) = 2 \sin^2\left(\frac{\theta}{2}\right)$ and $\sin^2(\theta) + \cos^2(\theta) = 1$, then, one obtains equation (45c)

$$\Delta = \left(h + \frac{t_{ASL}}{2}\right) \sqrt{2 \times 2 \sin^2\left(\frac{\theta}{2}\right)} = 2 \left(h + \frac{t_{ASL}}{2}\right) \sin \frac{\theta}{2} \tag{45c}$$

, as we wish to demonstrate.

APPENDIX III – EQUILIBRIUM STATE

The equilibrium state to find a stable configuration, as seen before, is written as shown in equation (46a).

$$\mathbf{F}_t^T \dot{\mathbf{X}} = W_{\text{contact}} + W_{\text{ASL}} \quad (46a)$$

Substituting equation (4), (13) and (17), from section 3.2, in equation (46a), one obtains equation (46b)

$$\mathbf{F}_t^T \mathbf{T} \dot{\boldsymbol{\theta}} = \mathbf{f}^T \mathbf{J} \dot{\boldsymbol{\theta}} + (\mathbf{K}_{\text{ASL}} \Delta)^T \dot{\Delta} \quad (46b)$$

Using the result obtained in equation (45c) and calculating its derivative as presented in equation (47)

$$\Delta = 2 \left(h + \frac{t_{\text{ASL}}}{2} \right) \sin \left(\frac{\theta}{2} \right) \Rightarrow \dot{\Delta} = 2 \left(h + \frac{t_{\text{ASL}}}{2} \right) \frac{1}{2} \cos \left(\frac{\theta}{2} \right) \dot{\theta} \quad (47)$$

, one can substitute the above equation for the elongation derivative in equation (46b), obtaining, therefore, equation (46c).


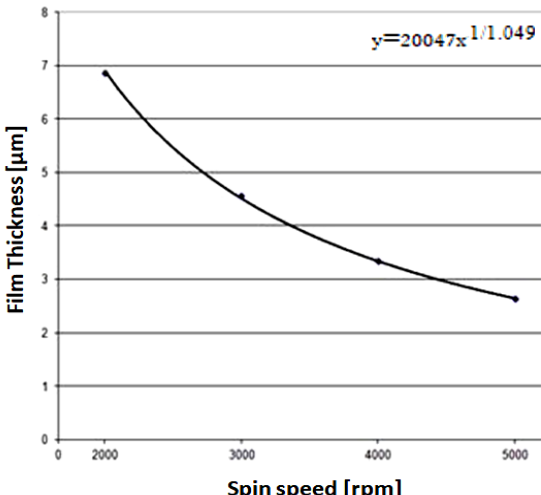

$$\begin{aligned} \mathbf{F}_t^T \mathbf{T} \dot{\boldsymbol{\theta}} &= \mathbf{f}^T \mathbf{J} \dot{\boldsymbol{\theta}} + \left(\mathbf{K}_{\text{ASL}} 2 \left(h + \frac{t_{\text{ASL}}}{2} \right) \sin \left(\frac{\theta}{2} \right) \right)^T \left(h + \frac{t_{\text{ASL}}}{2} \right) \cos \left(\frac{\theta}{2} \right) \dot{\theta} = \\ &= \mathbf{f}^T \mathbf{J} \dot{\boldsymbol{\theta}} + 2 \left(h + \frac{t_{\text{ASL}}}{2} \right)^2 \left(\mathbf{K}_{\text{ASL}} \sin \left(\frac{\theta}{2} \right) \right)^T \cos \left(\frac{\theta}{2} \right) \dot{\theta} \end{aligned} \quad (46c)$$

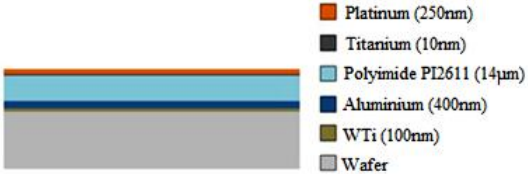


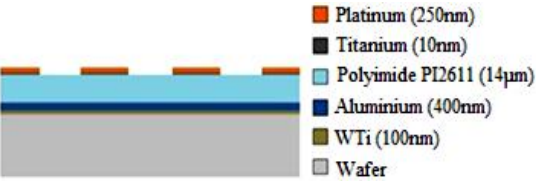
Since $\left(\sin \left(\frac{\theta}{2} \right) \right)^T \cos \left(\frac{\theta}{2} \right) = \left(\frac{\sin(\theta)}{2} \right)^T$, then one, finally obtains equation (46d).

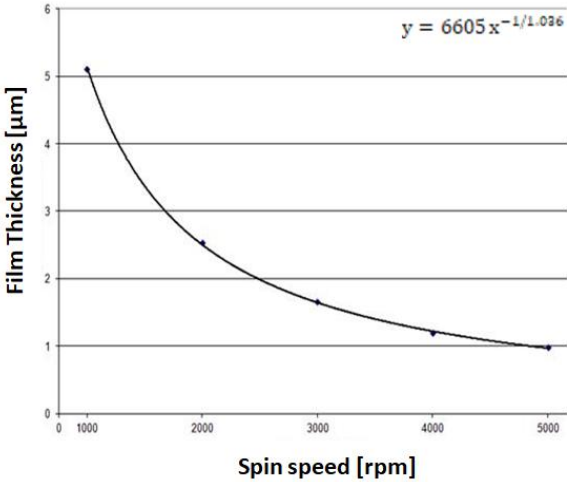
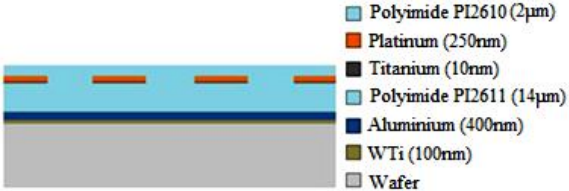
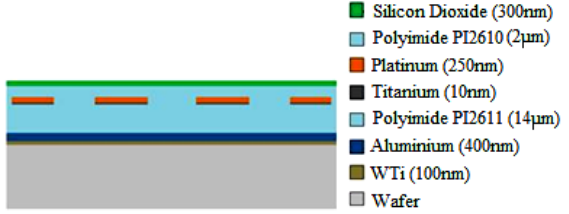
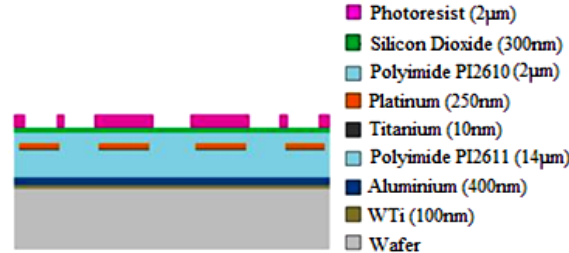
$$\begin{aligned} \mathbf{F}_t^T \mathbf{T} \dot{\boldsymbol{\theta}} &= \mathbf{f}^T \mathbf{J} \dot{\boldsymbol{\theta}} + 2 \left(h + \frac{t_{\text{ASL}}}{2} \right)^2 \left(\mathbf{K}_{\text{ASL}} \frac{\sin(\theta)}{2} \right)^T \dot{\boldsymbol{\theta}} \Leftrightarrow \\ &\Leftrightarrow \mathbf{F}_t^T \mathbf{T} = \mathbf{f}^T \mathbf{J} + \left(h + \frac{t_{\text{ASL}}}{2} \right)^2 \left(\mathbf{K}_{\text{ASL}} \sin(\theta) \right)^T \end{aligned} \quad (46d)$$

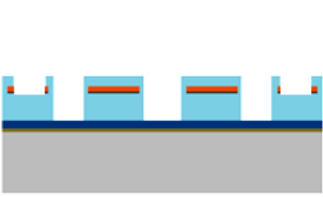



, as we wish to demonstrate.

APPENDIX IV – STRETCHABLE HEATERS MANUFACTURING PROCESS OUTLINE

Step	Process description	Observations
01	<p>Metal Deposition</p> <p>Metal : WTi/Al</p> <p>Thickness: 100nm/400nm</p> <p>Deposition Rate: WTi: 0.36nm/s Al: 0.58nm/s</p> <p>Deposition Time: WTi: 4min 38s Al: 11min 30s</p>	 <ul style="list-style-type: none"> ■ Aluminium (400nm) ■ WTi (100nm) ■ Wafer
02	<p>Polyimide Deposition</p> <p>Material: Pi2611</p> <p><u>Dehydration:</u></p> <p>Hot plate: 120°C during 10min</p> <p>Adhesion promoter (VM651): 500rpm during 10s 3000rpm during 30s (with Nitrogen)</p> <p><u>First Coating:</u></p> <p>Thickness: 7 μm</p> <p>Speed Rotation: $x = \left(\frac{20047}{7}\right)^{1/1.049} \approx 1974 \text{rpm}$</p> <p><u>Soft cure:</u></p> <p>Hot plate: 65°C during 3min 105°C during 3min</p> <p><u>Second Coating:</u></p> <p>Thickness: 7 μm</p> <p>Speed Rotation: $x = \left(\frac{20047}{6.72}\right)^{1/1.049} \approx 2053 \text{rpm}$</p>	 <p>Polyimide PI2611 coating trend line that relates the spin coating speed to achieve the desired thickness. In the right upper corner is possible to observe its function.</p>  <ul style="list-style-type: none"> ■ Polyimide PI2611 (14μm) ■ Aluminium (400nm) ■ WTi (100nm) ■ Wafer

	<p><u>Soft cure:</u> Hot plate: 65°C during 3min 105°C during 3min</p> <p><u>Full cure:</u> 300°C during 5h (ramp temperature)</p>	
<p>03</p>	<p>Metal Deposition</p> <p>Metal : Ti_r/Pt</p> <p>Thickness: 10nm/250nm</p> <p>Deposition Rate: Ti: 90nm/min Pt: 270nm/min</p> <p>Deposition Time: Ti: 6.66s Pt: 55.5s</p>	 <ul style="list-style-type: none"> Platinum (250nm) Titanium (10nm) Polyimide PI2611 (14µm) Aluminium (400nm) WTi (100nm) Wafer
<p>04</p>	<p>Photolithography</p> <p>Photoresist: AZ9221</p> <p>Thickness: 2µm</p> <p><u>Soft bake:</u> 2min</p> <p><u>Exposure:</u> Dose=130mJ/cm²</p> <p><u>Development:</u> Time: 81s</p> <p><u>Full cure:</u> Oven:105°C during 130s cure time = 90s + $\frac{20s}{1\mu m} \times 2\mu m = 130s$</p> <p><u>Reflow:</u> Hotplate: 115°C during 3min</p>	<p>Photoresist Coating :</p>  <p>Reflow:</p>  <ul style="list-style-type: none"> Photoresist (2µm) Platinum (250nm) Titanium (10nm) Polyimide PI2611 (14µm) Aluminium (400nm) WTi (100nm) Wafer
<p>05</p>	<p>Ion Beam Etching + Photoresist Strip</p> <p>Metal : Ti_r/Pt</p> <p>Thickness: 10nm/250nm</p> <p>Etch Rate: Pt: 131nm/min Ti: 40nm/min</p> <p>Deposition Time: Pt: 1min 55s Ti: 15s</p>	 <ul style="list-style-type: none"> Platinum (250nm) Titanium (10nm) Polyimide PI2611 (14µm) Aluminium (400nm) WTi (100nm) Wafer

<p>06</p>	<p>Polyimide Deposition Material: Pi2610 <u>Dehydration:</u> Hot plate: 120°C during 10min Adhesion promoter (VM651): 500rpm during 10s 3000rpm during 30s (with Nitrogen) <u>First Coating:</u> Thickness: 2 μm Speed Rotation: $x = \left(\frac{6605}{2}\right)^{1/1.036} \approx 2492 \text{rpm}$ <u>Soft cure:</u> Hot plate: 65°C during 3min 105°C during 3min <u>Full cure:</u> 300°C during 5h (ramp temperature)</p>	 <p>Polyimide PI2610 coating trend line that relates the spin coating speed to achieve the desired thickness. In the right upper corner is possible to observe its function.</p> 
<p>07</p>	<p>SiO₂ Deposition Metal: SiO₂ Thickness: 300nm Deposition Rate: 58nm/min Deposition Time: 5min 10s</p>	
<p>08</p>	<p>Photolithography Thickness: 2μm <u>Soft bake:</u> 2min <u>Exposure:</u> Dose=130mJ/cm² <u>Development:</u> Time: 81s</p>	

<p>09</p>	<p>Layer Etch + Photoresist Strip Material: SiO₂+Polyimide+ SiO₂ Thickness: 300nm/16µm/300nm Etch Rate: SiO₂: 345nm/min Polyimide: 2300nm/min Deposition Time: SiO₂: 52s Polyimide: 6min 58s</p>	 <ul style="list-style-type: none"> ■ Polyimide PI2610 (2µm) ■ Platinum (250nm) ■ Titanium (10nm) ■ Polyimide PI2611 (14µm) ■ Aluminium (400nm) ■ WTi (100nm) ■ Wafer
<p>10</p>	<p>Photolithography Thickness: 14µm Soft bake: 7min Exposure: Dose=490mJ/cm² Development: Time: 400s</p>	 <ul style="list-style-type: none"> ■ Photoresist (14µm) ■ Polyimide PI2610 (2µm) ■ Platinum (250nm) ■ Titanium (10nm) ■ Polyimide PI2611 (14µm) ■ Aluminium (400nm) ■ WTi (100nm) ■ Wafer
<p>11</p>	<p>Final Etch + Photoresist Strip Material: Polyimide+Photoresist Thickness: 2µm/14µm</p>	 <ul style="list-style-type: none"> ■ Platinum (250nm) ■ Titanium (10nm) ■ Polyimide PI2611 (14µm) ■ Aluminium (400nm) ■ WTi (100nm) ■ Wafer
<p>12</p>	<p>Device Release Anodic dissolution NaCl aqueous solution</p>	 <ul style="list-style-type: none"> ■ Platinum (250nm) ■ Titanium (10nm) ■ Polyimide PI2611 (14µm) ■ Aluminium (400nm) ■ WTi (100nm) ■ Wafer

Surface material (larger area)	Vapor HMDS	Plasma O ₂	Thermal dehydration
Si	√√	√	√
SiO ₂ , fused silica, SiN, Si ₃ N ₄	√√	√	√
Float glass, pyrex	√	√√	√
Metal Al	...	√	√√
Metals Ti, Cr, Ia	...	X	√√
III/V semiconductors (GaN, GaAs)	...	X	√√

Note: Cleanroom relative humidity control is critical for resist adhesion.

Legend:

- √√ Strongly recommended
- √ Alternative process
- ... Not effective
- X May affect or destroy underlying material

Figure 75 – Methods to improve the adhesion to the previous layers fabricated. In this case, since the new coating will be performed on top of aluminium, the best option is to perform a thermal dehydration on the wafer’s surface.

Surface material (larger area)	Vapor HMDS	Plasma O ₂	Thermal dehydration
Si	√√	√	√
SiO ₂ , fused silica, SiN, Si ₃ N ₄	√√	√	√
Float glass, pyrex	√	√√	√
Metal Al	...	√	√√
Metals Ti, Cr, Ta	...	X	√√
III/V semiconductors (GaN, GaAs)	...	X	√√

Note: Cleanroom relative humidity control is critical for resist adhesion.

Legend:

- √√ Strongly recommended
- √ Alternative process
- ... Not effective
- X May affect or destroy underlying material

Figure 76 – Methods presented to improve the adhesion to the previous layers fabricated. In this case, since the new coating will be performed on top of metallic layer, the best option is to perform a thermal dehydration on the wafer’s surface.

First digits	Coating option	→	Last digits	Spin speed [rpm]	Softbake time [mm:ss]	PR thickness [µm]
01XX	HMDS / NoEBR (topEC)		XX41	6000 (AZ9207)	01:30	0.65
02XX	Dehydrate / NoEBR (topEC)		XX42	1200 (AZ9207)	01:30	0.85
03XX	HMDS / EBR		XX45	4200 (AZ9221)	02:00	2
04XX	Dehydrate / EBR		XX46	1900 (AZ9221)	03:00	3
			XX47	1100 (AZ9221)	04:00	4
			XX49	6000 (AZ9260)	05:00	5.5
			XX50	2800 (AZ9260)	05:00	8
			XX51	1800 (AZ9260)	06:00	10
			XX52	920 (AZ9260)	07:00	15
			XX53	720 (AZ9260)	08:00	20

Figure 77 – Process to choose the appropriate recipe for coating the photoresist. The coating option allows to thermally dehydrate the wafer’s surface to improve the adhesion. The recipe is also chosen having into account the desired photoresist thickness.

Even though the process of directly writing with the laser is automatic, the energy and power for the laser to write as to be settled according to the photoresist thickness so that the pattern is transferred properly without either damaging the layers underneath nor passing the laser beam through all the photoresist layer. Figure 78 allows determining the dose to be set according with the photoresist thickness.

Illumination:	Broadband*	i-line (355-365 nm)	h-line (405 nm)
Equipment:	MABA6, MA6 Gen3 (no filter)	VPG 200, MA6 Gen3 (filter), MJB4	MLA 150
PR thickness [µm]	Dose [mJ/cm ²]*	Dose [mJ/cm ²]**	Dose [mJ/cm ²]**
2	190	175	130
3	240	220	165
4	300	270	200
5	360	330	240
8	460	420	340
10	555	470	390
14	660	580	490

Figure 78 – For the laser machine, the dose used by the laser to correctly transfer the pattern has to be set according to the photoresist thickness.

Sequence Number	Recipe name	PR thickness [µm]	Total contact time [s]
0941	CMiDev.AZ9207 0um65 puddle	0.65 0.85	58
0945	CMiDev.AZ9221 2um0 puddle	2	81
0946	CMiDev.AZ9221 3um0 puddle	3	102
0947	CMiDev.AZ9221 4um0 puddle	4	111
0949	CMiDev.AZ9260 6um0 puddle	6	148
0950	CMiDev.AZ9260 8um0 puddle	8	230
0951	CMiDev.AZ9260 10um0 puddle	10	300
0952	CMiDev.AZ9260 15um0 puddle	15	400
0953	CMiDev.AZ9260 20um0 puddle	20	561

Figure 79 – The recipe for developing the exposure photoresist is set according to the photoresist thickness. As can be seen, for 2µm of photoresist, the total contact time of the photoresist in the wafer with the developer solution is 81s.

RESIST STRIP
Positive resists etch rate = 350 nm/min depending on the number of wafers to be processed in the batch.

Program	Gas 1 (O2, ml/min)	Gas 2 (CF4, ml/min)	Power (W)	Time (min:sec)	EPD (0, 1, 2)
01	400	0	500	01.00	1
02				00.30	0
03				01.00	
04				04.00	
05				07.00	
06				10.00	
08				20.00	
07	500		1000	30.00	

Figure 80 – Recipe’s available for the physical resist strip. In this case, to ensure that the crust of the photoresist is properly etched 1min exposure to the oxygen plasma is performed.

The chemical strip for the photoresist consists on several baths using a special remover (Shipley Remover 1165) and deionised water. The process is illustrated below:

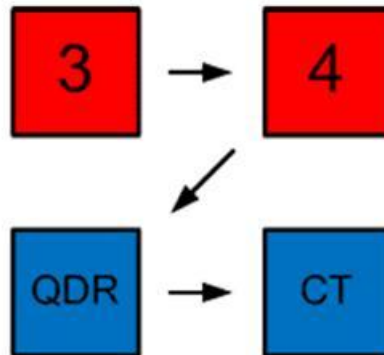


Figure 81 – Schematic description of the process performed to chemically strip the remaining photoresist.

As can be seen from the schematic above, the process consists on 4 different baths. Firstly, a remover bath occurs during 5min at 70°C at chamber 3, shown in Figure 81. The temperature and time of this recipe are standard for the resist strip. Secondly, the wafer is moved to a second remover bath, chamber 4 on Figure 81. The difference between this two baths is that the second one is performed using a cleaner remover. Therefore, the first bath allows stripping most of the photoresist while a stronger remover is used on a second bath to ensure that the remaining photoresist is properly stripped. Thirdly, the wafer is rinsed in deionised water on the QDR chamber (Quick Dump Rinsing) and finally a cascade bath, also

in deionised water is performed on the CT (Cascade) chamber. The difference between the QDR and CT bath is that the first one is performed with a greater flow of water inside the chamber whereas the second is softer. Thus, some precaution needs to be considered on the QDR bath, since the water flow can damage the devices on the wafer. Although, since the dimensions of the devices are big compared to the dimensions of the devices manufactured in the clean room, the risk of damaging the devices is low allowing performing the QDR bath and finalizing the chemical resist strip process.

APPENDIX V – SALLEN-KEY 2ND ORDER FILTER

The Sallen-Key filter topology is represented in the Figure below.

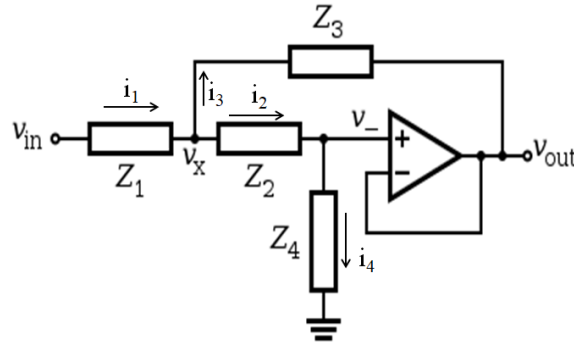


Figure 82 – 2nd Order Butterworth active filter with Sallen-Key topology.

As can be seen the filter has a unitary gain. Assuming that the operational amplifier is ideal and since we have a negative-feedback configuration, its v_+ and v_- inputs must match. In addition, since the inverting input v_- is directly connected to the output v_{out} , one has that

$$v_+ = v_- = v_{out} \quad (48)$$

Applying the Kirchoff's current law at the v_x node, one obtains equation (49).

$$i_1 = i_2 + i_3 \Leftrightarrow \frac{v_{in} - v_x}{Z_1} = \frac{v_x - v_{out}}{Z_3} + \frac{v_x - v_-}{Z_2} \quad (49)$$

Combining equations (48) and (49), one obtains

$$\frac{v_{in} - v_x}{Z_1} = \frac{v_x - v_{out}}{Z_3} + \frac{v_x - v_{out}}{Z_2} \quad (50)$$

Applying equation (48) and the Kirchoff's current law to the non-inverting input v_+ , and not forgetting that ideally, $i_+ \approx 0$ and $i_- \approx 0$, then the voltage at the v_x node can be written as shown in equation (51).

$$i_2 = i_4 \Leftrightarrow \frac{v_x - v_+}{Z_2} = \frac{v_{out}}{Z_4} \Leftrightarrow \frac{v_x - v_{out}}{Z_2} = \frac{v_{out}}{Z_4} \Leftrightarrow v_x = v_{out} \left(\frac{Z_2}{Z_4} + 1 \right) \quad (51)$$

Combining the equations (50) and (51), one obtains the gain of the system, presented in equation (52).

$$\frac{v_{out}}{v_{in}} = \frac{Z_3 Z_4}{Z_1 Z_2 + Z_3 (Z_1 + Z_2 + Z_4)} \quad (52)$$

, which typically describes a second-order linear time-invariant (LTI) system.

In the above equation, for the designed low-pass filter, the impedances are described as

$$Z_1 = R_1 = 62\text{k}\Omega, \quad Z_2 = R_2 = 36\text{k}\Omega, \quad Z_3 = \frac{1}{sC_1} = \frac{1}{s100\text{nF}}, \quad Z_4 = \frac{1}{sC_2} = \frac{1}{s47\text{nF}} \quad (53)$$

The transfer function for a second-order unity-gain low-pass filter is given by equation (54), where the undamped natural frequency f_0 , attenuation α and quality factor, Q , are given by the set of equations (55) to (57).

$$H(s) = \frac{\omega_0^2}{s^2 + 2\alpha s + \omega_0^2} \quad (54)$$

$$\omega_0 = 2\pi f_0 = \frac{1}{\sqrt{R_1 R_2 C_1 C_2}} \Leftrightarrow f_0 = 49.14\text{Hz} \quad (55)$$

$$2\alpha = 2\zeta\omega_0 = \frac{\omega_0}{Q} = \frac{1}{C_1} \left(\frac{1}{R_1} + \frac{1}{R_2} \right) \quad (56)$$

$$Q = \frac{\omega_0}{2\alpha} = \frac{1}{C_1} \left(\frac{1}{R_1} + \frac{1}{R_2} \right) = 0.703 \quad (57)$$

$$\zeta = \frac{1}{2Q} = 0.7112 \quad (58)$$

Despite Butterworth filters roll-off more slowly around the cutoff frequency f_0 than the Chebyshev filter or the Elliptic filter, they do not present ripple effects, as shown in Figure 83.

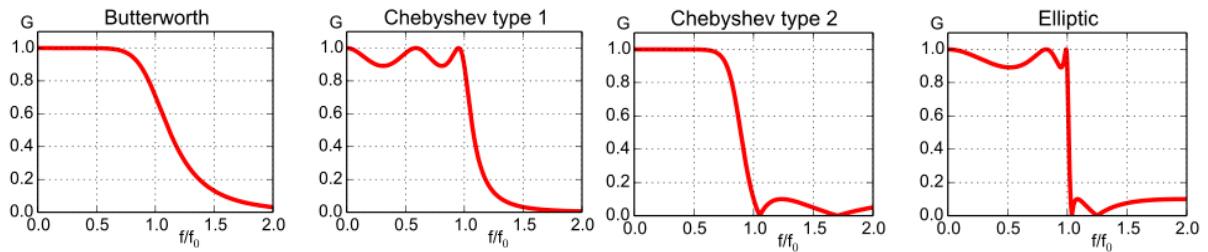


Figure 83 – Gain and frequency response of Butterworth, Chebyshev and Elliptic filters.

Furthermore, the value of the damping factor, ζ , is very near the desired value for a maximum flat gain characteristic of these filters, as depicted on Figure 84 [118].

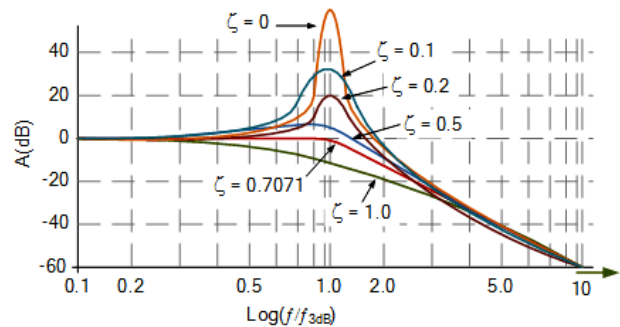


Figure 84 – Second order low pass-filter amplitude response.

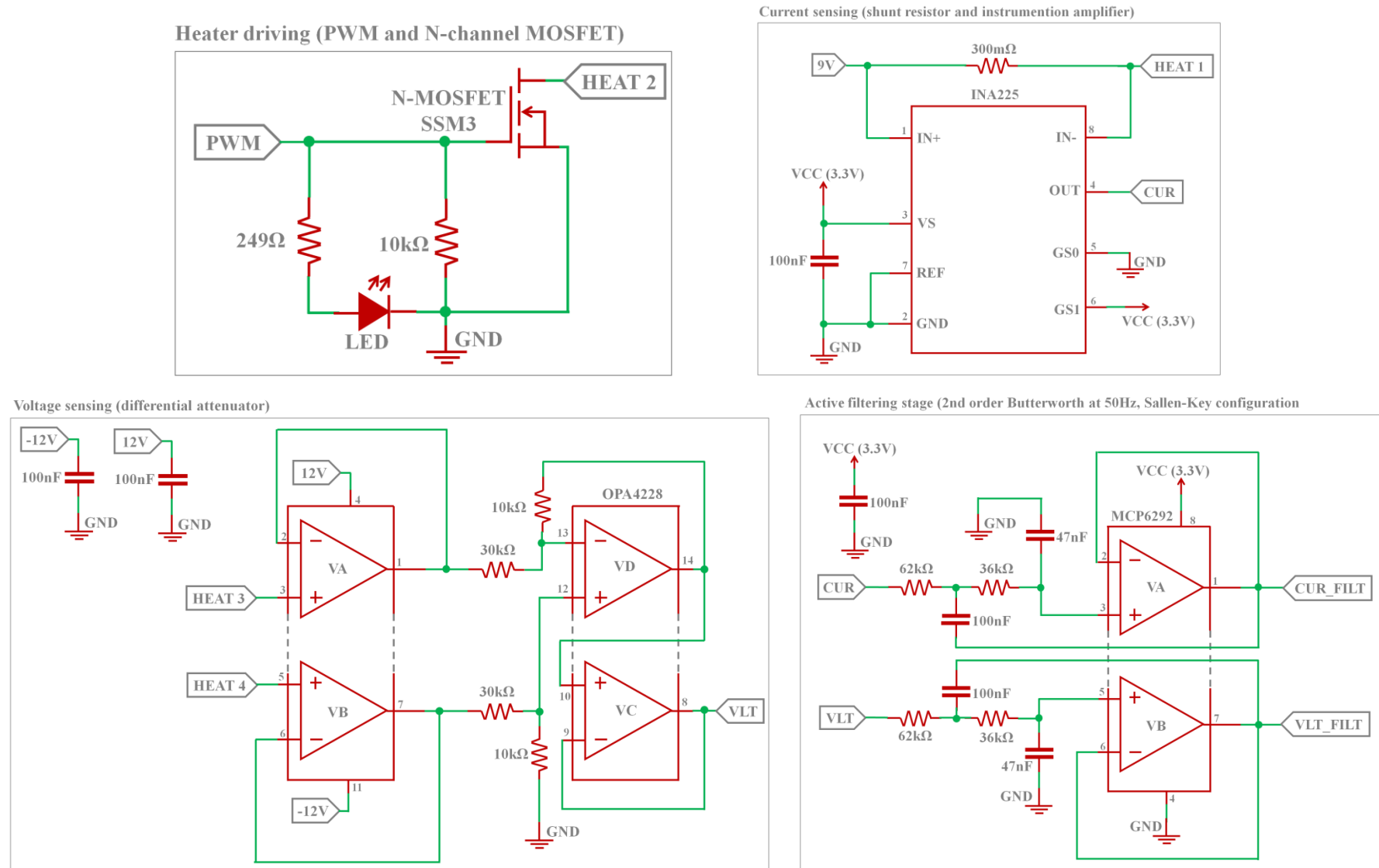


Figure 85 – Schematic of the electronic circuit that activates and measure the resistance of the heater.